# CHALMERS

## Actinide oxides co-precipitation and reduction of Ca-uranyl-carbonato complexes by iron

**Mustapha Gida Saleh**

**Licentiate seminar will be held in 10 an, Kemigården 4**

**2nd October 2024**

**Discussion leader:**
**Prof. Kristina Kvashnina.**

**The thesis is available at:**
**Department of Chemistry and Chemical Engineering**
**Chalmers University of Technology**
**412 96 Gothenburg, Sweden**
**Phone: +46 (0) 31-772 1000**


CHALMERS
UNIVERSITY OF TECHNOLOGY

**THESIS FOR THE DEGREE OF LICENTIATE OF ENGINEERING**

# Actinide oxides co-precipitation and reduction of Ca-uranyl-carbonato complexes by iron

**Mustapha Gida Saleh**

**Nuclear Chemistry**
**Department of Chemistry and Chemical Engineering**

**CHALMERS UNIVERSITY OF TECHNOLOGY**

**Gothenburg, Sweden 2024**

Actinide oxides co-precipitation and reduction of Ca-uranyl-carbonato complexes by iron.



Technical report no 2024: 18

Department of Chemistry and Chemical Engineering
Chalmers University of Technology
SE- 412 96 Gothenburg,
Sweden
Telephone: +46 (0) 31-772 1000

Cover: Mechanism of spent nuclear fuel dissolution under disposal condition.

Printed by Chalmers digitalryck
Gothenburg, Sweden 2024

# Actinide oxides co-precipitation and reduction of Ca-uranyl-carbonato complexes by iron

**Mustapha Gida Saleh**

**Nuclear Chemistry**
**Department of Chemistry and Chemical Engineering**
**Chalmers University of Technology**

## Abstract

Given the escalating global energy demands and consumption trends, nuclear energy has witnessed a resurgence worldwide. Several nations are reaffirming their commitment to expanding nuclear power generation to achieve energy security, fulfill climate goals, and foster sustainable development. However, the safe disposal of high-level radioactive waste, particularly spent nuclear fuel, remains a significant challenge on a global scale. Proposed solutions include deep geological repositories situated approximately 500-1000 meters underground, intended for the management of this hazardous waste. While these repositories are designed to transition rapidly to anoxic, reducing conditions after closure, the potential breach of safety barriers, such as containment canisters, could lead to localized oxidizing conditions. This scenario arises from the ionizing radiation present in spent fuel, which generates radiolytic oxidants, thereby causing the oxidative dissolution of the fuel. Nevertheless, the presence of dissolved Fe(II) and molecular hydrogen, acting as repository reductants, can significantly suppress the oxidative dissolution of the fuel by consuming the radiolytic oxidants. This study delves into the interaction between corroded metallic iron (canister material) and dissolved U(VI) in simulated groundwater compositions under anoxic conditions, with an investigation on whether the formation of Ca-uranyl-carbonato complexes hinders the reduction of U(VI) by metallic iron. Concurrently, the leaching of used nuclear fuel remains a pivotal aspect of safety analysis for underground repositories. Co-precipitation, initially proposed as a radionuclide retention mechanism, offers promise for lowering the solubility of minor components in nuclear waste disposal scenarios. To explore this phenomenon further, a co-precipitation experiment involving Ce(III) oxide with $UO_2$, a major component of spent fuel, was conducted, to investigate the potential possibility for actinides ions to co-precipitate with each other under disposal conditions, with Ce serving as a surrogate for Pu. Understanding these interactions would provide insights into the release mechanisms of radionuclides into the environment.

A multidisciplinary approach integrating chemical analysis, spectroscopy technique (ICP-MS, XAS),surface analysis (XPS),crystallography (XRD) and micro structural analysis (SEM-EDX) was employed in these studies for both liquid and solid characterizations. The findings suggest that the concentrations of Ce, other lanthanides or actinides and fission products released by the fuel matrix during oxidative dissolution will be orders of magnitude lower than their individual solubilities when they co-precipitate with $UO_2$(s) at the iron surface of the canister material. In the Ca-uranyl carbonato complexes studies in the presence of iron ,metallic iron foils efficiently reduced U(VI) to U(IV), leading to its significant sorption and precipitation on the iron foil surfaces as U(IV).

**Keywords: Ce(III), $UO_2$, Solubility, Co-precipitation, Groundwater, Fe(II), U(VI)**

## List of Publications

This thesis is based on the following publications.

### Paper 1

N.L.Hansson., M. Saleh., P. L. Tam., S. Holgersson., K. Spahiu., C. Ekberg (2023). Influence of groundwater composition on the reductive precipitation of U (VI) on corroding iron foil surfaces. Journal of Nuclear Materials 577,154324

Contribution: Investigation, Formal analysis, Writing-review and editing.

### Paper 2

M. Saleh., M. Hedberg., P. L. Tam., K. Spahiu., I. Persson., C. Ekberg (2024). Coprecipitation of Ce(III) oxide with $UO_2$.

Manuscript accepted for publication in Journal of Synchrotron Radiation

Contribution: Conceptualization, Formal analysis, Investigation, Methodology, Writing - original draft, review and editing.

## Abbreviations and definitions

The following abbreviations, acronyms and definitions were used during this thesis:

| | |
|---|---|
| ACS | American Chemical Society |
| am | Amorphous |
| Ce | Cerium |
| EDX | Energy Dispersive X-ray |
| EXAFS | Extended X- ray Absorption Fine Structure |
| GW | Giga Watt |
| ICP-MS | Inductively Coupled Plasma Mass Spectroscopy |
| IEA | International Energy Agency |
| LWR | Light Water Reactors |
| mM | Milli molar |
| MeV | Mega electron volt |
| MOX | Mixed Oxide fuel |
| MQ | Milli-Q (for high purity water) |
| MWe | Mega Watt electric |
| HLW | High -Level Waste |
| ppb | Part per billion |
| ppm | Part per million |
| Pu | Plutonium |
| PWR | Pressurized water reactors |
| P-XRD | Powder X-ray Diffraction |
| SEM | Scanning Electron Microscopy |
| SKB | Swedish Nuclear Fuel and Waste Management. Company |
| SNF | Spent Nuclear Fuel |
| U | Uranium |
| $UO_2$ | Uranium dioxide |
| UV-vis | Ultraviolet Visible Spectroscopy |
| XAS | X-ray Absorption Spectroscopy |
| XANES | X-ray Absorption Near Edge structure |
| XPS | X-ray Photoelectron Spectroscopy |

## Table of Contents

# 1.0. Introduction

In recent years, nuclear power has experienced a resurgence globally as countries seek to address climate change and enhance energy security [1]. The integration and expansion of nuclear energy have become pivotal in achieving sustainable development goals, with significant growth anticipated particularly in Asia, Europe, and the Americas [2]. While countries like Germany have opted to phase out nuclear energy, others are expanding their capacities, illustrating diverse national approaches amidst evolving energy policies [1].
By 2026, the global nuclear capacity is expected to grow substantially, with approximately 29 gigawatts (GW) of new capacity to become operational worldwide, led notably by China and India [1, 2]. This growth underscores a broader international commitment, reaffirmed at events such as the 2024 first nuclear energy summit held in Brussels, to harness nuclear power for sustainable development, to achieve energy security and climate mitigation [3].

Despite its promise, nuclear power faces persistent challenges, notably construction risk in financing nuclear projects and public acceptance issues [1,4].Concerns over safety, exacerbated by past nuclear accidents, and the management of radioactive waste remain critical [5]. Efforts to secure viable long-term storage solutions for spent nuclear fuel (SNF), which constitutes over 95% of radioactive waste generated, highlight the complexity and urgency of these challenges [6].

One proposed solution for SNF management and disposal is deep geological repositories, currently under development in several countries including Sweden and Finland [7,8]. Sweden's KBS-3 repository concept, designed by the Swedish Nuclear Fuel and Waste Management Company (SKB), involves encapsulating SNF in copper canisters surrounded by bentonite clay and buried 500 meters deep in granitic bedrock [9]. This method aims to isolate SNF from the biosphere for hundreds of thousands of years, relying on both natural and engineered barriers such as the bedrock formations, copper canisters and bentonite clay to ensure containment and safety [10].

This thesis work focuses on understanding some key processes influencing the long-term safety of SNF disposal within the KBS-3 repository concept. More specifically, it investigates the interaction between U(VI) and corroded metallic iron, a critical component of the canister material. The study aims to evaluate if calcium-uranyl-carbonato complexes hinder the reductive precipitation of U(VI) by metallic iron under repository-relevant conditions. Additionally, the study of the co-precipitation of Ce(III) oxide with $UO_2$ was carried out to understand some phenomena observed during SNF leaching and to also elucidate potential mechanisms influencing the solubility and mobility of actinides in repository environments.

The study investigates if the co-precipitation of actinides oxides or the formation of solid solutions can occur during spent fuel leaching under disposal conditions, as well as the nature of the solid solutions formed. To explore the underlying principles and refine the methodology, the co-precipitation of U(IV) and Ce(III) was studied, where Ce(III) was used as a surrogate for Pu(III). The ionic radius of Ce(III) (1.03 Å  in six-fold coordination) is quite similar to that of Pu(III) (1.00 Å Pu(III) in six-fold coordination). While both Pu(III) and Pu(IV) are expected to coexist in solution under repository conditions (Neck et al.,2007) ,Ce(III) was selected due to the need to maintain U(IV) in its reduced state and to prevent its oxidation.

The goal of this study is to enhance the understanding of actinide solubilities in repository conditions, contributing to the safety assessment of SNF. This thesis aims to fill the remaining knowledge gaps in these areas, thereby advancing the understanding of SNF behavior under disposal conditions and contributing to improved safety protocols.

# 2.0. Background

This chapter presents the background to the research project work with an overview of spent nuclear fuel under disposal condition, the process leading to its oxidative dissolution or corrosion and the effect of potential repository reductants on its dissolution.

## 2.1. Chemistry of uranium

Uranium (U), a heavy and naturally abundant radioactive element from the actinide series, was discovered in 1789 by Martin Heinrich Klaproth in pitchblende. Initially used as a colorant for ceramics and glasses, its radioactive properties were discovered by Henri Becquerel in 1896. Marie Curie developed techniques to measure its radioactivity, and the U-235 isotope was identified in 1935. The crucial significance of uranium was fully realized with the discovery of nuclear fission by Hahn and Strassman in 1938, positioning uranium at the core of nuclear energy and electricity generation in nuclear power plants [11].

Nuclear energy involves the use of naturally occurring fissile isotopes like U-235 and fertile U-238 in a nuclear reactor to generate power. This highlights the profound scientific and technical significance of uranium's chemistry and technology [11]. U is also of important interest for the long-term safety assessment of nuclear waste under deep geological repositories. It is relatively abundant in the earth´s crust with a concentration of 2-3 part per million (ppm) which is more abundant than silver, mercury, antimony, and cadmium. Uranium occurs in diverse minerals like pitchblende, uraninite, carnotite, and autunite, exhibiting a wide range of structural and chemical variability. This variation arises from the various chemical environments in which uranium minerals originate [12,13]. It can form a variety of compounds through chemical interactions with inorganic species and organic ligands [11,14].

The natural occurrence of uranium consists of a mixture of the three isotopes U-238 ($t_{1/2} = 4.47. 10^9$ y), U-235 ($t_{1/2} = 7.04. 10^8$ y), U-234 ($t_{1/2} = 2.46. 10^5$ y) all of which are alpha emitters, with respective natural abundances of 99.275 atomic %, 0.72 atomic %, and 0.005 atomic %. The atomic weight of natural uranium is approximately 238.0289 [15].

In aqueous solutions, uranium can exist in various oxidation states, primarily U(IV), U(V), and U(VI). Among these, the hexavalent state, U(VI), typically the uranyl ion ($UO_2^{2+}$) is the most stable particularly in the presence of carbonate ions and in oxygen-rich environments and predominant under the Earth's surface conditions [16]. The other oxidation states, U(IV) and U(V), are less stable. U(IV) tends to precipitate out as uranium dioxide ($UO_2$) under reducing conditions, while U(V) relatively rare often disproportionate into U(IV) and U(VI) [11,16]. In the absence of oxidizing agents such as oxygen, U(IV) remain stable in aqueous solution, but in the presence of oxygen, it can undergo oxidation to form the more soluble U(V) and U(VI) states [11].

The relative stability of these oxidation states is significantly influenced by the pH of the solution and the presence of complex ligands. Compounds containing tetravalent uranium are insoluble under mildly acidic to alkaline conditions, whereas hexavalent compounds are highly soluble and mobile. In solution, U(VI) forms soluble complexes with carbonate, oxalate, and hydroxides, contributing to its high solubility [11]. It is also highly susceptible to adsorption

by organic matter or by precipitation with various anions, such as hydroxide, silicate, and phosphate [11]. Uranium occurs in sea water at a concentration of 3 part per billion (ppb) [11]

## 2.2. Nuclear fuel and nuclear reactors

Nuclear fuel is a material used in nuclear reactors to sustain a nuclear chain reaction. The most common type of nuclear fuel is uranium, specifically in the form of uranium dioxide ($UO_2$). $UO_2$ is highly suitable as a nuclear fuel due to its high melting point, stability under irradiation, and it does not undergo phase transformations at elevated temperature [17]. Following uranium mining, milling and purification from its ore, the uranium oxide obtained cannot be directly utilized as fuel for a nuclear reactor, necessitating additional processing (enrichment) [18,19]. The fabrication of nuclear fuel involves converting enriched uranium hexafluoride ($UF_6$) gas into uranium dioxide powder, pressing the powder into cylindrical ceramic pellets, and then sintering these pellets at high temperatures under reducing conditions to achieve a high density close to 95% of theoretical density ($10.96 g/cm^3$) for freshly produced $UO_2$ pellets [11,20]. These pellets are then stacked in metal cladding tubes made of zircaloy, forming fuel rods. These rods are assembled into fuel bundles, ready to be loaded into a nuclear reactor [20].

The nuclear reactor is used to initiate and control a sustained nuclear chain reaction. Reactors are the core components of a nuclear power plant and are responsible for converting nuclear energy into thermal energy, which is then used to generate electricity. There are several types of nuclear reactors, but the most common type used for power generation is the light water reactors (LWR), which are of two main principal designs, boiling water reactors (BWR) and pressurized water reactors (PWR). These reactors generate heat through the process of nuclear fission.

The operation of nuclear reactors is based on the principle of nuclear fission, in which a thermal neutron splits a heavy nucleus such as U-235 into two smaller nuclei (fission fragments) releasing a few neutrons and a significant amount of energy. The newly released neutrons induce fission in other U-235 nuclei, while the energy released from fission is primarily in the form of kinetic energy of the fission products, which is converted into thermal energy. The thermal energy is absorbed by the coolant (water) in the reactor, which is then used to produce steam for electricity generation. The complete fission of U-235 gives rise to an energy equivalent of about $2.10^7$ $kW.kg^{-1}$ (equivalent to about 200 MeV per fission), released as kinetic energy distributed between the fission products and the emitted neutrons [11].

To sustain the chain reaction, it is crucial to manage the surplus neutrons generated from the fission of U-235, ensuring that criticality is maintained while preventing a significant increase in neutron generation over time [11]. To control the fission process and maintain a steady rate of energy production, nuclear reactors are equipped with control rods made of materials that absorb neutrons, such as cadmium or boron. By adjusting the position of these control rods within the reactor core, operators can control the number of neutrons available to sustain the chain reaction, thus regulating the power output of the reactor [21].

Nuclear fuel and nuclear reactors are integral to the operation of nuclear power plants, enabling the generation of electricity through controlled nuclear fission. The design, fabrication, and management of nuclear fuel, along with the sophisticated technology of nuclear reactors, ensure the efficient and safe production of nuclear energy.

## 2.3. Spent Nuclear Fuel (SNF)

Spent nuclear fuel (SNF) refers to a fuel that has undergone irradiation within a nuclear reactor. It is the radioactive waste product of nuclear energy production. From the perspective of geologic disposal, SNF comprises a matrix of nearly stoichiometric $UO_2$(s), a complex, heterogenous, redox-sensitive, semiconducting, polycrystalline ceramic material [22,23].Globally, ~ 430 nuclear reactors have collectively produced a spent fuel inventory of roughly 270,000 metric tonnes of heavy metal (mtHM), with an annual increase of ~10,000 mtHM/year [22,24].Johnson and Shoesmith (1988) and Oversby (1994) have extensively explored the structure and composition of various types of spent fuel [25,26]. At the end of the fuel's operational lifespan within the reactor, approximately 96% of the spent nuclear fuel (SNF) remains as $UO_2$. The remaining 4% consists of fission products (e.g. $^{90}Sr$, $^{129}I$, $^{131}I$, $^{137}Cs$,), transuranium elements (e.g. $^{237}Np$, $^{239}Pu$, $^{241}Am$) and activation products (e.g. $^{14}C$, $^{60}Co$, and $^{63}Ni$) [ 21,26].

The composition and radiotoxicity of the fuel evolves over time due to radioactive decay, thermal heat and radiation fields [ 22,27,28]. However, the final composition of the spent fuel is influenced by factors such as the initial fuel type, chemical composition, the level of U-235 enrichment, neutron energy spectrum, and the fuel burn-up [22,27].The distribution of elements within a SNF is not uniform, as shown in Figure.1. These radionuclide elements exhibit heterogeneous distribution throughout the spent fuel, and occur in a variety of phases and forms, ranging from inert gases to relatively stable oxides [29]. Fission product gases such as Kr, Xe and I, occur as finely dispersed bubbles within the fuel grains while other fission products form oxide precipitates of Cs, Ba, Rb and Zr. Along the $UO_2$ grain boundaries, metallic fission products such as Pd, Mo, Tc, Ru, and Rh form metallic precipitates (ε-particles) [23, 29].

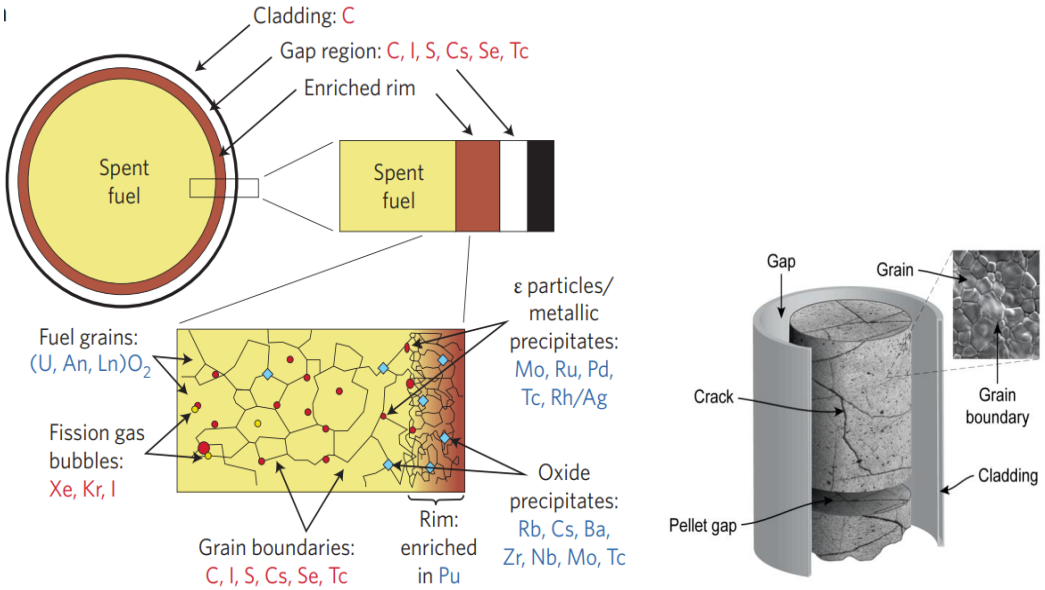


**Figure 1.** Microstructure and the distribution of elements in SNF after irradiation in a reactor. figure adapted from Buck et al. (2004) and Bruno et al. (2006) [22,30].

## 2.4. Management and disposal of radioactive nuclear waste (SNF)

Nuclear power plants, along with various applications in research and medicine generate radioactive waste which needs to be disposed of. The ionizing radiation emitted by this waste poses risks of genetic mutations and cancer, necessitating its safe isolation from humans and the environment [31,32]. The management and safety requirements for handling radioactive waste are determined by its risk potential, primarily influenced by factors such as the nature and intensity of ionizing radiation, heat generation from radioactive decay, radiotoxicity, and the duration of hazard posed to humans and the environment [33]. Radioactive waste is categorized based on its initial radioactivity level (high, intermediate, or low) and radioactive decay rate (long or short-lived). These characteristics determine the timeframe during which the waste may pose risks, guiding the formulation of long-term safety requirements by regulatory authorities for the management of this waste [34].

Most of the radioactivity generated from nuclear power generation arises from spent nuclear fuel as shown in Figure.2 [35].SNF is categorized as a high -level, long lived radioactive nuclear waste requires disposal in a location that is inaccessible to humans and the environment for an extended period of time (at least hundred thousands of years) until its radioactivity decreases to levels deemed safe ( such as natural mined uranium ores) for both humans and the surrounding environment [36]. The scientific consensus today is that deep geological repositories in stable geological formations (GDRs) are a safe, long-term and effective approach for the isolation, management and disposal of SNF [37].

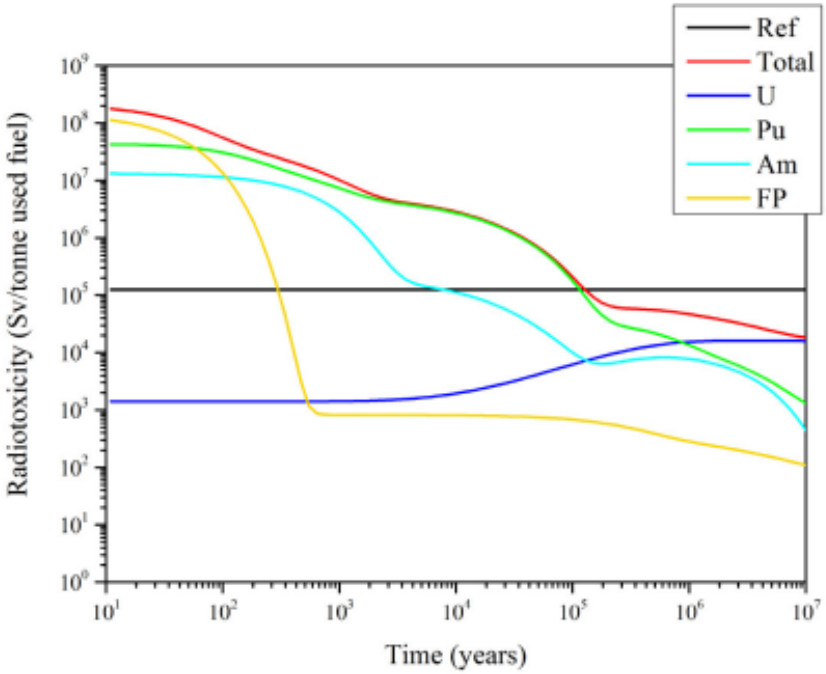


**Figure 2**. Radiotoxicity of spent nuclear fuel (4% enrichment, 45 MWd/kg fuel burnup) with contributions of different actinides elements and fission products [35]. The reference level corresponds to the radiotoxicity of the mined natural uranium.

## 2.5. Deep Geological Repository (DGR)

The direct disposal of SNF in deep underground geological formations is being considered as a management option in several countries such as USA, Sweden, Finland, Canada, UK etc. In Sweden, an estimated amount of 12,000 tons of spent nuclear fuel from Swedish nuclear power plants are currently stored interim awaiting final solution. The Swedish final repository concept known as the KBS-3 method has been proposed for the final storage of this highly radioactive waste [8,9].The primary objective of the KBS-3 repository is the long-term isolation and containment of the spent nuclear fuel from both human intervention and the environment for an extensive period.

The government of Sweden granted Svensk Kärnbränslehantering AB (SKB), a company established in the 1970´s by the country's nuclear industry, approval in late January 2022 to proceed with constructing a deep geological repository (DGR) for management and disposal of spent nuclear fuel (SNF). This decision marks the culmination of over 40 years of research and development, making Sweden the second country, after Finland, to move forward with building a permanent SNF repository. The facility will include a DGR located in Forsmark, Östhammar municipality, along with an encapsulation plant situated near an interim storage facility in CLAB, outside Oskarshamn municipality [9,38].

The planned repository facility, which will be constructed at a depth of 500m illustrated in Figure.3, will employ the KBS-3 containment method developed by SKB. This method involves surrounding the spent fuel with multiple engineered and natural safety barrier systems. These barriers will fulfill two main safety roles: containing the fuel within the canister and, if there's containment breach, retard any potential release from the repository.

These barriers include the spent nuclear fuel form (fuel pellet and cladding tube), copper canisters housing the fuel bundles, each featuring a robust 5 cm thick copper corrosion barrier that spans 5 meters in length and weighs up to 27 tons, along with a load-bearing insert made of nodular cast iron. The sealed canisters measure 4,835 mm in total length with a diameter of 1,050 mm will be positioned in deposition holes designed to withstand corrosion and geological movements. The ability of copper canisters and their cast iron inserts to withstand the mechanical and chemical stresses of the repository environment have been demonstrated through extensive research and testing [9].

Surrounding the canisters will be a bentonite clay buffer, which effectively restricts water flow around the canisters and into the bedrock. Bentonite clay, which swells in contact with water and limits water flow, will provide additional protection against movements in the bedrock. The tunnel system construction and the placement of canisters in the spent fuel repository will happen concurrently over several years in separate operational areas. After all deposition holes in a deposition tunnel are filled, bentonite clay will be used to backfill the tunnel. Ultimately, upon completion of canister deposition, the entire repository will be backfilled [9]. By placing the repository at a depth within a stable geological setting for the long term, the waste is securely isolated from human and near-surface environmental impacts.

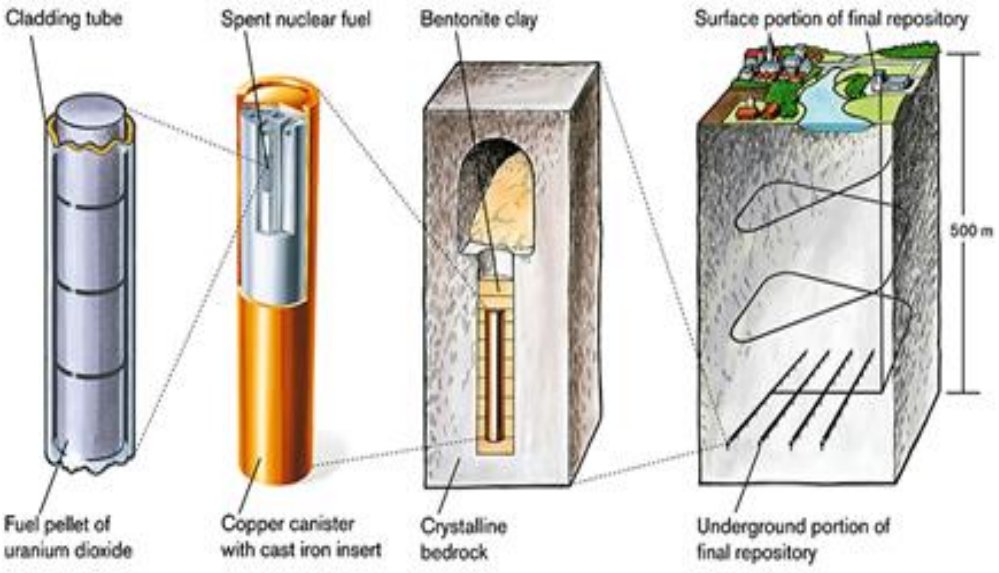


**Figure 3.** The KBS-3 design incorporates safety barrier features such as fuel pellet, copper canister, bentonite clay, and crystalline bedrock. Illustration: Jan Rojmar, Svensk Kärnbränslehantering AB. Reproduced with permission from SKB.

## 2.6. Radiation induced SNF dissolution under disposal condition

While the engineered barrier system design is robust, the intrusion of groundwater to the spent fuel has been addressed in the safety analysis report by SKB [9]. These concerns are primarily related to potential canister failures over an extended period (within the repository environment) due to factors such as erosion of the bentonite clay, corrosion or shear loads. While such failures could compromise the protective function of safety barriers, the likelihood of these scenarios occurring within the first 1000 years after repository closure is extremely low [9,10].

Within a few years after repository closure, all oxygen present will be consumed by reducing minerals and bacteria, resulting in an oxygen-free, reducing environment. Under these anoxic reducing conditions, $UO_2$ (s) the major component of the spent nuclear fuel remains stable with very low solubility in deep groundwaters. The primary mechanism for the transport and migration or release of radioactive nuclides from the spent nuclear fuel (SNF) repository to the surface is most likely through groundwater, which is only feasible in the event of a damaged canister [ 39-41]. Consequently, the release of radionuclides present within the spent fuel would be dependent on the dissolution of $UO_2$ matrix [39]. The dissolution rate would depend on factors such as the composition of the spent fuel, groundwater, as well as the degree of surface oxidation, which is influenced by the redox condition of the solution [39,40 ,42-45].

In the event of breached canisters, the redox conditions of the groundwater, initially reducing within the disposal vault, may be altered to become oxidizing due to the radiolysis of water caused by the radioactivity associated with the spent fuel [39,41]. Radiation emitted from the spent nuclear fuel in contact with water will induce chemical processes in the groundwater (radiolysis of water) resulting in the generation of reactive free radicals and molecular products. This process yields both oxidants ($OH^{\bullet}$ , $H_2O_2$, $HO_2^{\bullet}$ , and $O_2$) and reductants ($e^-_{aq}$, $H^{\bullet}$ and $H_2$) in equal proportions [39].

The radiolytic oxidants generated would alter the prevailing reducing conditions by interacting with the fuel thereby causing the oxidation of the U(IV) to the significantly more soluble U(VI) leading to its oxidative dissolution [46]. $H_2O_2$ is the main radiolytic oxidant species towards $UO_2$, with a relative impact exceeding 99% [47]. The oxidative dissolution of $UO_2$ via reaction with $H_2O_2$ can be described by a two-electron transfer reaction from $H_2O_2$ to U(IV), as illustrated below.

$$UO_2(s) + H_2O_2 \rightarrow UO_2^{2+}(aq) + 2\,OH^- \qquad (1)$$

The oxidation of the $UO_2$ matrix, together with the attachment of aqueous ligands capable of forming strong complexes would enhance the dissolution of the spent fuel matrix [48]. The generation of oxidants depends on factors such as the dose rate, which, in turn, is influenced by variables like fuel age, burnup, and distance to the fuel surface.

It is imperative to conduct further investigation into the water intrusion scenario resulting from the canister breaches, as groundwater serves as the only pathway for radionuclides transport to the biosphere. Also, assessing the potential dissolution and migration of radionuclides from spent nuclear fuel becomes crucial highlighting the significance of this research thesis work.

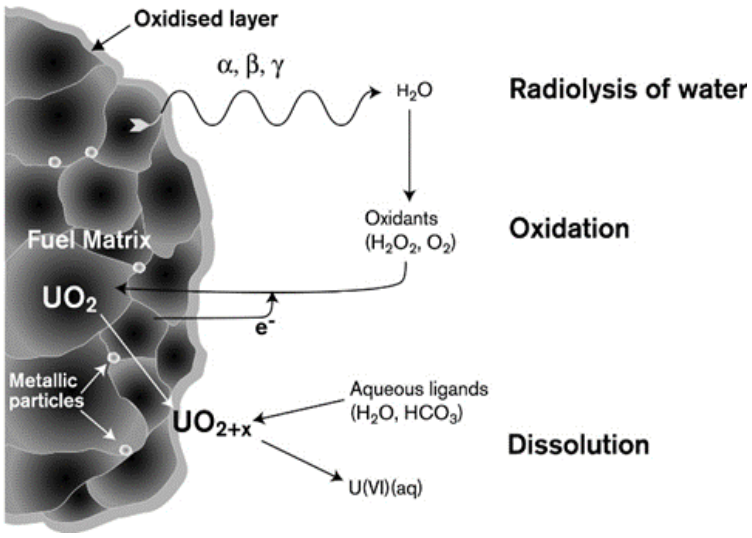


**Figure 4.** The process of oxidative dissolution of spent nuclear fuel caused by radiation. Illustration: Svensk Kärnbränslehantering AB (SKB). Reproduced with permission from SKB.

## 2.7. Effect of potential repository reductants on SNF dissolution

In the Swedish KBS-3 repository design, each spent fuel canister will contain about 14 tons of iron within the outer copper shell making iron a vital component of the canister designs [49,50]. Should a canister lose its integrity within the repository, it is anticipated that anoxic iron corrosion will occur [51].

In the event of water intrusion, the aqueous corrosion of iron would yield various corrosion products, including magnetite, chukanovite, siderite and green rust depending on the redox conditions and the composition of the groundwater. [52-56].However, magnetite has been observed as the predominant anoxic iron corrosion product [55-58]. This anoxic iron corrosion will lead to formation of dissolved Fe(II) and significant amount of molecular $H_2$ as shown in

the reaction (2,3) below, both serving as potential repository reductants or reducing species within disposal- relevant conditions [59-61].

$$Fe(s) + 2H_2O\ (l) \rightleftharpoons Fe(OH)_2\ (aq) + H_2\ (g) \quad (2)$$

$$3Fe(s) + 4H_2O\ (l) \rightleftharpoons Fe_3O_4(s) + 4H_2\ (g) \quad (3)$$

The formation of Fe(II) can result in the consumption of strong oxidants such as $H_2O_2$ through the reactions (4 and 5).

$$Fe(II) + H_2O_2 \rightarrow Fe(III) + OH^{\bullet} + OH^- \quad (4)$$

$$Fe(II) + OH^{\cdot} \rightarrow Fe(III) + H_2O + OH^- \quad (5)$$

This process leads to the reduction of $H_2O_2$ at the fuel surface and the precipitation of oxidized $Fe^{3+}$. Although $H_2$ does not react directly with $H_2O_2$, there is a synergistic effect that exist between $H_2$ and Fe(II) [ 62,63]. $H_2$ rapidly reacts with the hydroxyl radical generated by the $Fe^{2+}$ in reaction (4), resulting in the formation of atomic hydrogen (6), which is a strong reductant (see reaction 6). This can support a $H_2$ driven $H_2O_2$-consuming reaction chain via the hydroxyl radical and atomic hydrogen intermediaries, reactions (6, 7).

$$OH^{\cdot} + H_2 \rightarrow H_2O + H^{\cdot} \quad (6)$$

$$H^{\cdot} + H_2O_2 \rightarrow H_2O + OH^{\cdot} \quad (7)$$

In the performance assessment report, it is assumed that fuel dissolves oxidatively with a very low rate and the oxidized U, Pu and redox sensitive fission products are reduced at the massive iron canisters typical for all European repository concepts [64]. Extensive research has been conducted on the influence of metallic iron and hydrogen on spent nuclear fuel, demonstrating their potential to suppress the oxidative dissolution of the SNF.

Several studies have highlighted that molecular hydrogen can protect the fuel surface from radiolytic oxidants [65-71]. The mechanism behind the effect of hydrogen on spent fuel dissolution involves the kinetic activation of hydrogen on catalytic metallic ε-particles (Mo, Ru, Rh, Tc, Pd), where activated hydrogen actively reduces oxidized uranium or consumes oxidizing species [72-74].Additionally, several studies [52-58] on the impacts of iron and its corrosion products on the corrosion of spent fuel consistently show that the presence of Fe inhibits the corrosion of the fuel and radionuclide release. In conclusion both $Fe^{2+}$ and $H_2$ can interact with the radiolytic oxidants from the fuel surface thereby influencing the fuel corrosion (oxidative dissolution) behaviour. This effect can significantly impact the safety of spent nuclear fuel under disposal condition particularly in the water intrusion scenario [53,75].

## 2.8. Radionuclide co-precipitation and uranium speciation in groundwaters

The bulk of spent fuel composition comprises $UO_2$(s), with a small fraction of other actinides and fission products. Over 95% of these radioactive elements are either dispersed or incorporated into the $UO_2$(s) matrix as solid solution [36,37]. Several works have indicated that in numerous leaching tests conducted with spent fuel in the presence of hydrogen, a decrease in the concentrations of U and other actinides such as Np and Pu has been measured. This

phenomenon has led many authors to conclude that these actinide elements, originating from a pre-oxidized fuel layer, are reduced at the fuel surface and co- precipitate as the corresponding reduced amorphous oxides [39,59,67,69-70].

Coprecipitation has been initially suggested as a mechanism for retaining radionuclides in spent nuclear fuel following the potential corrosion of stored spent fuel under disposal conditions by groundwater [76-78]. The possibility that these radionuclides or actinide ions co-precipitate with each other is high considering the similarity of their ionic radii, ionic charges, coordination, and the fluorite type structures of their tetravalent oxides. In cases where spent fuel undergoes oxidation due to radiolysis, localized oxidizing conditions may prevail at the interface between the fuel matrix and groundwater [79]. While at the near field of the massive iron canister material, it is assumed that reducing conditions of the disposal site will become dominant, as a "redox front" [80].

It has been projected that the formation of solid solutions or coprecipitation of the actinides is expected to occur during their reduction at some distance from the spent fuel surface, where the reducing conditions of the repository prevail again [80].

Given that uranium is by far the most abundant component of the spent fuel, its coprecipitation with minor elements will finally determine their concentrations inside the failed canister and consequently the doses released from the repository. This co-precipitation could play a significant role forming solubility-controlling solids in HLW repository environments. The retention mechanism can have considerable control over the release of radionuclides during the dissolution of spent fuel in a breached geological disposal site by groundwater [80]. Understanding the interaction of this spent fuel under various geological disposal scenarios is essential for evaluating its safety under deep repository conditions. Hence the study of coprecipitation of actinides under disposal condition is therefore highly relevant due to its importance for the repository.

Carbonate which is present in repository relevant groundwater composition is a strong complexing agent for $UO_2^{2+}$ [81]. In the water intrusion scenario, the presence of carbonate would have a significant influence on the dissolution rate of oxidized uranium, as it can form strong soluble complexes with uranyl ion such as $UO_2(CO_3)_3^{4-}$ and $UO_2(CO_3)_2^{2-}$ [81,82]. The carbonate concentration in groundwater is dependent on dissolution of carbonate mineral (calcite),$pCO_2$ and pH of groundwater. The concentration of Calcium ($Ca^{2+}$) in groundwater plays a significant role in the formation and stability of Ca-uranyl-carbonato complexes, which can affect U solubility and mobility under disposal conditions [83]. Calcium, (a ubiquitous component in both seawater and groundwater) can influence the speciation through the formation of the complexes $CaUO_2(CO_3)_3^{2-}$ and $Ca_2UO_2(CO_3)_3$ [84]. Studies have shown that the dominant complex under sea water and groundwaters is the neutral $Ca_2UO_2(CO_3)_3$ complex [85-88].

The presence of a solid Fe(II) containing phase can reduce U(VI), causing precipitation of the reduced U(VI) due to its low solubility [89,90]. Uranyl ion can also adsorb efficiently on iron oxides and hydroxides minerals, but this adsorption decreases with higher calcium concentrations in carbonate solutions, which implies that the formation of $CaUO_2(CO_3)_3^{2-}$ and $Ca_2UO_2(CO_3)_3$ complexes can limits uranyl adsorption on mineral surfaces and may prevents its reduction and precipitation on metallic iron or Fe(II) containing mineral surface [91].

# 3.0. Theory

## 3.1. Coprecipitation phenomena and formation of a solid solution

Coprecipitation, a well-established chemical phenomenon, is becoming increasingly important as it finds broad applications in various fields such as analytical and nuclear chemistry, radiochemical processes, and geochemistry. This process is particularly relevant in understanding radionuclide migration in the geosphere and the formation of multicomponent solid solutions. It involves the simultaneous precipitation of solid compounds from a solution, often resulting in the incorporation of trace elements into the solid precipitate. In a typical coprecipitation process, aqueous metal salts are mixed at ambient or elevated temperatures with a base such as NaOH which acts as a precipitating agent [92,93]. The process is sometimes conducted under an inert atmosphere [94].

During coprecipitation, ions that were initially dissolved in the solution become incorporated into the solid precipitate. This incorporation can occur due to various factors such as similar ionic radii, charge, and chemical properties between the precipitating ions. Several factors influence co-precipitation reactions, such as pH, ionic strength, temperature, the concentration of reactants, solution composition, metal complexation, precipitation rate and the nature of the precipitating agent [92,95]. In the definition recommended by IUPAC, coprecipitation is defined as "the simultaneous precipitation of a normally soluble components with a major component from the same solution." [96]. It is a process that involves the precipitation and subsequent nucleation, crystal growth, coarsening and/or agglomeration process, where minor or trace components build a common structure of mixed composition with the major or host component [97,98].

Solid solution, a term mostly used for metals refers to the uniform mixtures of two or more substances in solid state either at the atomic or molecular level [99]. It is often characterized by a single crystalline structure in which one or more atoms or molecules substitute the other (host atom) without altering the overall structure, although some variation in the lattice parameters may occur [100]. There are two types of solid solutions: substitutional and interstitial. In substitutional solid solutions, solute atoms replace solvent atoms (host atom) within the lattice structure. In interstitial solid solutions, solute atoms occupy the spaces (interstices) between the solvent atoms.

## 3.2. Partition laws governing coprecipitation phenomena

Co-precipitation reactions are commonly described and quantified using a distribution model that relies on an empirical partition coefficient [95].The equilibrium partitioning of components A and B of a solid solution between the aqueous and solid phases can be described in two different ways [77]. The coprecipitation phenomena are governed by two partition laws which establish connections between the molar fractions in the solid Equation.(8) or at the solid surface, Equation.(10) and the total concentration in solution. When equilibrium is attained between the bulk of the solid solution and the aqueous phase, the system adheres to the homogeneous distribution law proposed by Berthelot-Nernst [77,101].

This can be expressed as:

$$\frac{[A](s)}{[B](s)} = \mathrm{D}\ \frac{[A](aq)}{[B](aq)} \qquad (8)$$

Where [A] (aq) and [B](aq) corresponds to the total concentrations in solution of the trace element to the major or host element respectively, while [A](s) and [B](s) represents the mole fractions in the solid phase for the trace element and major element respectively. D signifies the partition or homogenous distribution constant.

Also, the equilibrium constant for Equation.(8) i.e. the distribution constant D describes the bulk composition of the solid solution in equilibrium with the aqueous solution as the quotient of the solubility product constants of the two different solids A(s) and B(s) as such, D can be written as:

$$\mathrm{D} = \frac{Kso[\,B]}{Kso\,[A]} \qquad (9)$$

Where $K_{s0}$ [B] and $K_{s0}$ [A] are the solubility product of the major and minor component respectively.

Homogeneous solid solutions are uniform with absence of concentration gradients, representing a true state of thermodynamic equilibrium. In contrast, it is possible to have heterogeneous distributions of the foreign ions or minor components within the host lattice. Heterogeneous solid solutions may exist in metastable equilibrium with an aqueous solution, exhibiting concentration gradients [102]. In this type of solid solutions, no structural rearrangement has occurred, and distribution equilibrium is only established between the solid surface and the aqueous solution, adhering to the logarithmic distribution law proposed by Doerner-Hoskins [103]. This is formulated as:

$$log\ \frac{[\mathrm{A}](\mathrm{surface})}{[\mathrm{B}](\mathrm{surface})} = \mathrm{k}\log\frac{[A](aq)}{[B](aq)} \qquad (10)$$

$[A]_{(surface)}$ and $[B]_{(surface)}$ represents the mole fractions of the coprecipitated trace and major element respectively at the solid surface. k denotes the partition or heterogeneous distribution constant.

## 3.3. Solubility and hydrolysis of U(IV)

U(IV) is characterized by its low solubility and strong hydrolysis. $UO_2$ can be dissolved in acidic solutions. In regions with low pH, the dominant charged species in solution are $U^{4+}$ and $U(OH)^{3+}$. When the pH is ≤ 2, all U species can remain in solution; however, at pH levels above 2, U begins to hydrolyze and form various species in solution [104]. Hydrolysis which literally means “water splitting” refers to the reaction of metal ions with water that liberate proton and produces hydroxyl complexes in solution [105] .The metal ions properties such as charge, and size determines the strength of these interactions, and the nature of species formed [105].

U in its tetravalent states shows a strong tendency to hydrolyze and form U hydroxide complexes through the following reactions.

$x\ U^{4+} + y\ H_2O \rightleftharpoons U_x(OH)_y^{4x-y} + y\ H^+$

where x = 1, represents the formation of mononuclear hydroxides. The formation of mononuclear U hydroxides species of $U(OH)^{3+}$, $U(OH)_2^{2+}$, $U(OH)_3^{+}$ and $U(OH)_4$ (aq), occurs through the following reactions [104].

$U^{4+} + H_2O(l) \rightleftharpoons U(OH)^{3+} + H^+$ (11)

$U^{4+} + 2\ H_2O(l) \rightleftharpoons U(OH)_2^{2+} + 2\ H^+$ (12)

$U^{4+} + 3\ H_2O(l) \rightleftharpoons U(OH)_3^{+} + 3\ H^+$ (13)

$U^{4+} + 4\ H_2O(l) \rightleftharpoons U(OH)_4\ (aq) + 4\ H^+$ (14)

The overall formation constant for each hydrolyzed species is given by:

$$\beta_{1,x} = \frac{\{U(OH)_x^{(4-x)+}\}}{\{U^{4+}\}\{OH\}^{-x}} \quad (15)$$

where subscript 1, x denotes a mononuclear complex formed in the hydrolysis step x.

At a typical groundwater pH level of 7-9, amorphous (am) $UO_2$ reaches equilibrium at a concentration of approximately ~ 3 x $10^{-9}$ M in its tetravalent state [106].The dissolution or precipitation of $UO_2$(am) can be described with the equilibrium reaction. These dissolution reactions control the solubility of U(IV)[106,107].

$UO_2(am) + 4\ H^+ \rightleftharpoons U^{4+} + 2\ H_2O$ $\log^*K^0_{s,0} = 1.5$ (16)

$U^{4+} + 4\ H_2O(l) \rightleftharpoons U(OH)_4(aq) + 4\ H^+$ $\log^*\beta^0_4 = -10.00$ (17)

$UO_2(am) + 2\ H_2O \rightleftharpoons U(OH)_4(aq)$ $\log K^0_{s,4} = -8.5$ (18)

The equilibrium described by the constant $K_{s,4}$ is the one dominating in the higher pH range. As seen from the equilibrium reaction above, the constant $K_{s,4}$ corresponds to the formation of a neutral species. Tetravalent U precipitates as an amorphous hydrous oxide $UO_2.xH_2O$(am), which is commonly referred to as uranium hydroxide, $U(OH)_4$(s).The dissolution proceeds according to the following:

$U(OH)_4(s) \rightleftharpoons U^{4+} + 4\ OH^-$ (19)

The solubility product for the amorphous form can be described as :

$K^o_{sp} = [U^{4+}]\ [OH^-]^4$ (20)

Neck and Kim have reviewed and published data on the solubility of $UO_2$(am) and selected the solubility product $\log K_{sp,am} = 54.5 \pm 1.0$ [106].The total concentration of metal that determines the solubility of the substance of interest includes the concentration of the metal ion ($Me^{4+}$) and the concentration of all its hydrolysis products given by the relation:

$[Me(IV)]_{total}] = [Me^{4+}] + \sum [Me[OH]_n^{4-n}]$ (21)

## 3.4. Solubility and hydrolysis of Ce(III)

Cerium (Ce) is the second element in the lanthanide series, which is considered as one of the rare-earth metals [108]. Ce commonly exists in two main oxidation states, Ce(III) and Ce(

IV),with stable oxidation state 4+ in aqueous solution, a unique character of the lanthanides series [109]. Ce(III) is stable in the acidic pH region [110]. Trivalent Ce can be precipitated in the pH range of 6 to 7.16 as $Ce(OH)_3(s)$ and would dissolve completely at pH < 4 [111,112].

The following mononuclear hydroxides complexes of Ce(III) and Ce(IV) have been established in several studies e.g. $Ce(OH)^{3+}$,$Ce(OH)^{2+}$,$Ce(OH)_2^{+}$,$Ce(OH)_3(aq)$,$Ce(OH)_2^{2+}$,$Ce(OH)_3^{+}$and $Ce(OH)_4$ aq.

The formation of mononuclear Ce(III) hydroxides species occurs through the following reactions.

$$Ce^{3+} + H_2O(l) \rightleftharpoons Ce(OH)^{2+} + H^{+} \quad (22)$$

$$Ce^{3+} + 2\ H_2O(l) \rightleftharpoons Ce(OH)_2^{+} + 2\ H^{+} \quad (23)$$

$$Ce^{3+} + 3\ H_2O(l) \rightleftharpoons Ce(OH)_3(aq) + 3\ H^{+} \quad (24)$$

In low acidic pH regions, the dominating equilibrium for the dissolution of pure $Ce(OH)_3(s)$ can be described with the equilibrium reaction:

$$Ce(OH)_3(s) + 3\ H^{+} \rightleftharpoons Ce^{3+} + 3\ H_2O(l) \quad (25)$$

since no hydrolytic Ce(III) complexes are expected to exist at very low pH range. The thermodynamic equilibrium constant can be expressed:

$$*K^0_{s0} = \frac{\{Ce^{3+}\}a_w^3}{\{H^+\}^3\ a_{Ce(OH)_3(s)}} \quad (26)$$

where $a_{Ce(OH)_3(s)}$ is the activity of $Ce(OH)_3(s)$ in the solid, $a_w$ represent the activity of water and the curved brackets denote the activities of the species in solution.

Only few reported data for the hydrolysis and solubility of $Ce(OH)_3(s)$ exists. Different values for the solubility product of Ce(III) hydroxide have been reported by a few authors [113-117]. However, from the review of Ekberg and Brown [118] solubility constant of $\log *Ks_{1,0}$ = 18.5±0.5 have been recommended with large associated uncertainty.

# 4.0. Materials and Methods

This chapter presents the materials used in the experimental studies, followed by the descriptions of the analytical instruments used for measurements.

## 4.1. Chemicals and solutions

All solutions utilized in the experimental work were prepared using ultrapure water (MilliQ Advantage, Merck) with a resistivity of 18.2 MΩ.cm. Before use, the water was thoroughly purged with $N_2$ (99.99%) for several hours to remove any residual dissolved $O_2$.Subsequently, the water was transferred into an Ar atmosphere control chamber (glove box) and sealed in a glass container.

For the preparation of the U(IV) stock solution (~111 g/L) for the U-Ce coprecipitation study, reactor- grade uranium metal (sourced from Norway) was dissolved in 12 M HCl (37% ACS reagent, Sigma-Aldrich, Merck). Additionally, 4.6573 g of 99.9% pure $CeCl_3.7H_2O$(Sigma-Aldrich, Merck) was dissolved in 100 ml of ~ 10 M HCl to produce a 0.125 M Ce stock solution. The solution was prepared with a high acidity to simulate an available Pu(IV) stock solution. Sodium dithionite ($Na_2S_2O_4$) (Sigma-Aldrich, Merck) solutions were prepared at concentrations of 10 mM and 20 mM solutions of $Na_2S_2O_4$. A 1 M carbonate- free NaOH solution was prepared using 1 M NaOH Titrisol ampoules (Sigma-Aldrich, Merck).

For the preparation of ionic medium (I=1.0 M) used for the solubility experiment, 4.61308 mmol/ g solution of $NaClO_4$ stock solution was prepared using reagent grade perchloric acid and sodium carbonate, following the laboratory methods developed at Kungliga Tekniska högskolan (KTH) university [119].The $H^+$ concentration in the stock solution was determined using Gran plots (Gran 1952) [120], and the salt concentration was quantified by weighing samples dried at 125 °C .To prepare 1 M $NaClO_4$ solution, a precise measured quantity of stock solution containing 1 mole of $NaClO_4$ (216.77 g) was weighed and transferred into a 1 L volumetric flask, which was then filled to the calibration mark with distilled water.

For the Ca-uranyl-carbonato reduction in the presence of iron study, 10 ppm of U(VI) stock solution was prepared. This stock solution was subsequently diluted with synthetic groundwaters to achieve an initial concentration of 1 ppm ($4.2 \times 10^{-6}$ M).According to the work of Nassar et al. (2016) [121]. $FeCO_3$ used as oxygen trap in the study was synthesized in an autoclave by mixing $FeSO_4 \cdot 7H_2O$, ascorbic acid, and ammonium carbonate in a 1:1:3 molar ratio. The mixture was then allowed to react in 50 mL ultrapure water for 1.5 hours at 140 °C .

### 4.1.1. Iron foils

Iron foils with a purity of ≥ 99.99 % (Thermo Scientific, Alfa Aesar) measuring 0.1 mm in thickness with a surface area of ~1.56 $cm^2$ and a mass of 0.125 g were used in the experiments. Before use, the iron foils were polished with #1200 grit (FEPA-P) SiC sandpaper within an inert-gas glovebox atmosphere to remove any pre-oxidized surface layer.

### 4.1.2. Groundwaters

Synthetic groundwater solutions were prepared using ≥ 99.0% ACS reagent grade chemicals (Sigma-Aldrich, Merck). Two representative synthetic groundwaters analyzed from the repository depth at the Forsmark site designated as “01D” and “02A” were synthesized with concentrations given in Table 1 [122]. Additionally, two other simplified synthetic

groundwaters termed “10-2” and “10-2-Ca” were also studied. The synthetic groundwater “10-2” and “10-2-Ca”contains a concentration of ~10 mM NaCl and 2 mM $NaHCO_3$.To specifically assess the impact of $Ca^{2+}$ , 0.526 mM $CaCO_3$ was added exclusively to the “10-2-Ca” solution. Iron and Manganese were added to the synthetic groundwaters directly inside the glovebox just before the experiment to prevent or minimize the oxidation of these species. The compositions of all four groundwater models are detailed in Table 1.

**Table 1.**

Chemical compositions of the synthetic groundwaters. Concentrations in unit mmol/L.

| Ground-water | $[Na^+]$ | $[K^+]$ | $[Ca^{2+}]$ | $[Mg^{2+}]$ | $[HCO_3^-]$ | $[Cl^-]$ | $[SO_4^{2-}]$ | $[Br^-]$ | $[F^-]$ | [Si] | $[Fe^{2+}]$ | $[Mn^{2+}]$ | $[Sr^{2+}]$ | pH |
|---|---|---|---|---|---|---|---|---|---|---|---|---|---|---|
| 01D | 77.02 | 0.187 | 45.91 | 0.448 | 0.280 | 168.56 | 0.324 | 0.581 | 0.061 | 0.152 | 0.014 | 0.0016 | 0.237 | 8.40 |
| 02A | 96.57 | 0.931 | 22.21 | 10.04 | 2.065 | 148.91 | 5.275 | 0.304 | 0.077 | 0.216 | 0.041 | 0.0377 | 0.099 | 7.19 |
| 10-2 | 12.00 | 0 | 0 | 0 | 2.000 | 10.00 | 0 | 0 | 0 | 0 | 0 | 0 | 0 | 8.34 |
| 10-2-Ca | 10.47 | 0 | 0.526 | 0 | 2.000 | 9.00 | 0 | 0 | 0 | 0 | 0 | 0 | 0 | 8.34 |

## 4.2. Characterization Methods

Analysis of both liquid and solid samples were performed using the instruments described in this section.

### 4.2.1. Solution analysis by Inductively Coupled Plasma Mass- Spectroscopy (ICP-MS)

For the U-Ce coprecipitation study, solution concentrations were determined using an ICP-MS (Inductively Coupled Plasma Mass Spectrometry) instrument (Thermo Scientific, iCAP Q). The samples solutions were diluted with 0.5 M $HNO_3$ (Suprapur, Merck) containing 2 ppb Bi-209 as an internal standard (from a 10-ppm certified standard stock solution (CPAchem). The external calibration series of the analyzed elements in the concentration range of the 0 – 50 ppb were prepared from 10 ppm U and Ce solutions (CPAchem). Samples were analyzed for total U and Ce concentration. All the measurements were performed in standard (STD) modes. The detection limits for U and Ce were 0.1 and 0.01 ppb respectively.

For the Ca-uranyl carbonato reduction in the presence of iron experiment, the total concentration of U, Fe and Ca were determined also with ICP-MS. The measurements were performed using kinetic energy discrimination (KED) mode to be able to discriminate iron and calcium from polyatomic ion interferences [123]. Samples and external calibration series were diluted using 0.5M $HNO_3$ (Suprapur, Merck) containing 10 ppb Th-232 from a 10-ppm certified standard solution (CPAchem) as an internal standard. External calibration series were prepared from 10 ppm Ca, Fe and U solutions (CPAchem) in the 0 – 50 ppb concentration range. All ICP-MS measurements were performed in triplicates. Measurement uncertainties were found to be quite insignificant (< 2% relative uncertainty) for any concentrations above 0.1 ppb, due to the high resolution or detection limits of the ICP-MS instrument. The uncertainties were not plotted in the concentration series since they overlap considerably with the datapoints.

### 4.2.2. Scanning Electron Microscopy with Energy Dispersive X- ray (SEM-EDX)

The U-Ce coprecipitated solid samples were characterized using a Quanta 200 ESEM FEG scanning electron microscope (SEM) equipped with a Schottky field emission gun (FEG) for optimal spatial resolution. Chemical analysis of the solid samples was carried out with an integrated Oxford Inca Energy Dispersive X-ray (EDX) system. The instrument was operated at a voltage of 30 kV in high vacuum mode.

For the Ca-uranyl carbonato reduction in the presence of iron experiment, the iron foil surfaces in contact with the uranyl and synthetic groundwater solutions were subjected to analysis using a Phenom tabletop scanning electron microscope (SEM), which was equipped with Energy Dispersive X-ray (EDX). The instrument was operated at a voltage of 15 kV in high vacuum mode.

### 4.2.3. Powder X-ray Diffraction ( P-XRD)

X-ray diffraction analysis was performed using a BRUKER D2 PHASER instrument equipped with a monochromatic Cu $K_\alpha$ lines ($\lambda_1$ = 1.54184 Å) radiation source covering a 2Θ range from 20 ° to 90° and a LYNXEYE detector. The instrument was operated at a voltage of 30 kV and a current of 10 mA. Diffrac. Topas (V6.0) software provided by Bruker, in addition to the open access JEdit software were used to determine the phase and crystal structure of the co-precipitated solid samples. The international Centre for diffraction data (ICDD) database was used for indexing. The instrument was stationed or kept in the glove box with partial pressure of $O_2 \leq 1$ ppm to prevent oxidation of the samples during handling and measurements. The solid samples were analyzed for phase identification and crystal structure both before and after equilibration.

### 4.2.4. Surface analysis by X-ray Photoelectron Spectroscopy (XPS)

XPS measurements were carried out using a PHI5000 VersaProbe III Scanning XPS Microprobe to determine the oxidation states of the solid samples (U-Ce coprecipitated solids and iron foils) in both studies. The instrument was equipped with a monochromatic aluminium (Al) X-ray source (photon energy = 1486.6 eV) which featured a tuneable beam size ranging from 9 µm and 300 µm in diameter with the beam size set to 100 µm for these experiments. This configuration provided a core level spectra energy resolution of 0.685 eV, with reference to the full width at half maximum (FWHM) of a $Ag3d_{5/2}$ peak measured from an ion sputter-cleaned silver foil. To ensure accurate binding energy (BE) scale calibration, the energy positions of the gold ($Au4f_{7/2}$), silver ($Ag3d_{5/2}$), and copper ($Cu2p_{3/2}$) were aligned at 83.96 eV, 368.21 eV and 932.62 eV, respectively in accordance with ISO 15472:2010 standards. The powdered samples which had uncertain conductivity, were analyse using a dual charge neutralisation technique which involves the use of both an argon ion gun (i.e. +ve) and electron neutralizer (i.e. -ve) to compensate the photoelectron loss during the measurements.

The XPS spectral analysis was carried out in two steps. First, survey scans covering an energy range from 0 to 1350 eV were performed with a step size of 1.0 eV to identify the elemental composition of the samples. Subsequently, narrow scans with a finer step size of 0.1 eV were conducted on the regions of interest to assess the chemical states of the elements present.

The detection limit of the measurements was approximately 1.0 atomic percent, with the majority (95%) of the signal originating from the top few atomic layers of the samples.Data analysis was conducted using the ULVAC-PHI MultiPak™ software (Version 9.7.0.1) with background subtraction performed using the Shirley method. The binding energies were corrected by referencing the adventitious carbon C1s peak at 284.8 eV.

Special care was taken to prevent contamination during sample preparation and transfer. Small pieces of iron foil and powdered samples from the coprecipitated solids were prepared and loaded into an XPS sample holder within a glove box under an inert argon (Ar) atmosphere with oxygen levels below 1 ppm. The samples were then sealed in a vacuum transfer vessel that was compatible with the XPS introduction chamber. This vessel ensured that the inert atmosphere was maintained during transportation from the preparation site to the XPS analysis chamber, effectively minimizing the risk of air and moisture contamination.

### 4.2.5. X-ray Absorption Spectroscopy (XAS) analysis

XAS was used to analyze the oxidation states and local structure surrounding U and Ce in the co-precipitated solid samples. Approximately 20 mg of each solid sample was mixed with boron nitride and covered with Kapton tape. The uranium and cerium $L_3$-edge X-ray absorption data were acquired in transmission mode at ambient temperature on the Balder beamline at the MAX IV Laboratory, Lund University, Sweden [124]. The beamline operated at 3 GeV and 500 mA ran in top-up mode, using a Si (111) double crystal monochromator and mirrors to reject higher harmonics. The solid samples were kept in cells made of 1 mm aluminum frames with Kapton tape as windows. The X-ray absorption spectra were energy calibrated using a chromium metal foil, (5989.0 eV) [125] for Ce measurements, and an yttrium metal foil, (17038.0 eV) [125] for U measurements. Data analysis involved standard techniques for pre-edge subtraction, spline removal, and Fourier transformation, utilizing the EXFSPAK software package [126]. For the curve-fitting process, ab. initio calculated EXAFS parameters, generated by FEFF v. 7.0 [127], were applied.

### 4.2.6. Glove box

All the experiments were conducted in a glovebox with Ar atmosphere (Inert Technology) (99.99% Ar with $\leq$ 1 ppm $O_2$). The glovebox atmosphere is continuously circulated past a catalytic bed that removes $O_2$, maintaining a level of $\leq$ 0.1 ppm throughout the experiments. The glovebox was maintained at a room temperature of 21.0 ± 2.0 °C.

## 4.3. Co-precipitation of Ce(III) oxide with $UO_2$ experimental procedure

An aliquot of acidic U(IV) stock solution was treated with a few mg of uranium grains for some minutes to reduce any potential traces of U(VI), then transferred to a 250 ml centrifuge tube. A 20 mM deoxygenated solution of $Na_2S_2O_4$ solution was added to maintain reducing conditions. To this tube, a calculated aliquot equivalent to 1% acidic Ce(III) stock solution was introduced. The mixture was then titrated with carbonate-free NaOH to precipitate U and Ce as amorphous hydroxides. The carbonate free NaOH solution was added stepwise to the tube until a targeted pH value of 9.5-10 was obtained in the neutralized solution. The formation of solid precipitates was observed as shown in Figure.5.

**Figure 5.** Coprecipitated solid of U and Ce ($Ce_{0.10}U_{0.90}$) after centrifugation and removal of supernatant.

The mixture or co-precipitated solid in the tube was stirred for 15 minutes at 170 rpm on an orbital shaker (PSU-10i), then centrifuged at 12,000 rpm (12,865 g) for 15 minutes using a Beckman Coulter Avanti J-26 SXP. The supernatant was removed, and the precipitate was washed twice with deoxygenated 20 mM $Na_2S_2O_4$ solution adjusted to pH 7 to remove NaCl formed during neutralization. The washed precipitate was aged overnight in 120 ml of 20 mM $Na_2S_2O_4$ solution at pH 7, with continuous mixing on the shaker. After aging, the slurry was centrifuged again at 12,000 rpm for 15 minutes and the supernatant was discarded. The solid was distributed into 50 mL Oak Ridge centrifuge tubes (Thermo Scientific) for solubility measurements, using 0.980 mM $NaClO_4$ and 10 mM $Na_2S_2O_4$ as ionic media. The pH was adjusted between 2 and 13 using carbonate-free NaOH or $HClO_4$ and measured with a combined glass pH electrode calibrated with standard pH buffers.

Two experimental sets were conducted with these precipitates. One with 1% molar Ce concentration and the other with 10% concentration. The remaining slurry was treated with 75 ml of 10 mM $Na_2S_2O_4$ for washing. The precipitate was centrifuged, and the supernatant tested for chloride with $AgNO_3$.This washing step was repeated twice, with the second wash showing the presence of minimal chloride. A final washing step with ultrapure MQ confirmed no chloride presence. The precipitate was left to dry in the glove box for some days before any further analysis of the solids.

For the solubility experiments, pH measurements were taken at equilibration period of 7, 14, 21 and 30 days using combined glass pH electrode calibrated against pH buffers. The 3 M KCl reference solution of the combined pH glass electrode was replaced with a 3 M NaCl solution in order to avoid precipitation of $KClO_4$, and the electrode was calibrated with pH buffers of pH 1 (HCl), 4 (biphtalate), 7 (phosphate) and 10 (KCl / $H_3BO_3$ / NaOH) from Sigma Aldrich. The $-\log[H^+]$ value in the 1 M $NaClO_4$ solutions was calculated through the relationship: $pH_{exp} + \log[H^+] = -0.23 \pm 0.2$ [128].Redox potential measurements using a Pt electrode were inconsistent due to electrode drift, though all the values obtained corresponded to reducing conditions. The solid suspensions were continuously shaken, and aliquots taken at each equilibration period were filtered through 0.20 μm polypropylene membranes and Amicon Ultra-4 centrifugal filters with a 30,000 molecular weight cut-off (NMWL Sigma Aldrich Merck, Millipore Ltd) to effectively separate tiny solids particles from solutions. Pretreatment of filters with sample aliquots minimized sorption losses. The filtered samples were analyzed using ICP-MS.

## 4.4. Reduction of Ca- Uranyl-carbonato complexes in the presence of iron experimental procedure and set-up.

The experiments were conducted in a glovebox with Ar atmosphere (Inert Technology). Initially, 2 ml of 10 ppm U(VI) stock was diluted to 20 ml using synthetic groundwaters in plastic vials, which were then placed in a ~ 2 L glass reaction vessel inside the glovebox. The reaction vessel was equipped with a gas inlet and outlet, enabling continuous flushing with inert gas to maintain a controlled atmosphere throughout all experiments within a batch. Sample solutions were periodically taken, approximately every 48 hours and analyzed throughout the duration of the experiments, which spanned from 750 to 1250 hours (about 1-2 months). The experimental set-up maintained within the inert glove box for the entire period of the experiment is illustrated in Figure.6.

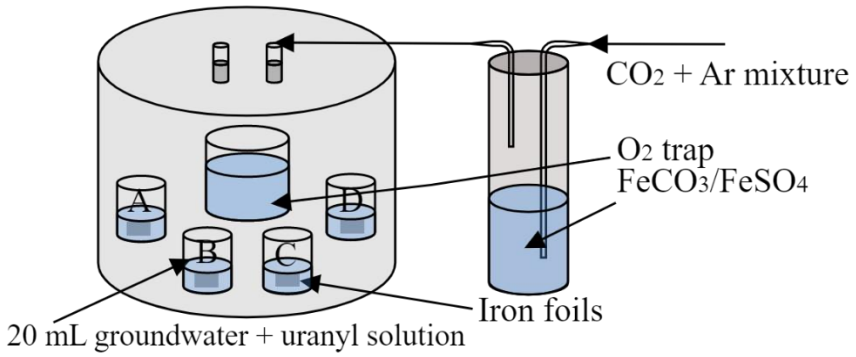


**Figure 6.** Experimental setup for the experiments. The reaction vessels (A, B, C, D) contains the synthesis groundwater solutions with uranyl solutions in the presence of iron foils.

# 5.0. Results

## 5.1. Results from coprecipitation of Ce(III) oxide with $UO_2$ study

To determine whether equilibrium has been reached between the aqueous and solid phases, to identify the nature of solid solutions formed and to develop accurate interpretations of the solubility data. Data obtained from both liquid and solid characterizations were analyzed. The findings are discussed below.

### 5.1.1. Solution concentrations and solubility of the co-precipitates

The behavior of U in equilibrium with the coprecipitated solid containing 1% mole fraction of Ce ($Ce_{0.01}U_{0.99}$) is expected to be quite similar to that of the amorphous $UO_2$(s). Figure.7 presents a comparison of the U concentration data at 30-day period in this present study with solubility measurements of $UO_2$(am) in 1 M NaCl [129].

In the recent Nuclear Energy Agency Thermochemical Database (NEA-TDB) volume on actinides, Grenthe et al. (2020) [130] discuss the solubility study by Fujiwara et al. (2003) [131], which reports data in 1 M $NaClO_4$ but these were actually obtained in 1M NaCl from their previous studies [132]. However, these data were excluded from our comparison as they are slightly higher than those obtained by Rai et al. (1997) [129].

As depicted in Figure. 7 below, the U concentration data are quite similar to those of Rai et al. (1997) in the $-\log[H^+]$ range of 2-4, where a decrease in U concentrations by approximately three orders of magnitude is observed for each unit increase in $-\log[H^+]$. The predominant hydrolysis species for U(IV) in this pH interval is expected to be the first hydrolysis complex $U(OH)^{3+}$, as indicated by several studies on $UO_2$(am) solubility. Therefore, the relevant equilibrium reaction for $UO_2$(am) with solution in this pH range is:

$$UO_2(am) + 3\ H^+ \rightleftharpoons U(OH)^{3+} + H_2O(l) \qquad (27)$$

$$*K_{s3} = [U(OH)^{3+}]\ [H^+]^{-3} \qquad (28)$$

The concentrations of U from several spent fuel leaching test conducted at a pH around 8 [39,59,69] along with the lower boundary of the reported solubility for $UO_2$(am) in this pH range (Grenthe et al. 2020, log [U] = –8.5±1) correspond well with the U concentrations observed at –log[H+] values greater than 4 in this study.

The constant $\log K^0_{s,4} = -8.5$ corresponds to the equilibrium $UO_2(am) + 2\ H_2O = U(OH)_4(aq)$, which has practically no ionic strength dependence. This value of –8.5 has also been reported even in the presence of higher ionic strength of 5 M NaCl [133]. No attempt was made in the present study to verify the oxidation state of U or Ce at such low concentrations, the U data obtained represent some of the lowest reported in literature for similar systems. This suggests the absence of U(VI), and if uranium is not oxidized, it is reasonable to infer that cerium remains in a reduced state as well. These solubility data indicate that the solubility controlling solids in this study are most likely amorphous.

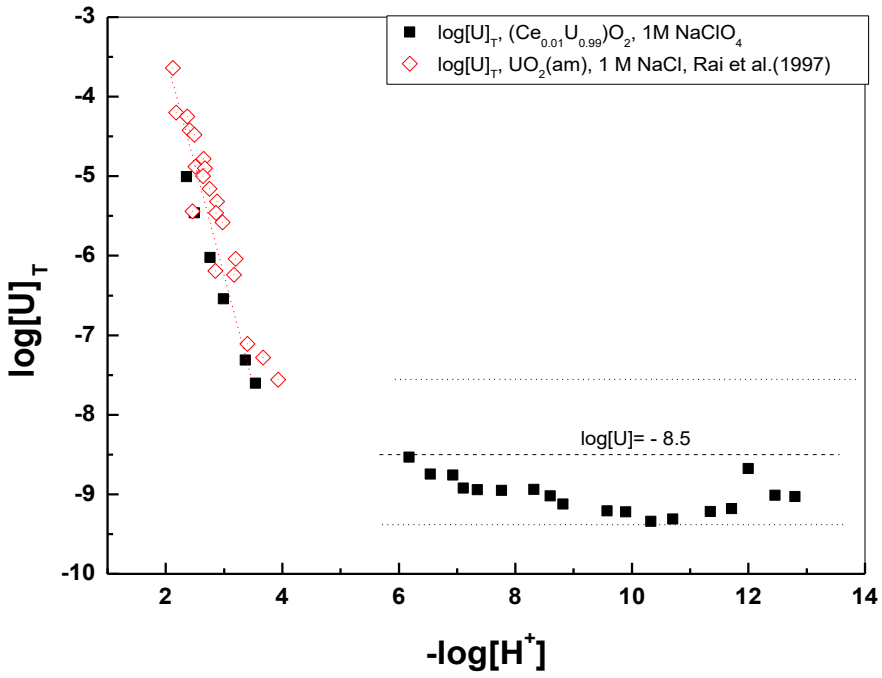


**Figure 7.** U concentrations in equilibrium with the $Ce_{0.01}U_{0.99}$ solid solution at 30 days. The dotted line with slope -3 is derived from Figure.5 in Rai et al. (1997) [129], while the horizontal dotted lines represent log[U] = –8.5±1. The data from Rai et al.(1997) corresponds to an equilibration period of 8-420 days.

### 5.1.2. Ce concentrations in equilibrium with the co-precipitate

The measured Ce(III) concentrations in equilibrium with the $Ce_{0.01}U_{0.99}$ co-precipitate presented in Figure.8 are slightly less than an order of magnitude lower than the corresponding U concentrations at pH levels above 6. In the pH range corresponding to –log [H+] of 2-4 , the Ce concentration decreases by more than an order of magnitude at the lowest measured pH, with the decrease becoming less pronounced as the pH increases.

This indicates that the presence of pure $Ce(OH)_3(s)$ in the solid can be ruled out, as it would dissolve completely within this pH range, resulting in much higher Ce concentrations than those observed. The measured Ce concentrations also clearly suggest that the co-precipitate does not behave as a homogeneous ideal solid solution, since, in such a case, the Ce concentration would decrease proportionally to its mole fraction (0.01) relative to the concentrations in equilibrium with pure solid $Ce(OH)_3(s)$. Additionally, the formation of solid solutions can significantly affect the measured concentration of Ce, which is the minor component in the co-precipitated solid.

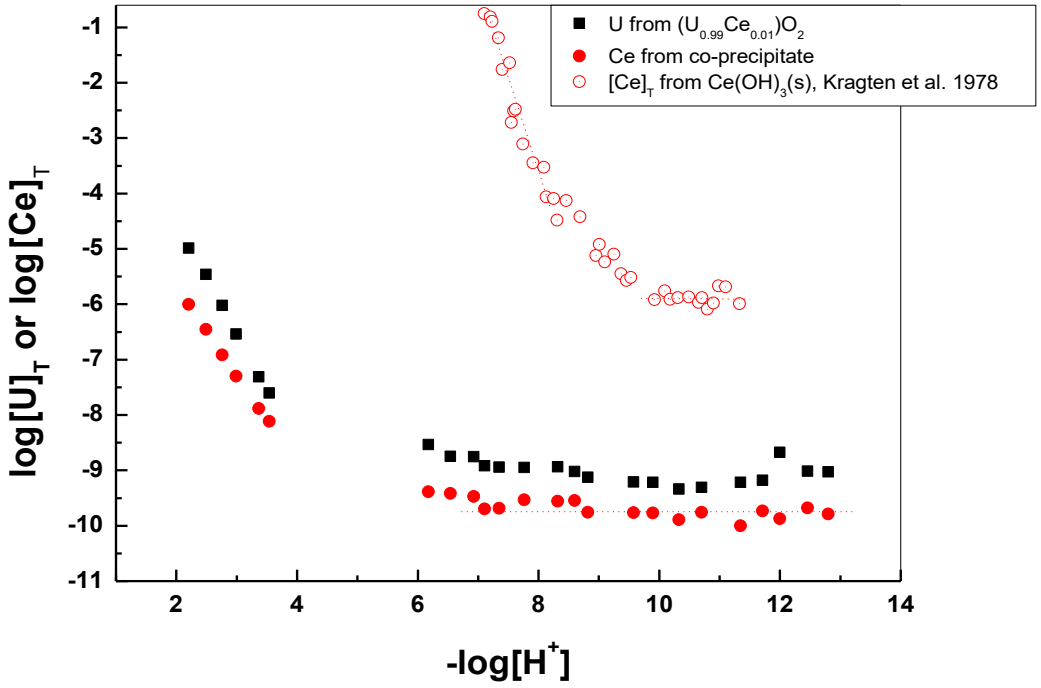


**Figure 8**. Concentrations of Ce and U in equilibrium with $Ce_{0.01}U_{0.99}$ oxide co-precipitate compared with concentrations of Ce in equilibrium with $Ce(OH)_3(s)$ (Kragten and Denkop-Weaver, 1978) at 1 M $NaClO_4$.

Based on Kragten and Denkop-Weaver's 1978 data, $Ce(OH)_3(s)$ in 1 M $NaClO_4$ [112] begins to precipitate at pH about 7 and dissolves completely at a pH less than 4.

At equilibrium, the chemical potential (μ) of each component in the $UO_2.xH_2O(s)$-$Ce(OH)_3(s)$-$H_2O$ system must be equal in both the solid and aqueous phase such $\mu^s$ $(Ce(OH)_3)$ = $\mu^{aq}$ $(Ce(OH)_3)$. In the present study, the concentration data for Ce and U in equilibrium with the mixed oxide phase for two pH ranges, where different aqueous species are expected: –log[$H^+$] 2.2-3.6 and –log[H+] 6.5-12.8.

The predominant equilibrium governing the dissolution of $Ce(OH)_3(s)$ in the low pH range 2.2-3.6 is represented by the reaction:

$$Ce(OH)_3(s) + 3\ H^+ \rightleftharpoons Ce^{3+} + 3\ H_2O(l) \qquad (29)$$

Within this pH range , the formation of hydrolytic Ce(III) complexes are not expected to exist. The thermodynamic equilibrium constant for $Ce(OH)_3$ in both the coprecipitate and the solution can be expressed as follows:

$$*K^0_{s0} = \frac{\{Ce^{3+}\}a_w^3}{\{H^+\}^3\ a_{Ce(OH)_3(s)}} \qquad (30)$$

where $a_{Ce(OH)_3(s)}$ represents the activity of $Ce(OH)_3(s)$ in the solid solution and the curly brackets indicates the activities of the species in solution. Based on Equation.(30), the concentration of Ce in equilibrium with the coprecipitate in 1 M $NaClO_4$ is given by :

$$\log [Ce^{3+}] = \log \left(*K^{0}_{s0} \frac{\gamma^{3}_{H^+}}{\gamma_{Ce^{3+}} a^{3}_{w}}\right) - 3(-\log[H^+]) + \log a_{Ce(OH)_{3(s)}} \qquad (31)$$

where the constant activity coefficients and the activity of water in 1 M $NaClO_4$ are included in the conditional constant $*K_{s0}$.

The conditional solubility product $*K_{s0}$ for $Ce(OH)_3(s)$ in 1 M $NaClO_4$ was determined by Kragten and Denkop-Weaver (1978) as:

$$\log *K_{s0}(1\ M\ NaClO_4) = \log [Ce^{3+}] / [H^+]^3 = 20.1 \qquad (32)$$

incorporating the constant activity coefficients and the activity of water in 1 M $NaClO_4$ into the conditional constant $*K_{s0}$, Equation.(30) for the coprecipitate in 1 M $NaClO_4$ can be expressed as:

$$\log [Ce^{3+}] = \log *K_{s0} - 3(-\log[H^+]) + \log a_{Ce(OH)_{3(s)}} \qquad (33)$$

At constant temperature, pressure and composition, the activity of remains unchanged if the free energy of the solid is constant. While aging of the precipitate usually lowers the free energy of the solid, this reduction was minimal over a 30- days period in our study (see Figure.22). The activity of $Ce(OH)_3(s)$ in the solid solution can be estimated by introducing a solid phase composition dependent constant denoted $K_x$, where x represents the mole fraction of Ce in the solid:

$$\log K_x = \log *K_{s0} + \log a_{Ce(OH)_3(s)} \qquad (34)$$

The constant $K_x$ equals $*K_{s0}$ when $Ce(OH)_3(s)$ is in its standard state, i.e. as pure $Ce(OH)_3(s)$. By combining Equations. (33) and (34) the expression for the constant $K_x$ within this log $[H^+]$ range can be written as:

$$\log [Ce^{3+}] = \log K_x - 3(-\log[H^+]) \qquad (35)$$

by fitting the log $[Ce^{3+}]$ data in the acidic $-\log [H^+]$ range to a line with a slope of –3 and extrapolating to $-\log[H^+] = 0$. The constants $K_x$ can be evaluated, as illustrated in Equation. (35). In this low pH range, the formation of hydrolyzed $Ce(OH)^{2+}$ species is considered unlikely, although the Ce data yield a slope significantly closer to 2 than to 3. This discrepancy seems more to be due to the evaluation of the solubility of a solid which cannot exist in this pH range. To estimate an approximate range of $K_x$ values, lines with a slope of –3 were used to calculate $K_x$ by passing through each individual Ce concentration point. The results are presented in Table 2.

**Table 2**.

Estimates of log $K_x$, $a_{Ce(OH)_3(s)}$ and $\lambda_{Ce(OH)_3(s)}$ derived from data in the $-\log[H^+]$ range 2.2-3.6.

| $X_{Ce(OH)_3(s)}$ | log $K_x$ | log $a_{Ce(OH)_3(s)}$ | log $\lambda_{Ce(OH)_3(s)}$ |
|---|---|---|---|
| 1 | 20.1 | 0.00 | 0.00 |
| 0.1 | 2.5±0.7 | –17.6 ±0.7 | –16.6±0.7 |
| 0.01 | 2.3±0.7 | –17.8±0.7 | –15.8±0.7 |

The values obtained are approximately 18 orders of magnitude lower than the estimated by Kragten and Denkop-Weaver (1978) for the pH range where $Ce(OH)_3(s)$ exists.

The activities of $Ce(OH)_3(s)$ in the solid phase were determined by subtracting 20.1 ($\log {}^*K_{s0}$) from the $\log K_x$ values (see Equation.(34)). Estimates of the equilibrium activities are also provided in Table 2. The activity coefficients of the solid ($\lambda$) were calculated from activity and composition data of the solids using:

$$a_{Ce(OH)_3(s)} = x\ \lambda_{Ce(OH)_3(s)} \qquad (36)$$

As presented in Table 2, the values of $K_x$ shows a slight increase with x for the two values investigated in this study, indicating that they behave thermodynamically as solid solutions. For both compositions investigated, Ce concentrations at equilibrium are consistently lower than those of U across the entire pH range.

These data are not recommended due to the significant uncertainty in determining the conditional solubility product of $Ce(OH)_3(s)$ from the co-precipitate and related parameters within a pH range where pure $Ce(OH)_3(s)$ cannot exist. They also differ considerably from the data obtained in the higher pH range which will be discussed subsequently.

### 5.1.3. Equilibrium Ce concentrations with co-precipitate at high pH values

For $-\log[H^+]$ values greater than 9.9, the solubility of pure $Ce(OH)_3(s)$ in 1 M $NaClO_4$ remains constant at $\log [Ce]_T = -5.9$ reflecting the dominance of the species $Ce(OH)_3(aq)$ in solution. Assuming that $Ce(OH)_3(aq)$ is the major species in solution, the following relationship holds:

$$\log [Ce]_T = \log {}^*K_{s0} + \log {}^*\beta_3 \qquad (37)$$

where ${}^*\beta_3$ is the constant at 1 M $NaClO_4$ corresponding to the equilibrium:

$$Ce^{3+} + 3\ H_2O(l) \rightleftharpoons Ce(OH)_3(aq) + 3\ H^+ \qquad (38)$$

The equilibrium Ce concentrations with mixed Ce and $UO_2$ coprecipitates at high pH values are significantly lower than $\log [Ce] = -5.9$ as depicted in Figure.8 and 9. This decrease is attributed to the activity of $Ce(OH)_3(s)$ within the mixed co-precipitate. In this case, we have

$$\log [Ce] = \log K_x + \log {}^*\beta_3 \qquad (39)$$

Substituting the value of $\log {}^*\beta_3 = -26$ (as determined by Kragten and Denkop-Weaver (1978) in 1 M $NaClO_4$) allows for the determination of $\log K_{0.01}$ and $\log K_{0.1}$ from the Ce concentrations at high pH range in equilibrium with the corresponding solids. As shown in Figure.8 and 9, Ce concentrations at pH levels above 9.5 are completely governed by congruent dissolution with $UO_2(s)$ exhibiting a constant decrease with relative to U concentrations.

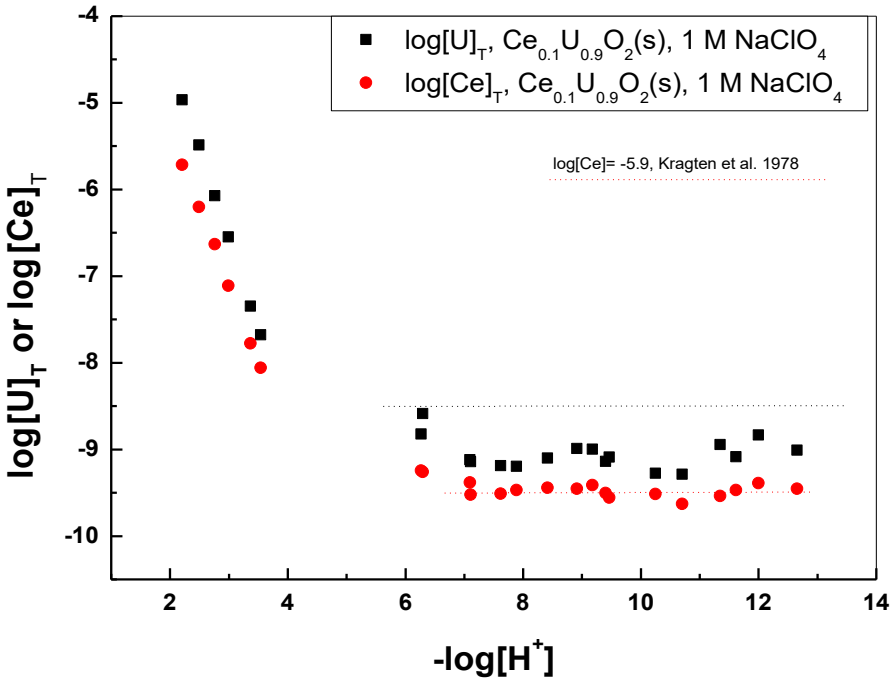


**Figure 9**. Concentrations of Ce and U in equilibrium with $Ce_{0.10}U_{0.90}$ oxide co-precipitate. The dotted lines in the basic range indicate the solubility of $UO_2(s)$, log[U] = –8.5 and the horizontal part of Ce concentrations for the pure oxide and the coprecipitate.

Table 3 presents the values of $K_x$ determined from Ce concentrations in equilibrium with the coprecipitates for $-\log[H^+] > 9.5$, along with the activity and activity coefficients λ of $Ce(OH)_3$ in the coprecipitates. As illustrated in Figure.8 and 9, the horizontal part of Ce(III) concentrations in equilibrium with the coprecipitate extends even to the $-\log[H^+] = 6 - 9.5$ interval, where the solubility of pure $Ce(OH)_3(s)$ increases steeply due to the presence of $Ce(OH)_2^+$, $Ce(OH)^{2+}$ or $Ce^{3+}$species. This further indication that the release of Ce(III) from the co-precipitate is completely dominated by the release of uranium.

**Table 3.**

Values of log $K_x$, $a_{Ce(OH)_3(s)}$ and $\lambda_{Ce(OH)_3(s)}$ estimated from data $-\log [H^+] > 9.5$.

| $X_{Ce(OH)_3}$ | log $K_x$ | log $a_{Ce(OH)_3(s)}$ | log $\lambda_{Ce(OH)_3(s)}$ |
|---|---|---|---|
| 1 | 20.1 | 0.00 | 0.00 |
| 0.1 | 16.5 | –3.6 | –2.6 |
| 0.01 | 16.3 | –3.8 | –1.8 |

As shown in Table 3, the values of $K_x$ increase but very slightly with x for the two values of x investigated in this study. The activity coefficients for $Ce(OH)_3$ in the coprecipitate are negative and significantly less than 1, indicating highly favorable mixing properties.

The old data from Kragten and Denkop-Weaver (1978) were utilized in the data analysis because they are the only available data on Ce(III) solubility and hydrolysis in 1 M NaClO4,

and they align with the conditions of freshly precipitated Ce(OH)3(s) equilibrated for one week to one month similar to our co precipitates study.

To compare the Kragten and Denkop-Weaver (1978) data with more recent lanthanide hydrolysis reviews, the data were extrapolated to zero ionic strength using the Specific Ion Interaction Theory (SIT) approach. The resulting value of the solubility product at infinite dilution (log $*K_{s1}^0 = 18.8$ ) and hydrolysis constants for the $Ce(OH)_3(aq)$ ( log $*\beta^0_3 = -24.7$) align well with more recent studies [118,134] indicating the validity of the older data. Although a full review of Ce-hydrolysis was outside the scope of this study, the comparisons suggest that the data used are reasonable and reliable.

## 5.2. Equilibrium distribution between the solid and aqueous phase

When equilibrium is achieved between the solid phase and the aqueous solution, the distribution of components between these phases adheres to the Berthelot-Nernst homogeneous distribution law as expressed in Equation.(40).

The plot of the normalized concentrations of Ce relative to U concentration have quite some spreads, especially at the low, –log $[H^+]$ range but show that the Ce release from the solid matrix is totally controlled by uranium dissolution and does not vary with time, signifying a congruent release process. According to the Berthelot-Nernst homogeneous distribution law, the distribution factor [135]

$$\frac{[Ce(III)]_{(s)}}{[U(IV)]_{(s)}} = D\frac{[Ce(III)]_{(aq)}}{[U(IV)]_{(aq)}} \qquad (40)$$

was calculated for different compositions and results in D = 0.05 for the $Ce_{0.01}U_{0.99}$ solid and D = 0.27 for the $Ce_{0.1}U_{0.9}$ solid.

The distribution coefficients determined experimentally in Equation.(40). differs from the solubility product ratio because the ratio of the activity coefficients of the solid phase components cannot be assumed to be unity. The distribution law does not account for the speciation of components in the aqueous phase or the activities of the resulting solids, which limits its thermodynamic accuracy. To make valid comparisons between distribution coefficients from different experiments, it is essential to consider the specific conditions under which each experiment was conducted [102].

## 5.3. Characterization of solid phases

### 5.3.1. Total chemical analysis

The total molar ratios of U and Ce in the solids samples were measured both before and after equilibration. Solid samples, weighing a few milligrams, were completely dissolved in 2 M $HNO_3$ and the resulting solution was analyzed for U and Ce concentrations using ICP-MS.

After 93-days of equilibration with solution at pH 8.2, the composition of the solid phase was quite similar to the pre-equilibrated solid, as presented in Table 4 . The analysis also conducted after 30 days of equilibration shows consistent results with those from the 93- day period. The extended equilibration period was selected based on the approach of Rai et al. (2004) [136], who reported solid analyses for a 238-day equilibration period compared to solubility data

obtained over 38 days. These data provides accurate compositions of the solids, which are essential for interpreting and understanding the solubility data presented in this study.

**Table 4**.

Analytical molar fractions of U and Ce in the initial and equilibrated solids.

| Target composition | Before equilibration | | 93 days of equilibration | |
|---|---|---|---|---|
| $Ce_xU_{1-x}$ | Ce | U | Ce | U |
| $Ce_{0.01}U_{0.99}$ | 0.01 | 0.99 | 0.01 | 0.99 |
| $Ce_{0.10}U_{0.90}$ | 0.09 | 0.90 | 0.09 | 0.90 |

## 5.3.2. SEM-EDX results

The U-Ce solid samples were examined by SEM-EDX in the back scattered electron mode before and after equilibration. The resulting micrographs obtained show that the solids exhibit a uniform appearance ( see Figure.10) and no distinct phases can be observed thereby excluding the presence of higher concentrations of U or Ce in specific area.

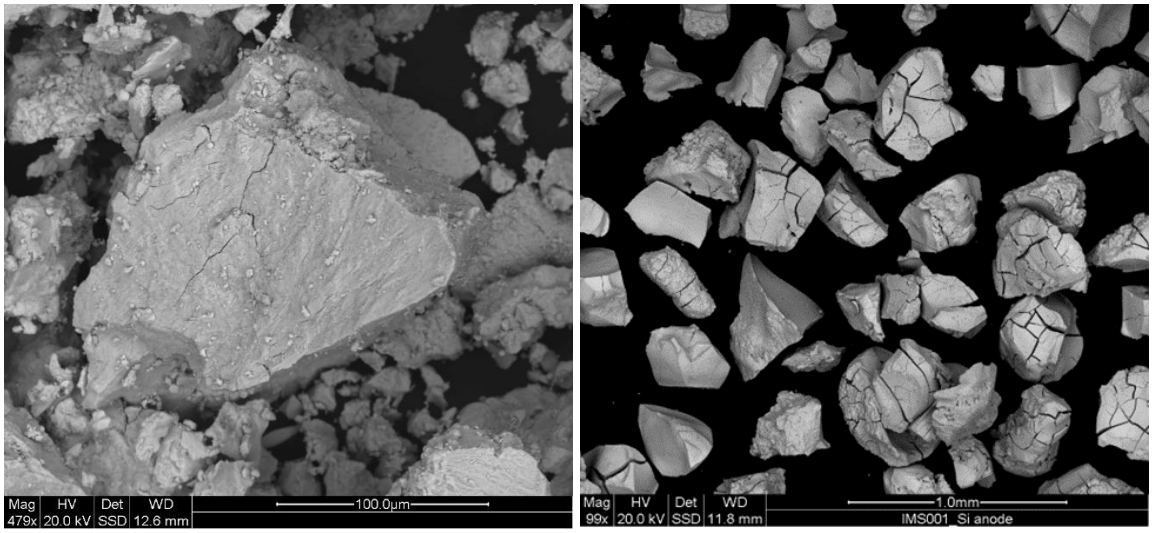

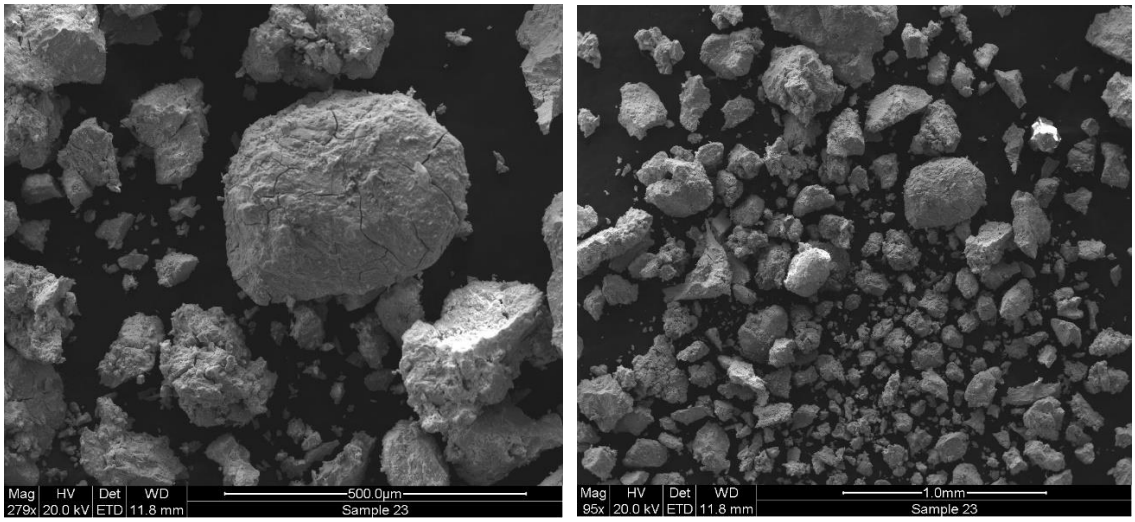


**Figure 10**. SEM micrographs of solid samples before and after equilibration in $NaClO_4$ solutions [$Ce_{0.01}U_{0.99}$ , top figure; $Ce_{0.10}U_{0.90}$, bottom figure].

The $Ce_{0.01}U_{0.99}$ solid samples were below the detection threshold for the EDX analysis. In contrast, EDX analyses of the $Ce_{0.10}U_{0.90}$ solid samples revealed that U and Ce are uniformly distributed in the solid sample. The analysis began with an initial scan of the powder in the SEM sample holder, followed by a detailed examination of various regions of interest, including agglomerates and other features. Based on the EDX results, homogeneity was assumed in all the area investigated, which showed both U and Ce are homogeneously distributed, as illustrated in Figures.11 and 13.

It can be concluded that the solid sample comprises of a single phase rather than a mixture of two different solid phases. The uniform distribution of U and Ce in the corresponding EDX mappings suggests that the solid samples most likely form a solid solution. No other phases were detected in the solids after equilibration and the same homogeneous distribution of U and Ce was observed in the solid after equilibration (see Figure.13).

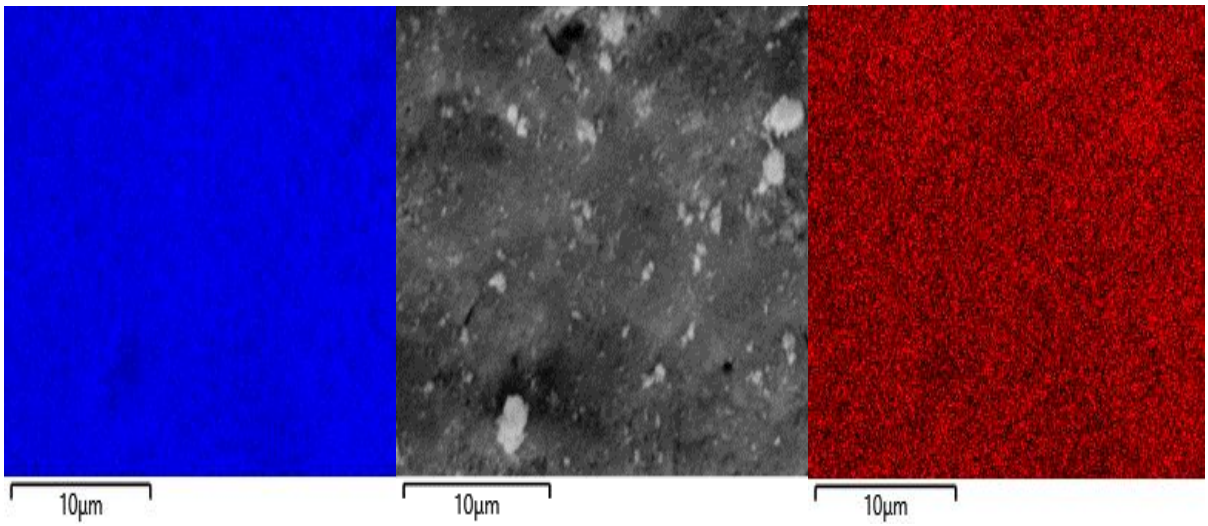


**Figure 11**. SEM micrograph of ($Ce_{0.10}U_{0.90}$) $O_{2\pm x}$ solid (center) and SEM-EDX U mapping (left) and Ce mapping (right) of the same area. Analysis made before equilibration.

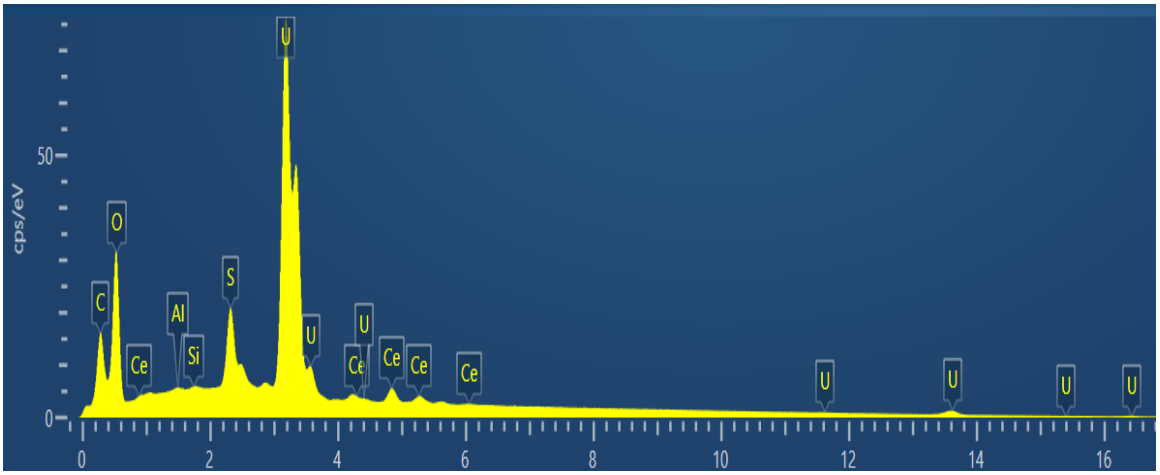


**Figure 12.** SEM-EDX spectrum of the $Ce_{0.10}U_{0.90}$ solid. Solid after equilibration, S originates from dithionite.

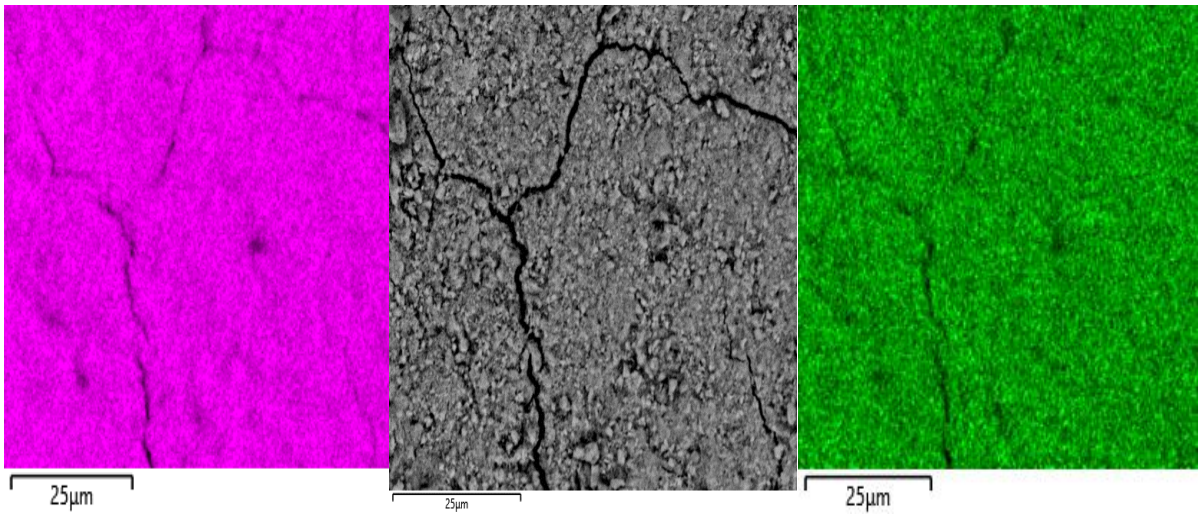


**Figure 13.** SEM micrograph of $(Ce_{0.10}U_{0.90})$ $O_{2\pm x}$ solid (center) and SEM-EDX U mapping (left) and Ce mapping (right) of the same area. Analysis made after equilibration.

### 5.3.3. XRD results

Both before and after equilibration the solid´s diffraction peaks were broad and exhibit a similar appearance. The representative solids samples show broad peaks and not well-defined peaks. The solid precipitates peaks indicate that the solids are primarily amorphous, and presence of micro crystallinity cannot be completely ruled out. It can be concluded that the solubility controlling solids are amorphous.

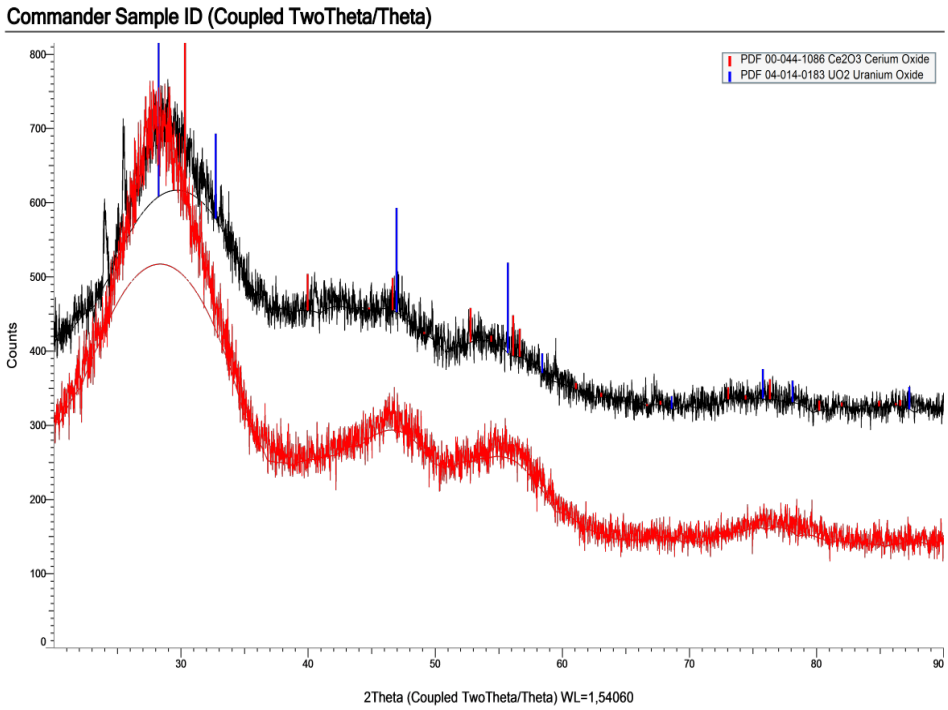


**Figure 14**. XRD pattern of the $Ce_{0.10}U_{0.90}$ solid before (upper) and after (lower) equilibration.

The samples sintered at 900 °C under reducing atmosphere exhibited well-defined crystalline narrow peaks for both $Ce_{0.01}U_{0.99.}$ and $Ce_{0.10}U_{0.90}$ solid samples, as shown in Figure.15.

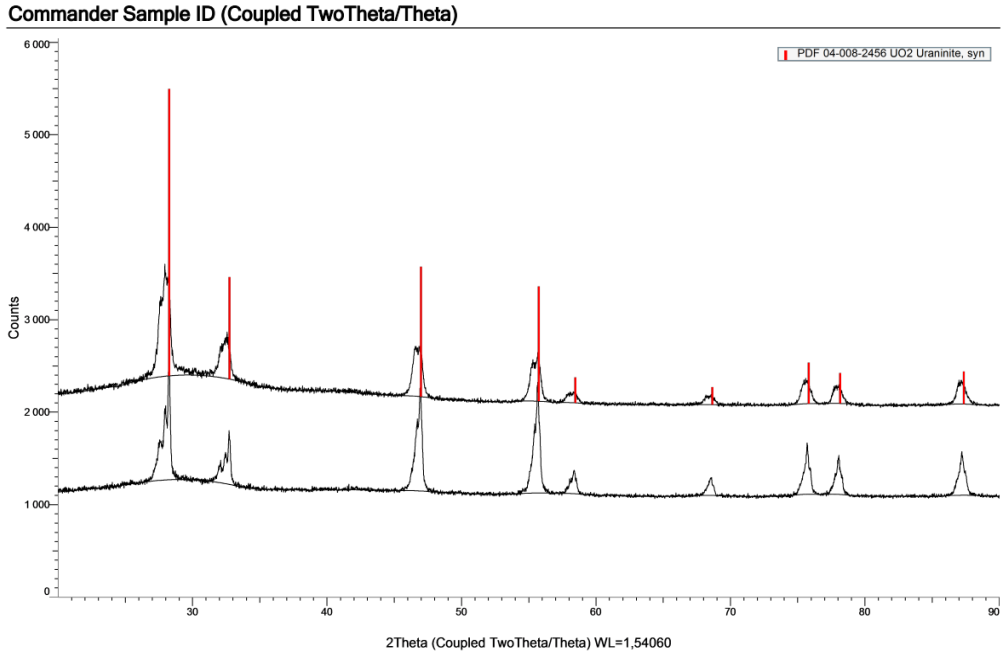


**Figure 15**. U-Ce equilibrated solid heated at 900 °C under reducing conditions. The upper pattern is for $Ce_{0.10}U_{0.90}$ while lower pattern is for $Ce_{0.01}U_{0.99.}$

The lattice parameters of the U-Ce coprecipitates sintered at 900 °C were refined using the GSAS-II software [137]. According to Kleykamp (1993) [138], the lattice parameter of the solid solution decreases as compared to pure $UO_2$ as the Ce content increases in the

stoichiometric solids. For Ce, the relationship for the lattice parameter of the solid solution (a) is related to the mole fraction of Ce (x) and the lattice parameter of $UO_{2.00}$ by the relationship [139].

$$a(Ce_xU_{1-x}O_2) = 5.47127\ Å - 0.058x \qquad (41)$$

where the lattice parameter of $UO_{2.00}$ is 5.47127 Å [140].

**Table 5.**

Lattice parameters for the Ce(III)-U(IV) coprecipitates sintered at 900 °C.

| Composition | Expected from Eq. (34) | a (Å) refined |
|---|---|---|
| $UO_{2.00}$ | - | 5.47127 |
| $Ce_{0.01}U_{0.99}$ | 5.4707 | 5.4709 |
| $Ce_{0.09}U_{0.90}$ | 5.4655 | 5.4660 |

The refined values for lattice parameters as shown in Table 5. are in good agreement with the expected trend for the two solid solutions investigated and show a linear decrease of the cell parameter with Ce content, suggesting a near stoichiometric solid solutions formed in our case; however, the ratio O/M was not investigated in this study.

As the Ce content in the solid solution increases, the lattice parameter of the solid solution decreases when compared to pure $UO_2$. These reduction in the lattice parameter are usually attributed to alterations in the $UO_2$ stoichiometry or the presence of oxygen vacancies which can occur due to the substitution of U with lower charge cation such as $Ce^{3+}$.This substitution can lead to either the formation of $O_2$ vacancies or an increase in the oxidation state of U [141].

## 5.3.4. XPS results

### 5.3.4.1. XPS analysis of the $Ce_{0.01}U_{0.99}$ solid sample

Surface analysis of the $Ce_{0.01}U_{0.99}$ solid shows that the Ce content is below the system detection limit of the instrument (i.e. 1.0 at. %) and resulting in no detectable features across the entire range. As shown in the narrow scan of the Ce3d region (Figure.16a), no significant spectral lines are observed. However, a high resolution scan in the U4f region (Figure.16b) shows the presence of U(IV) state indicated by a $U4f_{7/2}$ peak at 380.5 eV, a spin-orbit splitting of 10.90 eV with the $U4f_{5/2}$ peak, and a clear indication of the satellite peaks from each doublet [149].The absence of a $U4f_{7/2}$ at 381.0 eV or higher (Hanson et al. (2021) [142], Ilton and Bagus (2011) [143]), indicates that the U(VI) state is either absent, or below the detection limit of XPS. This confirms the presence of U(IV) oxide in the $Ce_{0.01}U_{0.99}$ sample.

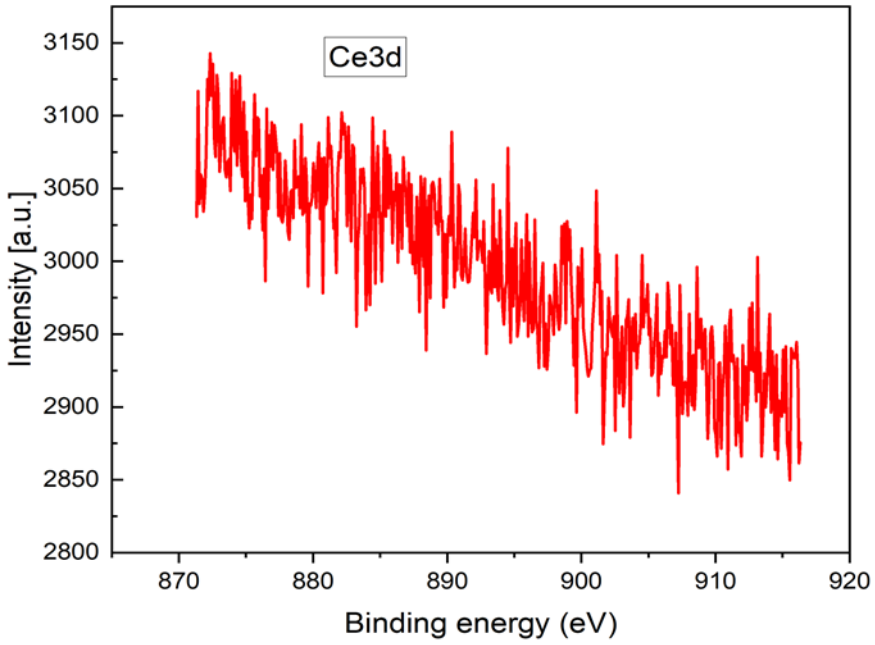


**Figure 16a.** High resolution XPS scans in the Ce3d region for the $Ce_{0.01}U_{0.99}$ solid.

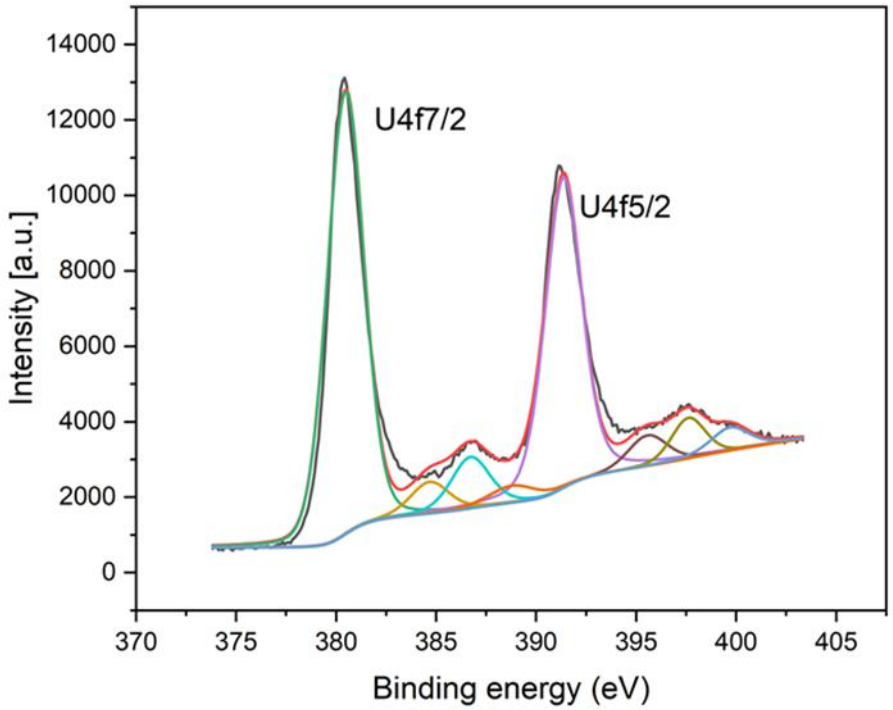


**Figure 16b**. High resolution XPS scans in the U4f region for the $Ce_{0.01}U_{0.99}$ solid.

### 5.3.4.2. XPS analysis of the $Ce_{0.10}$ $U_{0.90}$ solid sample

Based on the surface analysis of the $Ce_{0.10}U_{0.90}$ solid, the high-resolution XPS scan in the Ce3d region (Figure.17a) shows 2 pairs of spin-orbit doublets of $Ce3d_{5/2}$ and $Ce3d_{3/2}$, corresponding to the characteristic feature of the Ce(III) state [144]. Similarly, the high- resolution XPS scan in the U4f region (Figure.17b) shows the presence of U(IV) state, indicated by a $U4f_{7/2}$ peak at 379.5 eV, a spin-orbit splitting of 10.90 eV with $U4f_{5/2}$, peak, and a clear indication of the satellite peaks from each doublet [142].This findings confirms that the $Ce_{0.10}$ $U_{0.90}$ solid sample contains U(IV) oxide ($UO_2$) and Ce(III) oxide ($Ce_2O_3$) in a 9:1 ratio.

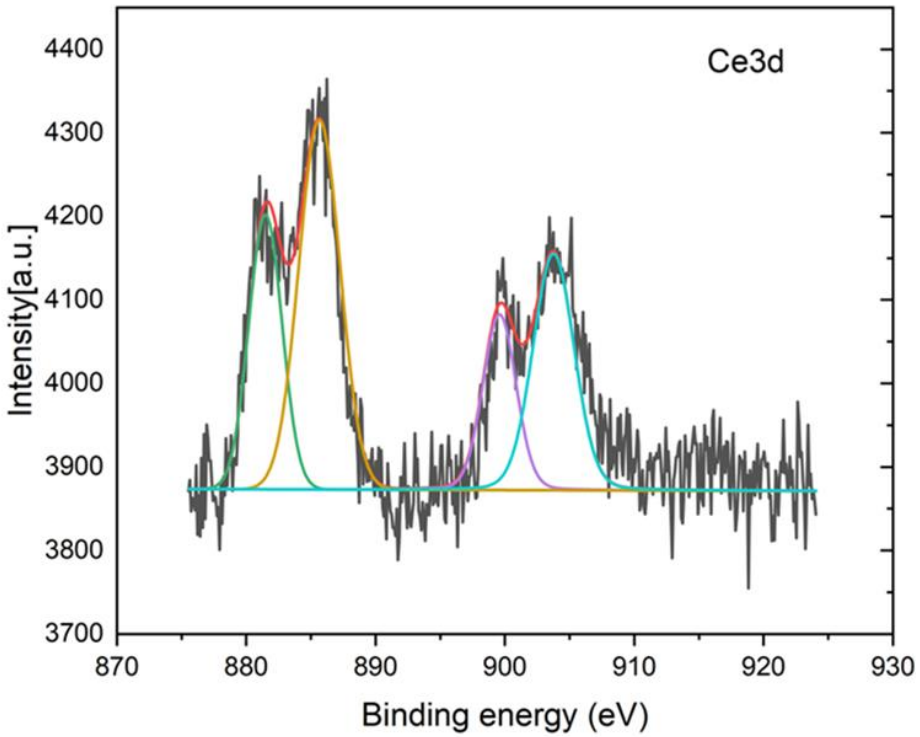


**Figure 17a**. High resolution XPS scans in the Ce3d for the $Ce_{0.10}U_{0.90}$ solid.

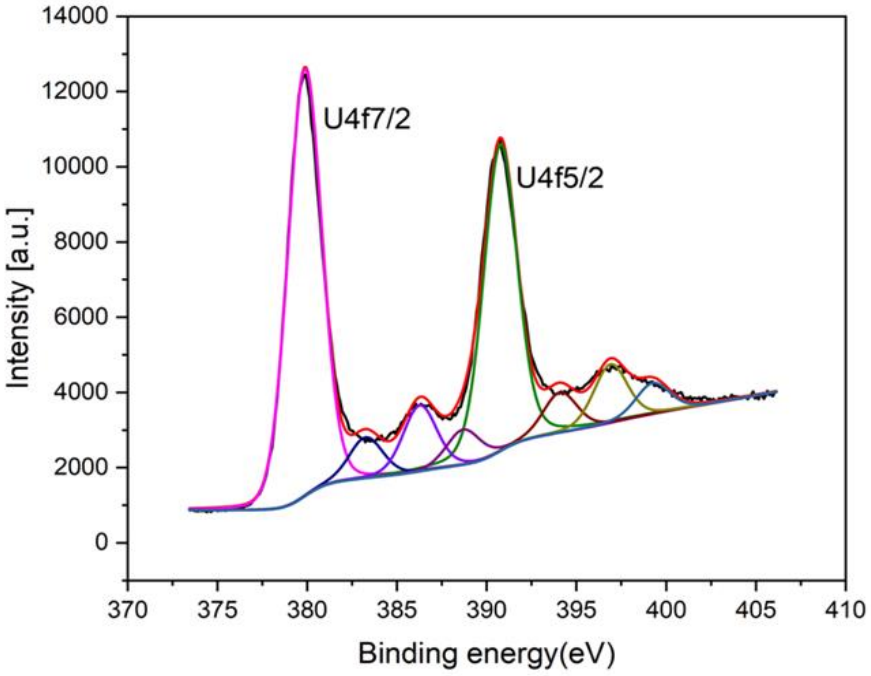


**Figure 17b**. High resolution XPS scans in the U4f region for the $Ce_{0.10}U_{0.90}$ solid.

## 5.3.5. XAS results

The goal of the XAS measurement is to determine the oxidation state and structure around cerium and uranium in solid solutions of mixed oxides formed. The U-Ce solid samples were characterised after equilibration as discussed in the following sections.

### 5.3.5.1 Analysis of XANES data

The background subtracted, normalized and non-normalized X-ray absorption near edge structure (XANES) spectra for the pure reference Ce(III) oxide sample and $U_{0.90}Ce_{0.10}$ solid samples shows that the samples are similar to each other as shown in Figure.18. This similarity indicates that Ce is present as cerium (III) oxidation states in the U-Ce solid samples.

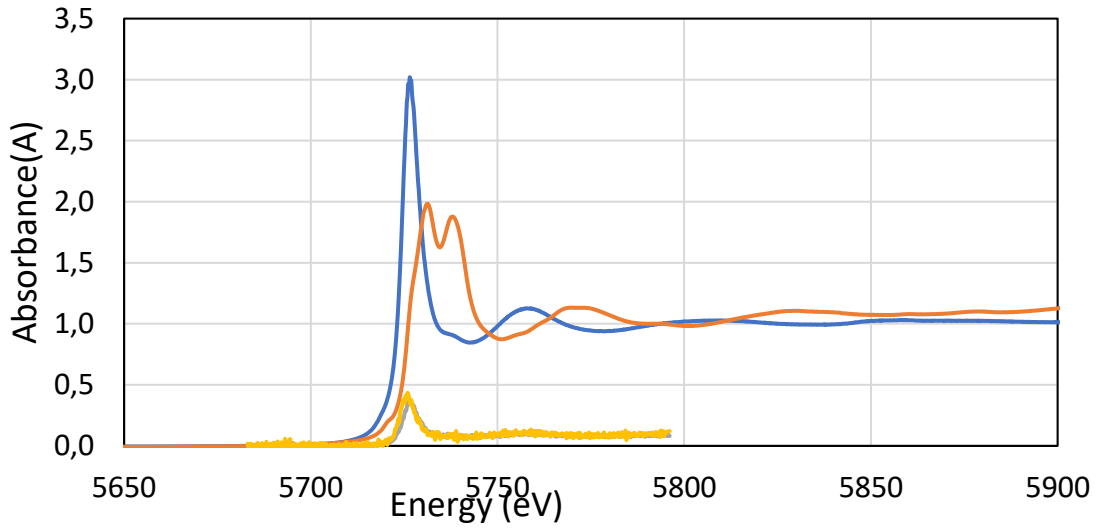


**Figure 18**. Normalized raw XANES spectra of $Ce_2O_3$ (light blue line), and $CeO_2$ (brown line). Raw data, not normalized, of $U_{0.90}Ce_{0.10}$ at two different spots (yellow and grey lines)

A comparison of the XANES spectra of crystalline U(IV) oxide, $UO_2$, collected in 2013, and uranium oxide sample under study is shown in Figure.19. The XANES data acquired on the Balder beamline for the solid samples in this study indicate that uranium exists as U(VI) oxide. The XANES spectra are very different, and in perfect agreement with previous XANES studies of U(IV) and U(VI) oxide (Leinders et al. (2020) [145], Allen et al. (1996) [146]). There is a slight variation in the XANES spectra between pure U(VI) oxide and those containing 1% and 10% Ce(III) oxide, with an increase in white line intensity as the cerium content increases, as shown in Figure.20. Based on the XANES results, it can be concluded that U in the solid samples were not successfully maintained in the tetravalent oxidation state which contradicts the findings from the XPS analysis of the solid samples.

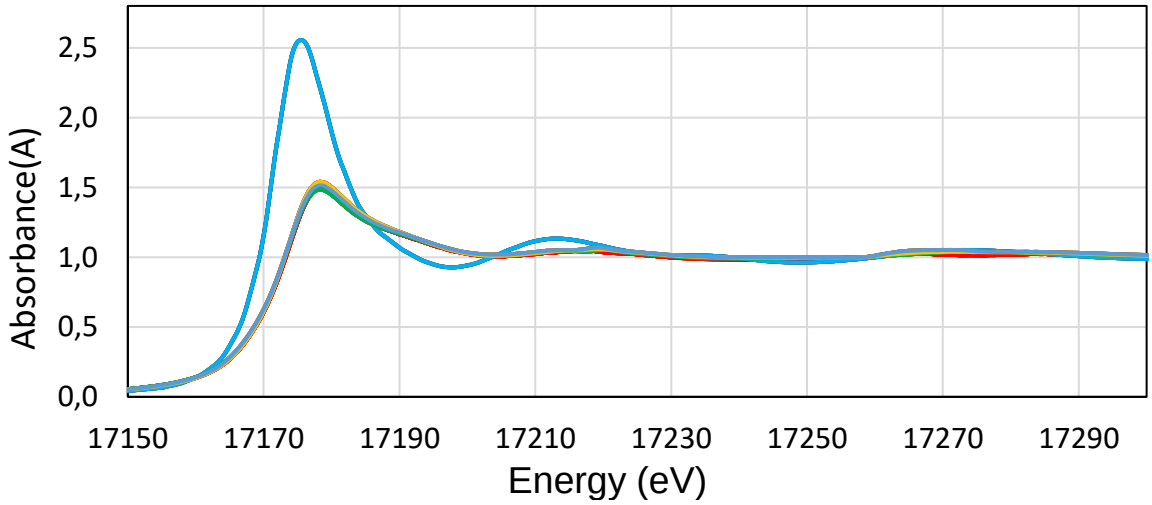


**Figure 19**. Normalized raw XANES spectra of uranium (IV) oxide, $UO_2$ (light blue line), and the studied uranium samples, "sample $UO_2$_pure_1" (red line), "sample $UO_2$_pure_2" (green line), "sample $U_{0.99}Ce_{0.01}$" (purple line) and "sample $U_{0.90}Ce_{0.10}$" (yellow line).

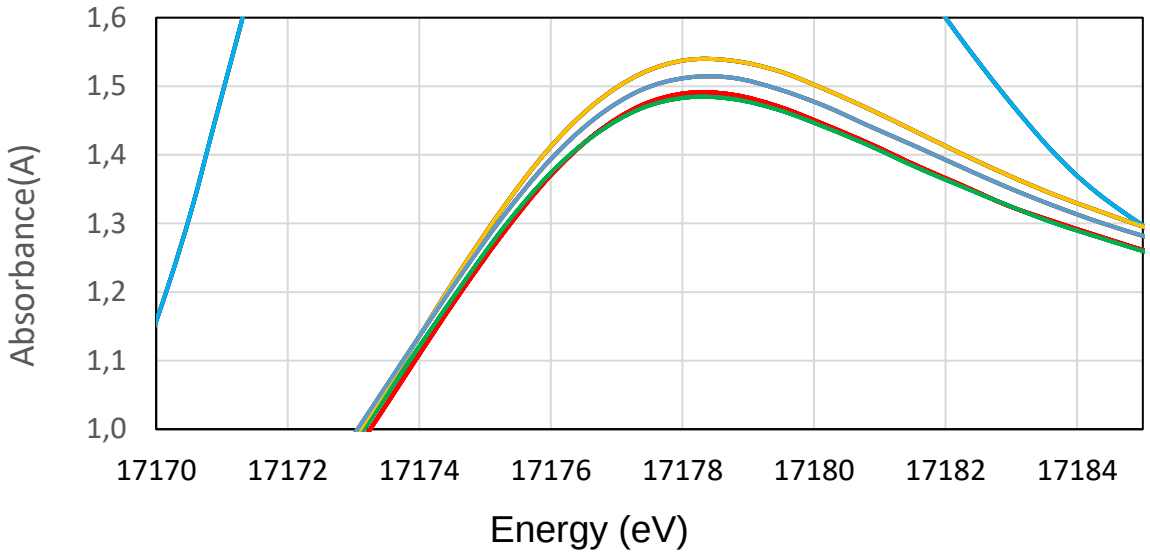


**Figure 20**. Close up of Figure.19 at the white line peak region

## 5.3.5.2.Analysis of EXAFS data

The extended X-ray absorption fine structure( EXAFS) analysis was carried out on the solids to identify any structural changes and to examine the local structure around the U-Ce solid samples. With the information from the XANES region, the EXAFS data were refined. The refined structural parameters are characteristics of uranyl (VI) complexes with two strong U=O bonds at 1.785 Å, and linear multiple scattering within the O=U=O entity. Additionally, there are approximately four U-O bond at 2.32 Å, and four U···U distances at ca. 3.45 and 4.17 Å. For more details, refer to the table in the published article on this study.These distances indicate that the solid sample under investigated consists of gamma-$UO_3$. Additionally, no U-Ce distance was observed in the EXAFS analysis.

To further investigate the findings from the XAS measurement, a certain amount of the solid sample used for XAS analysis were completely dissolved in perchloric acid and analyzed by UV-vis spectroscopy to determine the oxidation state of uranium in the solid samples. The results from the two samples analyzed at the MAX IV laboratory indicate that most of the uranium in the solid sample is as present as U(IV).

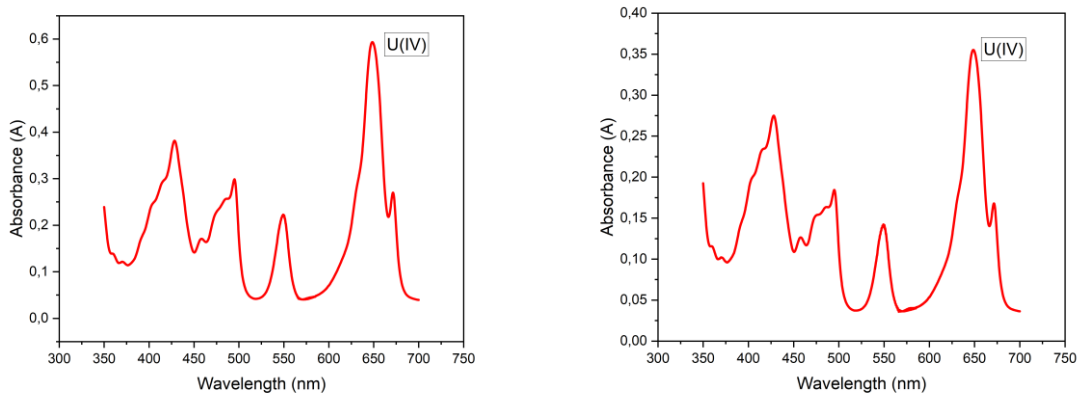


Samples analysed in MAX IV laboratory dissolved in $HClO_4$, left $Ce_{0.01}U_{0.99}$, right $Ce_{0.10}U_{0.90}$.

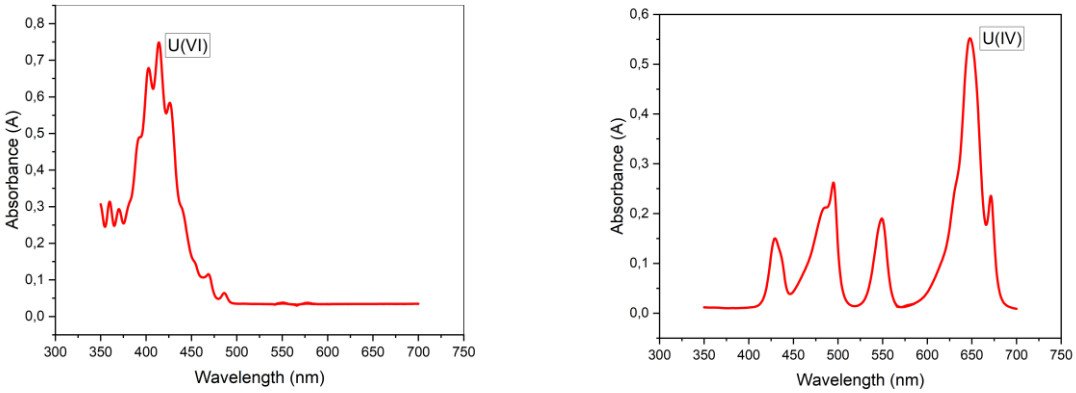


Pure U (VI) in $HClO_4$ Pure U (IV) in $HClO_4$

**Figure 21.** UV-vis analysis of the MAX IV laboratory samples after dissolution in $HClO_4$ compared with spectra of pure U(VI) and U(IV) in the same solvent.

The cause of the oxidation of the MAX IV laboratory samples requires further investigation, however this doesn't affect the conclusion of the present study.

## 5.4. Kinetics of solubility equilibria

As shown in Figure.22, the data for the total concentration of U and Ce in contact with $U_{0.99}Ce_{0.01}O_2$ solids, are quite similar over the equilibration period of 7, 14, 21 and 30 days with only a slight decrease in concentration with time due to the aging of the amorphous solid. This gradual decrease in concentrations is typical behavior of amorphous solids and is expected to become more pronounced with longer equilibration periods.Figure.23 shows the time-dependent changes in U and Ce concentrations in contact with $Ce_{0.10}U_{0.90}$ solid for two selected pH values , indicating that only minor changes occur after the initial 7 days. This behavior is consistent with other tests on amorphous $UO_2$ based co-precipitates. Previous studies by Bruno et al. (1988) [78] reported steady state U concentrations after 50 hours of contact with the solid and Rai et al. (2004) [136] reported that equilibrium in these systems is reached within about 3 days. Therefore, our results along with existing literature data on amorphous $UO_2$ based co-precipitates can be used to conclude that equilibrium was most likely reached in the present study. These equilibrium conditions correspond to equilibrium of both components of the freshly precipitated solids with the solution. At longer equilibration times, the aged coprecipitates are expected to become more crystalline, which will result in lower solubilities.

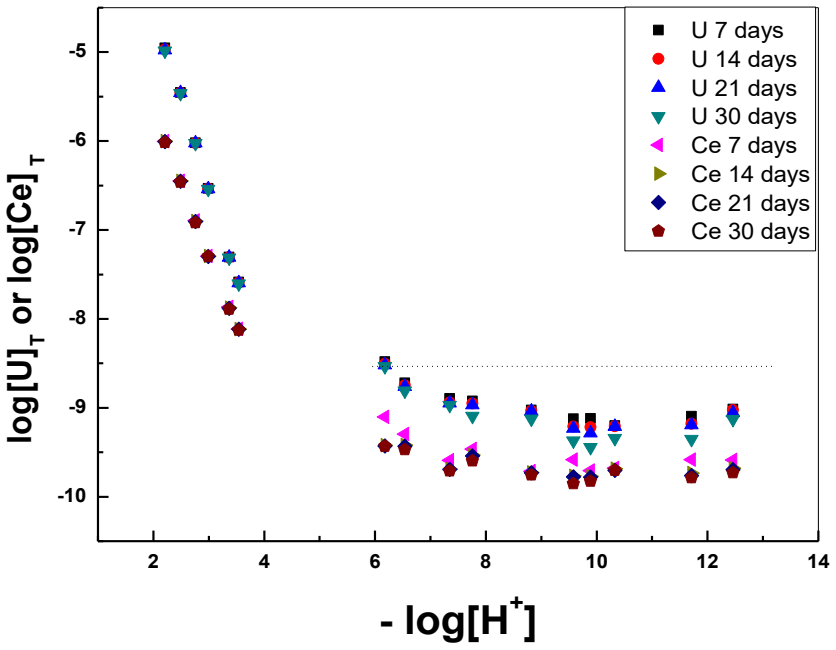


**Figure 22**. Evolution of total concentrations of U and Ce over a 30-day equilibration period across all pH values investigated for the solid containing 1% Ce ( $Ce_{0.01}U_{0.99}$)

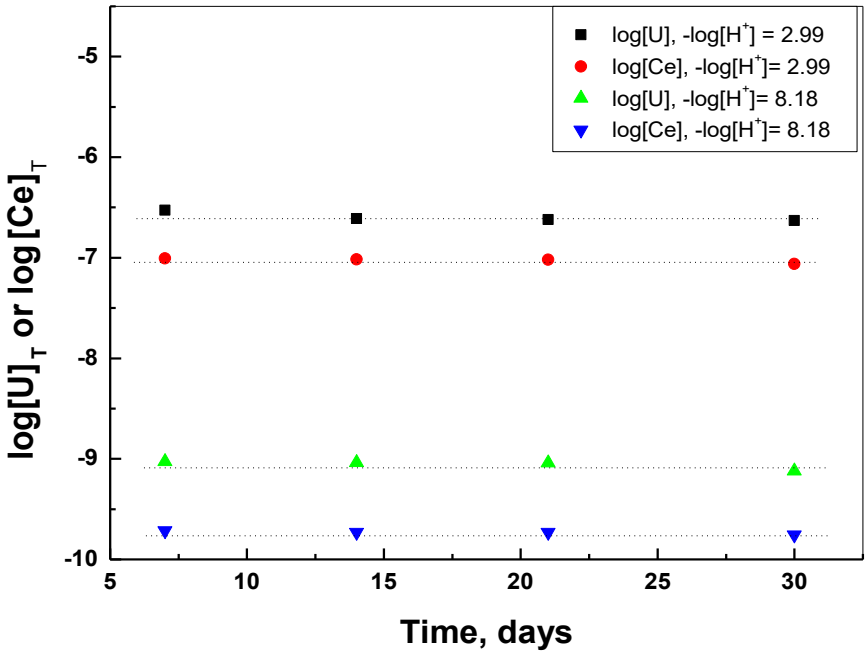


**Figure 23**. Evolution of total concentrations of U and Ce over a 30-day equilibration period for two randomly selected samples at $-\log[H^+]$ values of 2.99 and 8.18 for the solid containing 10% Ce ( $Ce_{0.10}U_{0.90}$ ). The dotted lines are horizontal and centered at the value of the last point.

## 5.5 Results from reduction of Ca- uranyl carbonato complexes by iron study

To facilitate understanding of the results that will be discussed in the following sections below. Table 6 shows the groundwater composition and atmospheric conditions, along with their corresponding experimental labels.

**Table 6.**
Groundwater and Atmosphere compositions and their corresponding sample label.

| Groundwater | Label |
|---|---|
| 01D | A, E, I, M |
| 02A | B, F, J, N |
| 10-2 | C, G, K,O |
| 10-2-Ca | D, H, L, P |
| **Atmosphere** | **Label** |
| 3000 ppm $CO_2$ in Ar | A, B, C, D |
| 400 ppm $CO_2$ in Ar | E, F, G, H, I, J, K, L, M, N, O, P |

### 5.5.1. ICP-MS solution concentration measurements

Figure.24 presents the measured concentrations of dissolved Ca, Fe, and U in the experiment batches A-D conducted under 3000 ppm $CO_2$ in Ar atmosphere. Initially, U concentrations are at 1 ppm ($4.2 \cdot 10^{-6}$ M) but gradually decrease to ~$10^{-9}$ M at the end of the 1200- hour experiment across all datasets. Dissolved Fe concentrations are initially much higher in the A and B tests due to the presence of Fe in the 01D and 02A water compositions. After approximately 200 hours, Fe concentrations are then roughly equal for all the four series. Afterwards, the Fe concentrations stabilizes and reaches an equilibrium of almost $10^{-3}$ M in experiment A and B. In C and D, the concentrations are about two orders of magnitude lower, (~$10^{-5}$ M). During the entire experiment duration, Ca concentrations were stable at their initially set values.

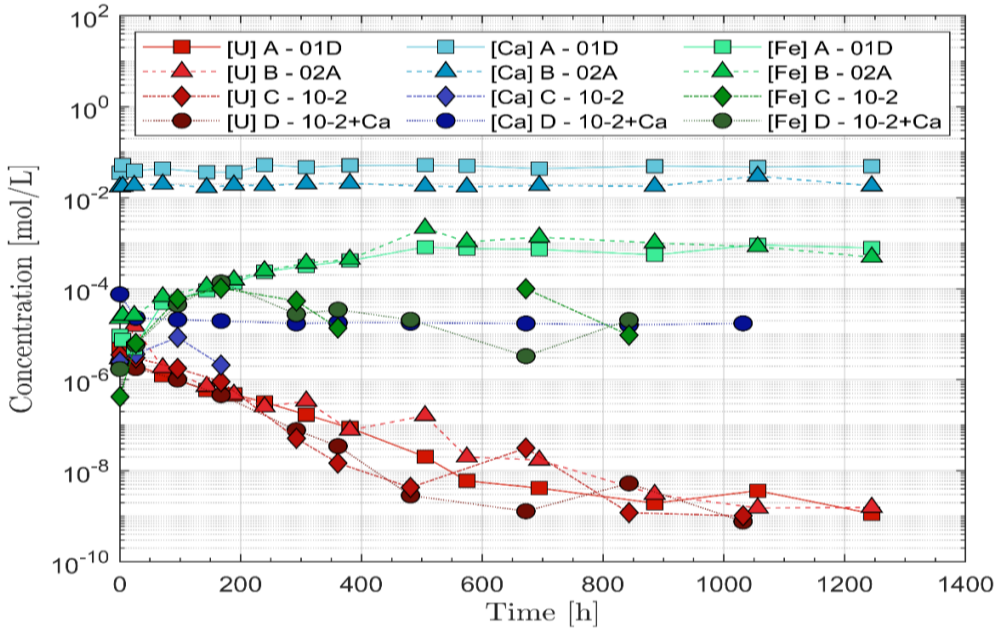


**Figure 24.** Dissolved concentrations in the 3000 ppm $CO_2$ Ar atmosphere experiment batch A-D using the $FeSO_4$ oxygen trap.

In experiment batches I-L carried out under 400 ppm $CO_2$ in an Ar atmosphere. The measured concentrations of dissolved U, Ca, and Fe are presented in Figure.25. In this series, U concentrations are similar (~$10^{-9}$ – $10^{-8}$ M) when compared to the A-D experiment series (~$10^{-9}$ M, as seen in Figure.24). However, the dissolved Fe concentrations in series I & J reached $10^{-4}$ M. The higher levels of ~$10^{-3}$ M Fe concentration observed in experiments A and B were never reached. In this batch, Ca concentrations also remained stable and consistent throughout the experiment.

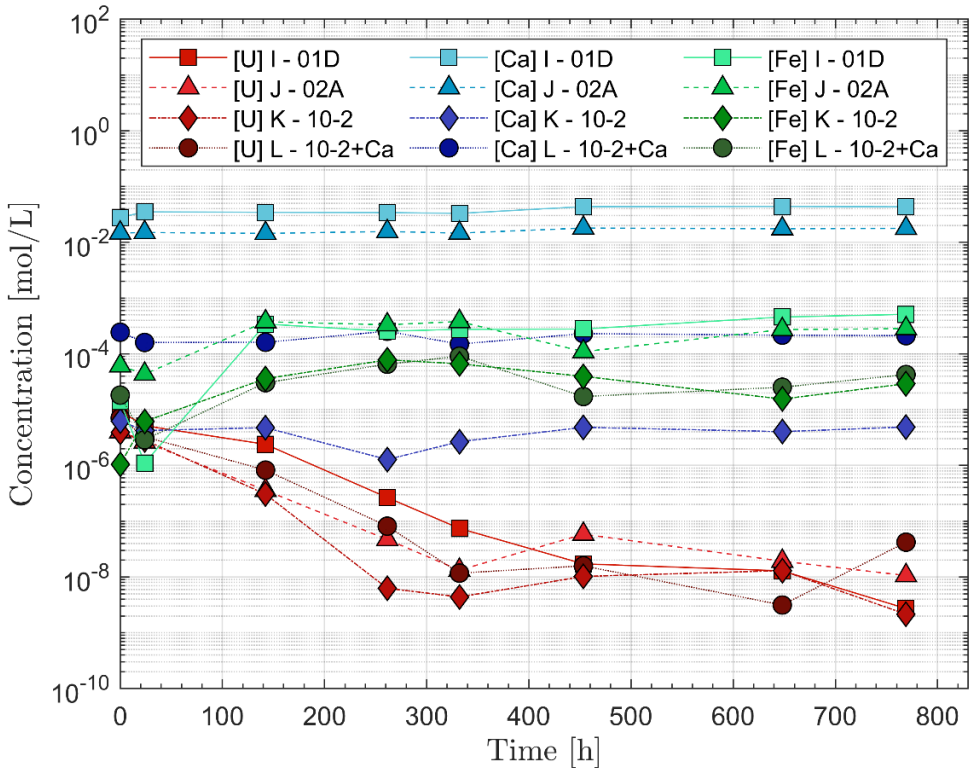


**Figure 25**. Dissolved concentrations in the 400 ppm $CO_2$ Ar atmosphere experiment batch I-L, using the $FeSO_4$ oxygen trap.

The results for the experimental batches E-H and M-P are not presented here due to oxygen contamination during experimental work influencing the obtained results, however more information about the results can be found in the published article.

## 5.6. Solid Characterizations

### 5.6.1. SEM-EDX results

At the conclusion of the leaching experiment, the iron foils were removed from the synthetic groundwater solution. The foils showed dark-green spots (see Figure.26a and b) which indicates a characteristic feature of green rust formation [147,148].

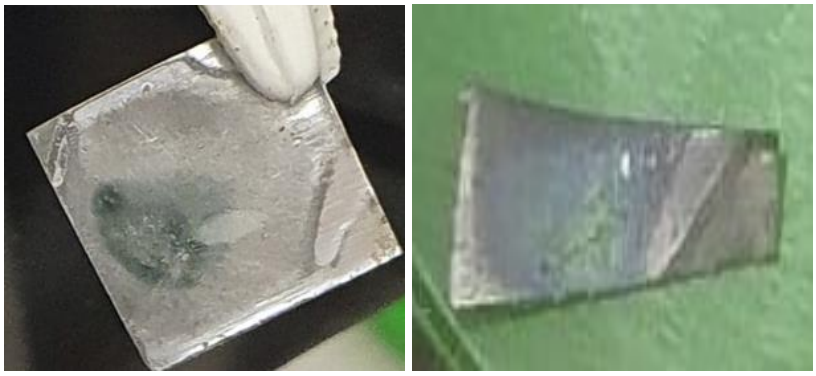

**Figure 26.** Images of iron foil taken after leaching experiments E and F, respectively, where a clear green (a) and a green bluish (b) rust spot is found.

SEM analysis was carried out on iron foils from different experimental batches. However, due to potential oxygen contamination during storage after the leaching experiments, only selected batches were analyzed. SEM images from experiments E, F, K and H a representative of leached iron foils exposed to simulated groundwater compositions are shown in Figure.27 and Figure.28. The uranium is not uniformly distributed across the analyzed area but is rather agglomerated in a few grains like spots in experiment E and F but significantly larger uranium grains were observed on the iron foil from experiment K , with the foils from experiment H very similar to those from experiment E and F. EDX analysis revealed that the iron foils from the experiments using groundwater 01D and 02A displayed complex features with compositions including O,Na, Fe, Cl, C and Si. The uranium-containing grains precipitated on the foils consist of Fe, U, C and O as detailed in Table 7.

The carbonate rich 02A synthesis groundwater resulted in a higher carbon content in the uranium grains on the surface of iron foil F (8– 16 at.%) compared to 01D groundwater use with iron foil E (1–5 at.%) based on ~5 analyzed grains per foil. However, the inclusion of oxygen in the compositional analysis significantly reduced the proportions of other elements.

**E – 01D** **F - 02A**

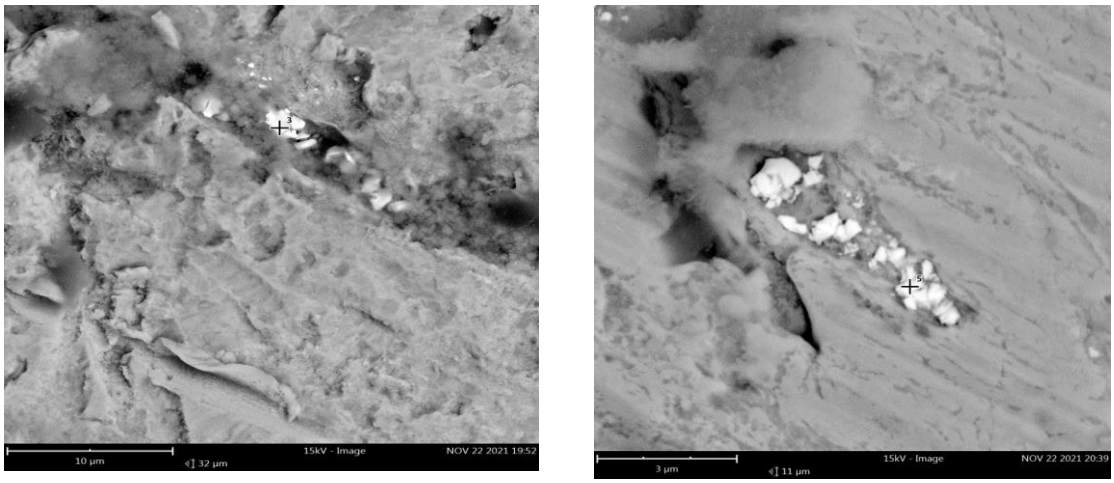


**Figure 27.** SEM analysis on foils from experiments E (a) and F (b) showing rather large, precipitated uranium grains.

**K-10-2** **H-10-2-Ca**

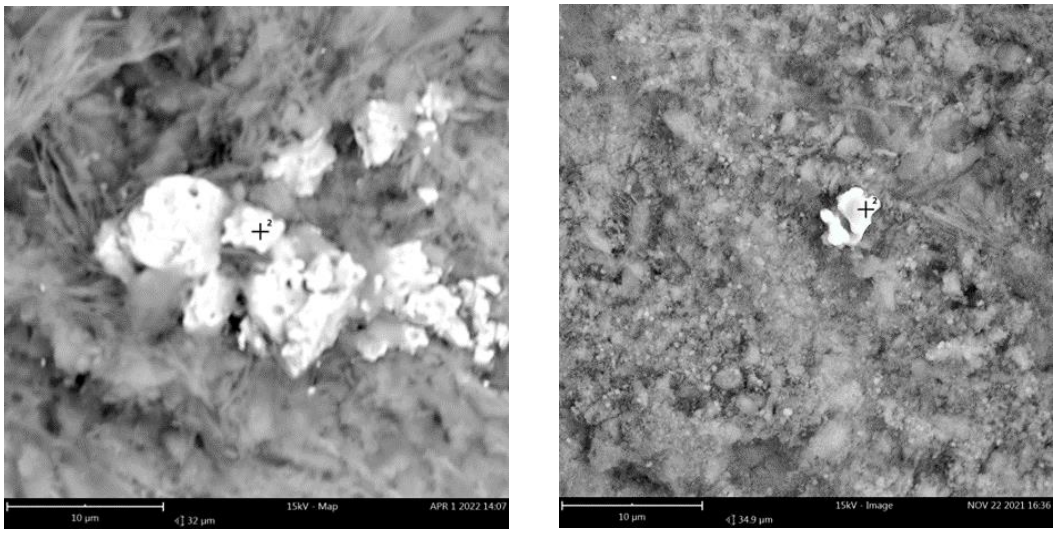


**Figure 28.** SEM analysis on foils from experiments K (a) and H (b) showing the large, precipitated U-containing grains.

**Table 7.**

EDX element compositions on iron foils labelled E, F, G, H,K and L

| Element | E (at.%) | F (at.%) | G (at.%) | H (at.%) | K (at.%) | L (at.%) |
|---|---|---|---|---|---|---|
| O | 57.15 | - | - | 63.06 | 47.58 | 60.72 |
| Fe | 24.61 | 54.22 | 24.26 | 12.42 | 10.61 | 13.40 |
| U | 15.12 | 34.33 | 60.78 | 19.50 | 32.71 | 19.90 |
| C | 3.13 | 11.45 | 14.96 | 5.02 | 9.09 | 5.98 |

A brief elemental mapping of grains deposited on the iron foil surface from experiment F, G and H showed that the uranium precipitates had a considerable overlap with carbon, with carbon rich spots associated with the uranium precipitates. (see Figure.29)

**Carbon G – 10-2** **Uranium G – 10-2** **Carbon H -10-2-Ca** **Uranium H – 10-2-Ca**

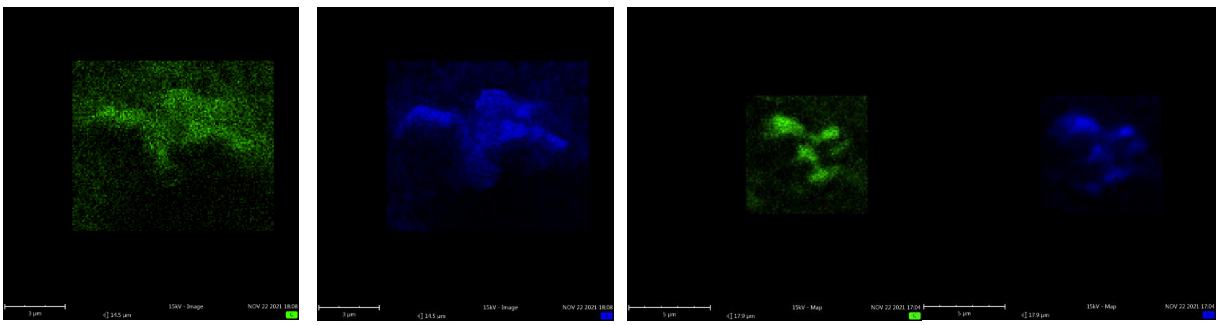

**Figure 29**. The significant overlap between carbon and uranium on the surfaces is shown from the brief elemental mapping scans.

## 5.6.2. XPS Surface analysis results

XPS measurements were carried out on the iron foils containing uranium deposit to assess the surface after exposure to the uranyl-containing synthetic groundwaters. The analysis focuses on the core levels of $U4f_{7/2}$, $U4f_{5/2}$ and $Fe2p_{3/2}$. Due to low amounts of uranium in the experiments, the resulting XPS data indicates low peak intensity and significant noise. The $U4f_{7/2}$ and $U4f_{5/2}$ XPS spectra from experiments E-H are shown in Figure.30 with all peaks having a full width at half maximum (FWHM) close to 1.8 eV, corresponding to a lower oxidation state[149,150].XPS measurement of the $U4f_{7/2}$ & $U4f_{5/2}$ peaks data for other experimental batches can be found in the published work attached to this thesis.

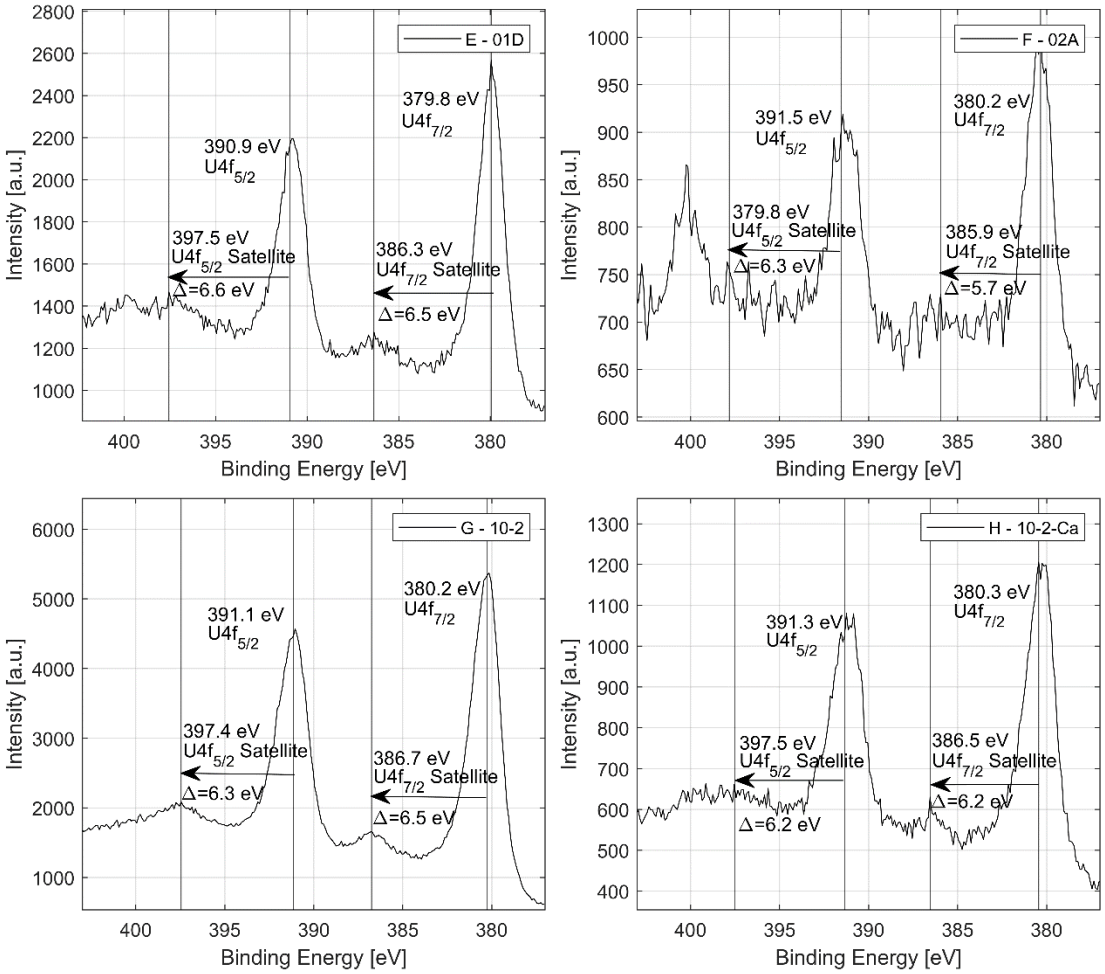


**Figure 30.** XPS measurement of the $U4f_{7/2}$ and $U4f_{5/2}$ peaks with the corresponding satellites from experiment batch E-H.

The $Fe2p_{3/2}$ peaks on the iron foils were analyzed and deconvoluted into their Fe(0), Fe(II)oct, Fe(III)oct, Fe(III)tet, Fe(II)sat and Fe(III)sat signals for the experimental batches E-H and I-L. The corresponding Fe(III)/Fe(II) ratios of the $Fe2p_{3/2}$ peaks are shown in Table 8.

**Table 8.**

Fe(III) to Fe(II) ratios of the Fe2p3/2 peaks of the E-H and I-L experiment batches.

| Iron foil label | Fe(III)/Fe(II) ratio |
|---|---|
| E | 0.9753 |
| F | 1.2251 |
| G | 1.2680 |
| H | 0.9619 |
| I | 0.9987 |
| J | 1.5403 |
| K | 1.2868 |
| L | 1.3389 |

## 5.7. Speciation calculations

The speciation of uranyl after being introduced into the synthetic groundwaters under 400 ppm and 3000 ppm $CO_2$ in Ar atmospheres, was modelled using PHREEQEC [151], with the Lawrence Livermore database, with the addition of calcium uranyl complexes from the NEA TDB database [130] along with the redox -active element RX and Inert elements Ip and Im [152]. The $Ca_2UO_2(CO_3)_3$ complex dominates in Ca containing groundwaters under the 300 ppm $CO_2$ partial pressure. As shown in Table 9, calcium-uranyl-carbonato complexes account for about 90% of the dissolved U in groundwater 01D with 400 ppm $CO_2$ and 56.5 % in the 3000ppm $CO_2$. In the synthetic groundwater 02A, these complexes play an even more dominant role in uranyl speciation, making up ~99.7% of the total U in both 400 and 3000 ppm $CO_2$ .

**Table 9.**

Modelled major uranyl species using PHREEQE C in the 400 ppm and 3000 ppm $CO_2$ atmosphere experiments.

| **400 ppm $CO_2$** | **01D** | **02A** | **10-2** | **10-2-Ca** |
|---|---|---|---|---|
| $Ca_2UO_2(CO_3)_3$ | 87.60% | 95.39% | 0.00% | 48.08% |
| $CaUO_2(CO_3)_3^{2-}$ | 1.88% | 4.28% | 0.00% | 43.43% |
| $UO_2(OH)_2$ | 5.75% | 0.00% | 3.56% | 0.31% |
| $UO_2(CO_3)_2^{2-}$ | 2.17% | 0.01% | 68.09% | 5.88% |
| $UO_2CO_3$ | 2.09% | - | 1.09% | 0.09% |
| $UO_2(CO_3)_3^{4-}$ | - | 0.31% | 24.51% | 2.21% |

| **3000 ppm $CO_2$** | **01D** | **02A** | **10-2** | **10-2-Ca** |
|---|---|---|---|---|
| $Ca_2UO_2(CO_3)_3$ | 55.34% | 95.39% | - | 32.06% |
| $CaUO_2(CO_3)_3^{2-}$ | 1.19% | 4.27% | - | 28.75% |
| $UO_2CO_3$ | 17.06% | - | 9.85% | 3.90% |
| $UO_2(OH)_2$ | 7.18% | 0.00% | 4.09% | 1.64% |
| $UO_2(CO_3)_2^{2-}$ | 4.94% | 0.02% | 78.83% | 31.56% |
| $(UO_2)_2CO_3(OH)_3^-$ | 1.75% | - | 3.43% | 0.56% |

## 5.8. Kinetics of U(VI) reduction

The kinetics of U(VI) removal by corroding metallic iron were investigated by measuring the uranium concentration in solution in all the experimental batches at various times (shown in Figure.24 and 25). Under the experimental conditions in this study, the reductive sites on the iron surface and Fe(II) in solution are significantly greater than U(VI). The uranium removal process exhibits characteristics of pseudo-first order reaction kinetics as evidenced by the nearly linear relationship observed when plotting ln ($C_t/C_0$) against reaction time, where $C_t$ and $C_0$ represents the U(VI) concentrations at time t and 0 respectively.

The natural logarithm of uranium concentration during the early stages of each experiment, specifically the first 5-6 data points was analysed using linear least square fitting. The slope of this fitted line, presented in Table 10 represents the pseudo- first order rate constant for U(VI) reduction. Experiments A and B, which had higher iron concentrations, do not show faster reduction kinetics. This observations suggests that the increased iron concentrations did not influence the kinetics but rather altered the final equilibrium conditions. Higher $CO_2$ pressure would result in greater dissolution of Fe at equilibrium, which may not impact the kinetics in the initial phase of the experiment.

**Table 9.**

Pseudo first order rate constants

| Atmosphere | Experiment | Pseudo first order rate constant, $d^{-1}$ |
|---|---|---|
| 3000 ppm $CO_2$ | A - 01D | 8.4E-3 |
| | B - 02A | 8.4E-3 |
| | C - 10-2 | 1.5E-2 |
| | D - 10-2+Ca | 1.2E-2 |
| 400 ppm $CO_2$ | I - 01D | 1.4E-2 |
| | J - 02A | 1.8E-2 |
| | K - 10-2 | 2.2E-2 |
| | L - 10-2+Ca | 4.3E-3 |
| 400 ppm $CO_2$ | M - 01D | 5.1E-3 |
| | N - 02A | 3.0E-3 |
| | O - 10-2 | 5.6E-2 |
| | P - 10-2+Ca | 1.5E-2 |

# 6.0. Discussion of results

## 6.1. Discussion on coprecipitation of Ce(III) oxide with $UO_2$

The aqueous concentrations of U in equilibrium with the coprecipitates solids containing 1% and 10% mole fraction of Ce ($Ce_{0.01}U_{0.99,}$ $Ce_{0.10}U_{0.90}$) are in excellent agreement with existing solubility data for $UO_2$(am) indicating that reducing conditions were successfully maintained during the experiments. In previous studies, Bruno and Sandino [77,78] investigated $UO_2$(am) coprecipitation with La, Ba, Th. The measured concentrations of U at pH 4.5 were higher than $10^{-4}$ M while in the study of Rousseau et al.(2002) [80], the observed U concentrations were slightly below $10^{-7}$ M for pH values greater than 4. Notably, no holding reductant was used in these previous studies and while Rousseau et al. (2002) used electrochemical reduction , it created highly reducing conditions only at the electrode surface, without ensuring consistent reduction throughout the bulk solution. In comparison, the present study use of a holding reductant contributed to the successful maintenance of reducing conditions in the bulk solution. This methodological difference may explain why our results differ from those observed in the previous studies where reducing conditions were less uniformly controlled. The ability to maintain stable reducing conditions across the entire system is crucial for accurately assessing the solubility and behavior of U in the presence of various coprecipitating elements, such as Ce.

The observed equilibrium concentrations of Ce in the solution are significantly lower than the solubility of pure $Ce(OH)_3$(s) as reported in the study by Kragten et al.(1978) [112].This suggests that Ce concentrations are primarily controlled by co-precipitation. Furthermore, the measured aqueous Ce concentrations in equilibrium with the coprecipitates clearly indicate that the co-precipitates do not behave as homogeneous ideal solid solutions unlike.in the case of $(U,Np)O_2$ solid solutions studied by Rai et al. (2004) [136].In a homogenous ideal solid solution, the activity of Ce in the solid would be expected to be equal to its mole fraction. The concentrations of the minor component Ce(III) were totally controlled by the release of U, and they were lower than the U concentration for both $Ce_{0.01}U_{0.99}$ solid and $Ce_{0.1}U_{0.9}$ solid. In the similar study of Sass and Rai 1986 [153] of the Cr(III)-Fe(III) hydroxide precipitates, the concentration of Cr(III) is lower than that of Fe(III) for the 1% Cr solid, but for the 9% Cr solid, the concentrations of Cr(III) at equilibrium are higher than those of Fe(III).

The kinetics of the equilibration of the precipitates occurred relatively fast and equilibrium was attained in all the solubility measurements. Therefore, our data alongside similar previous studies strongly suggest that equilibrium was most certainly reached in the present study. The solid characterization results indicate that no phase changes occurred during the equilibration period. The chemical composition of the solids remained consistent within experimental error before and after equilibration with no significant changes in the overall chemical composition of the solids over time. The SEM analysis of the solids shows a uniform appearance ,with SEM-EDX mapping of U and Ce indicating a homogeneous distribution of the components in the solid.

The XRD diffractogram reveal that the solids are amorphous with similar patterns observed before and after equilibration, suggesting that the solubility- controlling solids are likely amorphous in nature. XRD analysis of the solid sample heated to 900 ˚C under a reducing atmosphere shows a shrinkage in the $UO_2$ lattice parameter which is proportional to the Ce(III) content in the solid solution. The lattice parameter change agrees well with predictions from

published relationships for Ce(III) content in stoichiometric U-Ce solids. However, Vegard's law, which states that the cell parameter of a solid solution varies linearly with composition between the two end members, cannot be applied directly to these solids due to the hexagonal structure of $Ce_2O_3$(s) end member.

Both before and after equilibration, the XPS analysis confirmed the oxidation state of Ce(III) in the $Ce_{0.10}U_{0.90}$solid, as well as a ratio U:Ce of 9:1 while in the $Ce_{0.01}U_{0.99}$ solid Ce was under the detection limit. U(IV) oxidation state was confirmed by XPS for all solids, both before and after equilibration. XAS analysis results shows that Ce is present as Ce(III) in the solid samples, while U is identified as U(VI) in the form of $UO_3$(s) in the solid samples. The results for the U were quite surprising as they contradict the solubility results, which show a completely reduced $UO_2$(s) phase and the XPS results which also indicate a fully reduced surface. Further investigation of the same solid stored in the glove box after dissolving it in $HClO_4$ showed presence of mainly U(IV). This discrepancy suggests that the XANES samples may have been oxidized during transport or at the beam line. Our samples are extremely fine grained, and unlike the XPS samples, were not transported in an inert atmosphere vessel.

The only potential oxidant during transport, atmospheric oxygen, could oxidize both U(IV) to U(VI) and Ce(III) to Ce(IV) while the XAS analysis indicates reduced Ce(III) and oxidized U(VI). Further, the oxidation of $UO_2$(s) by atmospheric oxygen at room temperature is a relatively slow process and $UO_{2+x}$ phases are usually formed. To our knowledge, there are no other reports of the oxidation of pure $UO_2$(s) samples by the XAS beam and nor are there known XAS-EXAFS studies of cerium doped $UO_2$ that might offer further insight.

## 6.2. Discussion on reduction of Ca- uranyl carbonato complexes by iron

In groundwater solutions containing corroding iron foil, the reductive precipitation of U(VI) is highly effective, as evidenced by the rapid decrease in dissolved uranium concentrations. The increase in the $HCO_3^-$ concentration is due to the elevated dissolved $CO_2$ concentration resulting from the higher $CO_2$ partial pressure (3000 ppm in $CO_2$ in Ar). The observed lower uranium concentrations and higher iron concentrations in batches I-L suggest that the $FeSO_4$ oxygen trap is more efficient compared to the $FeCO_3$ trap, due to the higher solubility of $FeSO_4$ [154] and consequently higher Fe(II) concentration in the oxygen trap solution. This increased efficiency aids in efficient removal of the $O_2$ impurities from the glovebox atmosphere and eliminating $O_2$ contaminants from the Ar + $CO_2$ gas mixture. Table 10 shows that the presence of calcium-uranyl-carbonato complexes slightly reduces the rate of U(VI) reduction in calcium containing groundwater compared to the calcium free 10-2 solution.

At 3000 ppm $CO_2$, the reduction rate constant is ~ 1.8 times higher in the 10-2 solution compared to the Ca-containing groundwaters, where calcium-uranyl-carbonato complexes dominate. However, these differences are minor and less significant than the efficient removal of oxygen traces, which led to the highest reduction rates in the 400 ppm $CO_2$ experiment( I,J,K) with calcium presence slightly slowing the reduction by 1.2-1.6 times The presence of metallic iron in solution along with the anoxic corrosion products such as magnetite or carbonate green rust on its surface is expected to enhance even reduction caused by Fe(II) sorbed from solution onto their surface [155]. Uranium can also be reduced directly on magnetite [156], or alternatively on carbonate green rust [75,158]. However, the $Fe2p_{3/2}$ peak deconvolution analysis gives a ratio between Fe(III) and Fe(II) close to 1 for all foils in experiment batches E-H and I-L, indicating an oxide with a higher amount of Fe(II) than what

is present in magnetite. Simultaneously, this ratio is lower than the amount of Fe(II) expected from most green rust compositions [159], suggesting a possible mixture of the two different oxides.

Solid characterization of the corroded iron foils through SEM analysis shows that uranium precipitated on carbonate rich spots on the iron foil surfaces, possibly associated with the carbonate green rust corrosion product. This results corresponds well with the work of Cui and Spahiu, (2002) [75] where uranium precipitation occurred on top of green rust under similar experimental conditions as well as with O'Loughlin´s results [158] which showed that $UO_2$ nanoparticles were formed due to the reductive action of green rust. The XPS measurement of the $U4f_{7/2}$ peaks in experiments E-H have energies very similar to that of U(IV) at 380.0±0.2 indicating that the uranium on the iron foils is in the reduced U(IV) state.

# 7.0 Conclusions

In this work a study of the solubility behaviour of the minor components of the nuclear waste matrix in relation to the major component $UO_2$ have been investigated. This study relates to the possible coprecipitation behaviour of the $UO_2$ matrix in connection with a near field situation under repository conditions where uranium can be a major component in case of oxidative dissolution of the fuel caused by the breached of the canister material in contact with ground waters.

For this purpose, neutralization of acidic solutions containing U(IV) and Ce(III) at room temperature in glove box atmosphere and in the presence of sodium dithionite results in coprecipitation of these elements as amorphous solid solutions $Ce_xU_{1-x}O_{2\pm y.}$ The solubilities of the precipitates with different mole fractions (x) of $Ce(OH)_3$ (x = 0.01 or 0.1) were investigated in 1 M $NaClO_4$ solutions containing sodium dithionite between pH 2.2 and 12.8 8 in undersaturation tests under reducing conditions. The experiments, which spanned up to one month, indicate that equilibrium was achieved relatively fast (less than 1 week as shown in Figure.22 and 23).

The solubility of these coprecipitates were measured in the studied pH range in 1 M $NaClO_4$ solutions. The measured U concentrations were in excellent agreement with the lower limit of the $UO_2$(am) solubilities selected by NEA-TDB (Grenthe et al. 2020), as expected for coprecipitates with relatively very low Ce content (1% Ce), these results highlight the success in maintaining U reduced in its tetravalent state during the experimental work. The Ce concentrations were completely dominated by the release of U.

Ce concentrations were consistently lower than U across the pH range and increased slightly with higher Ce content in the solids, indicating that $Ce_xU_{1-x}O_{2\pm y}$ solids behave thermodynamically as solid solutions. The conditional solubility product of $Ce(OH)_3$ from the coprecipitate was several orders of magnitude (~ 4 in the near neutral pH range and ~18 in the acidic range) lower than that of pure $Ce(OH)_3$(s). The activity coefficients of $Ce(OH)_3$(s) in the coprecipitate are much less than 1 indicating that the mixing of $Ce(OH)_3$ with $UO_2$ is highly favourable.

Several analytical methods were used to characterize the solids (chemical analysis, SEM-EDX, XPS, XAS and EXAFS) confirming homogeneous distribution of Ce in the $UO_2$ matrix. The XRD results indicate that the solubility controlling solids are amorphous. The XAS-EXAFS results were the only ones which showed that the samples were completely oxidized to $UO_3$(s), apparently by atmospheric oxygen during transport to MAX IV laboratory or by the beam, while Ce was in reduced form as Ce(III). The incorporation of Ce in the $UO_2$ solid caused a lattice parameter shrinkage proportional to the Ce content.

These results indicates that the formation of a solid solution can significantly affect the solubility of the minor component and the coprecipitation of the minor components from a $UO_2$ solid solution is kinetically and thermodynamically controlled by the behaviour of the major component $UO_2$. Furthermore, these results also highlight that the concentrations of Ce, other lanthanides or actinides and fission products released by the fuel matrix during oxidative dissolution will not be determined by their individual solubilities when they coprecipitate with $UO_2$(s) at the iron surface of the canister insert but will be orders of magnitude lower. It can also be concluded that the solubility of the minor components cannot be only predicted on the

basis of their individual solid phases but rather also on their coprecipitation behaviour (formation of solid solutions) with other radionuclides present in the spent fuel matrix.

The major goal of this study was to refine the techniques and procedures for maintaining appropriate reducing conditions in order to obtain reliable solubility data. This experience will be very valuable when the study of coprecipitation of $UO_2$ with other actinides is carried out.

In the study on the reduction of Ca uranyl complexes in the presence of iron the experimental results indicate that the metallic iron in the fuel canister inserts provides an additional reducing capacity within the system. This was demonstrated by the significant reducing effect of the iron foils, which decreased the initial U concentration from ~ $4.2 \cdot 10^{-6}$ M to approximately three orders of magnitude lower concentrations ($10^{-9}$ M) in all groundwater compositions which is quite similar to the equilibrium lower solubility of $UO_2$(am) [157].

The characterizations of the iron foil with both SEM-EDX and XPS after test conclusion confirmed uranium precipitation as $UO_2$(s) on top of the iron foil surfaces, forming radially growing particles. Despite the low total concentration of U in solution, these particles exhibited relatively large radii. The precipitation likely occurred on carbonate green rust, which formed on corroding iron surface and appeared as dark green spots (see Figure.26 a and b).

The presence of calcium-uranyl-carbonato species did not inhibit the reductive precipitation in contact with a corroding metallic iron surface, although the reduction was slightly slower in the presence of Ca. These findings suggest that in the event of a canister breach in a repository potentially dissolved $UO_2$ in the U(VI) oxidation state would then be expected to be reduced and probably re-deposited as $UO_2$ particles on the corroding iron surface of the canister insert. The understanding of $UO_2$ migration behavior in groundwater solution in the presence of iron is crucial for assessing the safety of geological repositories as well as for predicting the behavior of dissolved uranium in the environment.

# Future work

Using the experience from the preliminary study of the coprecipitation of Ce(III) oxide with $UO_2$, the study of the co-precipitation of $UO_2$ with reduced state of Pu under reducing conditions will be carried out. The major difficulty will be to create the appropriate redox condition in the laboratory. When the co-precipitation of $UO_2$ with Pu(III) or Pu(IV) is investigated, the co-precipitation of the three actinides oxides of U, Pu and Np will be attempted. In this case the composition of the solid prepared will be similar to the composition of U, Pu and Np in the spent nuclear fuel.

In other planned studies, leaching experiment will be carried out to investigate the effect of metallic iron on un-irradiated MOX fuel. The work with the unirradiated MOX with Pu contents of approximately 10 % will be carried in an autoclave under Ar atmosphere. The test would begin with contacting iron foils (to be used later also in experiments with active material) with synthetic Forsmark groundwater. Based on the results of the initial iron corrosion study, it will already be clear what maximal Fe(II) concentrations can be reached in the autoclave and under what conditions. Given the high alpha dose rate of the 10% Pu doped pellet, its dissolution is worthwhile to study.

Finally, the study of dissolution of unirradiated MOX fuel with similar Pu content in the presence of iron corrosion product such as siderite, chukanovite and ankerite (and possibly magnetite) will be carried out in an autoclave using the synthetic Forsmark groundwater composition.

# Acknowledgments

Reaching this milestone has been a significant journey, and I am deeply grateful to everyone who has contributed and supported me along the way.

First and foremost, I would like to express my profound gratitude to my supervisor Prof. Christian Ekberg for your leadership, unwavering guidance, invaluable insights and support. Your mentorship has been instrumental in shaping my research.

I also extend my sincere appreciation to my co-supervisor, Prof. Kastriot Spahiu, whose expertise and advice have been crucial to my work. Your support has been indispensable, and I am deeply appreciative of the time and effort you have dedicated to my research and development, helping me navigate the challenges of this journey.

A special appreciation to my examiner, Prof. Teodora Retegan Vollmer, for your tutelage, thoughtful feedback and constant encouragement which have been invaluable in refining my work.

I would like to acknowledge the Division of Nuclear Chemistry and Industrial Material recycling for providing a stimulating academic environment and the resources necessary for my research. The group's commitment to excellence and quality research has been a continuous source of inspiration and admiration.

I am also deeply grateful to the seniors in our research group, whose experience and advice have been a guiding light. Your willingness to share your knowledge and support younger members of the group is commendable.

To my colleagues and fellow researchers, thank you for the camaraderie, the many insightful discussions, and for making this journey a collaborative experience. Your friendship and support have made this experience more enjoyable and fulfilling.

My sincere gratitude also goes to Dr. Stellan Holgersson, Dr. Stefan Allard and Dr. Marcus Hedberg for ensuring that all the necessary resources were always available and for maintaining an efficient, organized and safe lab environment. Your dedication to your work has made a considerable difference in the smooth progress of my research, which has impacted my work significantly.

I would also like to thank our administrator, Sandra Nayeri, for her support, kindness and for ensuring that administrative processes ran smoothly.

My heartfelt appreciation goes to my family, my beloved wife and son for their endless love, unwavering support, and encouragement. Your belief in me has been my greatest source of strength and motivation throughout this journey.

This thesis is as much a result of your support as it is of my work. Thank you all for being part of this journey with me.

Lastly, the Swedish Nuclear and Fuel and Waste Management Company (SKB) is greatly acknowledged for funding this research project (I.D:21235062) extending my gratitude to Prof. Lena Zetterström Evins.

Mustapha .G.Saleh

October 2024, Gothenburg

# References

[1] International Energy Agency (IEA), Electricity Report (2024). Analysis and forecast to 2026.

[2]IEA, Electricity Market report (2023). https://iea.blob.core.windows.net/assets/255e9cba-da84-4681-8c1f-458ca1a3d9ca/ElectricityMarketReport2023.pdf

[3] https://www.iaea.org/events/nuclear-energy-summit-2024.

[4] Kim,Y.,Kim,W.,Kim,M.(2014) .An international comparative analysis of public acceptance of nuclear energy. Energy policy 66 pp. 475-483.

[5] Marcus, G.H (2019).Nuclear power around the world, Nature Reviews Physics,1 172.

[6] https://www.nuclear-power.com/nuclear-power-plant/radioactive-waste/high-level-waste-hlw/

[7] IAEA, Nuclear power reactors in the world technical report reference data series No.2, International atomic agency edition https://www-pub.iaea.org/MTCD/Publications/PDF/RDS-2-43_web.pdf

[8]Aaltonen,I.,Engström,J.,Gehör,S.,Kosunen,P.,Kärki,A.,Paananen,M.,Paulamäki,S., Mattila, J.A. (2016). Geology of Olkiluoto, Posiva report,2016-16.

[9] Svensk Kärnbränslehantering AB. (2011). Technical report TR-11-01 Volume 1 – Long term safety for the final repository for spent nuclear fuel at Forsmark.

[10] Ewing, R.C., Weber, W.J., Clinard,F.W. (1995).Radiation effects in nuclear waste forms for high level waste radioactive waste, progress in nuclear energy, 29 pp.63-127.

[11]Grenthe,I.,Drożdżyński,J.,Fujino,T.,Buck,E.C.,AlbrechtSchmitt,T.E.,Wolf,S.F.(2008). Uranium, in: The chemistry of the actinides and the transactinide elements, springer, pp.253-698. 4th Edition.

[12] Hazen, R.M.,Ewing,R.C.,Sverjensky,D.A.(2009).Evolution of uranium and thorium minerals, Am. Mineral., 94,pp.1293-1311.

[13] Hammond, C. (2000).The elements, Handbook of chemistry and physics, 81

[14] Yanga,W., Parker, T.G, Suna, Z.M. (2015). Structural chemistry of uranium phosphonates., Coordination chemistry reviews 303.pp. 86–109.

[15] Holden, N. (1977). Isotopic composition of the elements and their variation in nature: a preliminary report, in, Brookhaven National Lab.

[16]Georgiou,E.,Raptopoulos,G.,Anastopoulos,I.,Giannakoudakis,D.A.,Arkas,M.,Paraskevopoulou, P., Pashalidis, I. (2023).Uranium Removal from Aqueous Solutions by Aerogel-Based Adsorbents—A Critical Review. Nanomaterials 2023, 13, 363.

[17] Kutty,T., Hegde,P., Khan,K., Basak,U., Pillai,S., Sengupta,A., Jain,G., Majumdar,S.H., Kamath,H.,Purushotham,D.(2002).Densification behaviour of $UO_2$ in six different atmospheres, J. Nucl.Mater.,305.pp. 159-168.

[18] Olander, D.R (1981). The theory of uranium enrichment by the gas centrifuge. Prog. Nucl. Energy , 8, 1–33.

[19] Krass, A.S. (1983).Uranium Enrichment and Nuclear Weapon Proliferation; Oxford University Press: Oxford, UK.

[20] Choppin, G., Liljenzin, J.O., Rydberg, J., Ekberg, C. (2013). Chapter 21- The Nuclear Cycle, in: Radiochemistry and Nuclear Chemistry 4th Edition, Academic Press, Oxford, (2013) ,pp. 685-751.

[21] Jevremovic,T. (2009) Nuclear Principles in Engineering 2nd edition; Nuclear Reactor Control pp. 491-516 Springer.com.

[22] Bruno, J., Ewing,R.C. (2006). Spent nuclear fuel. Elements, Volume 2. pp.343-349.

[23] Cui,D., Lowa,J., Spahiu, K. (2011). Environmental behaviors of spent nuclear fuel and canister materials. Energy Environ.Sci., 4, pp.2537-2545.

[ 24]Ewing,R.C., Runde,W., Albrecht-Schmitt,T.E.(2010).Environmental impact of the nuclear fuel cycle: Fate of actinides MRS bulletin volume 35.

[25]Johnson,L.H.,Shoesmith,D.W.(1988).Spent Fuel.In: Lutze W, Ewing RC (eds) Radioactive Waste Forms for the Future. North-Holland, Amsterdam, pp. 635-698.

[26] Oversby,V.M.(1994).Nuclear Waste Materials. In: Cahn RW, Haasen P, Kramer EJ (eds) Materials Science and Technology, Chapter 12 from volume 10B, VCH Verlagsgessellschaft mbH, pp. 391-442.

[27] Hedin, A. (1997). spent nuclear fuel- How Dangerous is it? Technical report TR-97-13 1-60 (SKB).

[28] Ewing,R.C. (2015). Long term storage of spent nuclear fuel Nature material vol 14.

[29] Kleykamp,H. (1985).The chemical state of the fission products in oxide fuels . Journal of Nuclear Material 131,pp.221-226.

[30] Buck,E.C.,Hanson,B.D., McNamara,B.K. (2004). In Energy, Waste, and the Environment: A Geochemical Perspective.The Geological Society of London Special Publication 236 (Gieré R, Stille P) pp. 65-88.

[31] Adeola,A.O., Iwuozor,K.O., Akpomie,G., Adegoke,K.A., Oyedotun,K.O., Ighalo,J.O., Amaku, J.F., Olisah ,C.,Conradie,J.(2023). Advances in the management of radioactive wastes and radionuclide contamination in environmental compartments: a review., Environ Geochem Health 45: pp.2663–2689.

[32]Darda,S.A.,Gabbar,H.A., Damideh, V., Aboughaly, M., Hassen.I. (2021).A comprehensive review on radioactive waste cycle from generation to disposal Journal of Radioanalytical and Nuclear Chemistry (2021) 329: pp.15–31.

[33] Kreusch, J., Neumann,W., Appel,D., Diehl,P.(2006).Nuclear Fuel Cycle Nuclear Issues Paper No. 3.

[34] Na¨slund,J.O.,Brandefelt, J., Liljedahl,L.C. (2013).Climate Considerations in Long-Term Safety Assessments for Nuclear Waste Repositories AMBIO, 42:393–401.

[35] Holm, M. (2011). RadTox, a computer program for assessing radiotoxicity curves for used nuclear fuel. Chalmers University of Technology, Department of Nuclear Chemistry, Master's thesis.

[36] Brantberger,M., Zetterqvist, A.,Arnbjerg-Nielsen,T.,Olsson,T.,Outters,N.,Syrjaenen, P. (2006). Final repository for spent nuclear fuel.Underground design Forsmark,Layout D1.

[37] Nuclear energy agency (NEA). (2020).Management and disposal of high-level radioactive waste: Global progress and solutions.

[38]https://www.powermag.com/swedens-government-approves-construction-of-spent-nuclear-fuel-repository.

[39] Spahiu, K., Cui, D., Lundström, M. (2004). The fate of radiolytic oxidants during spent fuel leaching in the presence of dissolved near field hydrogen. Radiochim. Acta 92, pp. 625–629.

[40] Sunder,S., Shoesmith,D.W.,Miller,N.H. (1997).Oxidation and dissolution of nuclear fuel ($UO_2$) by the products of the alpha radiolysis of water Journal of Nuclear Materials 244 pp. 66–74.

[41] Christensen,H., Sunder,S. (2000).Current State of Knowledge of Water Radiolysis Effects on Spent Nuclear Fuel Corrosion, Nuclear Technology, 131:1, pp.102-123.

[42] Johnson,L.H., Leneveu,D.M., Shoesmith,D.W., Oscarson, D.W., Gray,M.N., Lemire, R.J., Garisto,N.C. (1994). The disposal of Canada's Nuclear Fuel Waste: The Vault Model for Post closure Assessment, Atomic Energy of Canada Limited Report, AECL-10714.

[43] Shoesmith,D.W.,Sunder,S.,Hocking,W.H.(1994). in: Electrochemistry of Novel Materials, eds. J. Lipkowski and P.N.Ross VCH, New York, 1994 p. 297.

[44] Parks,G.A.,Pohl,D.C. (1988). Hydrothermal solubility of uraninite Geochim. Cosmochim. Acta 52,.pp 863-875.

[45] Lemire,R.J., Garisto, F. (1989).The Solubility of U, Nb, Pu, Th and Tc in a Geological Disposal Vault for Used Nuclear Fuel, Atomic Energy of Canada Limited Report, AECL10009 1989 .

[46] Jonsson,M.,Nielsen,F.,Roth, O., Ekeroth, E., Nilsson, S., Hossain, M.M. (2007). Radiation induced spent nuclear fuel dissolution under deep repository conditions. Envir. Sci. Technol. 41, pp.7087-7093.

[47] Ekeroth, E., Roth,O., Jonsson,M.(2006).The relative impact of radiolysis products in radiation induced oxidative dissolution of $UO_2$ . Journal of Nuclear Materials 355 pp. 38–46.

[48] Merino , J., Cera ,E., Bruno,J., Quinones,J., Casas,I., Clarens,F., Gime´nez ,J., ,de Pablo, J., Rovira,M.,Martınez-Esparza,A.(2005).Radiolytic modelling of spent fuel oxidative dissolution mechanism. Calibration against $UO_2$ dynamic leaching experiments,Journal of Nuclear Materials.Vol. 346, Issue 1, pp. 40-47.

[49] Fuel and Canister Process Report for the Safety Assessment SR-Can. (2006). SKB Technical Report, TR-06-22 .

[50] Criticality Effects of Long-Term Changes in Material Compositions and Geometry in Disposal Canisters. (2016) SKB Technical Report, TR-16-06 .

[51] Jonsson, M. (2012).Radiation Effects on Materials Used in Geological Repositories for Spent Nuclear Fuel, ISRN Materials Science, 2012, Article ID 639520, 13.

[52] Saheb,M., Neff , D., Dillmann, P.H., Matthiesen,H., Foy,E. (2008). Long-term corrosion behaviour of low-carbon steel in anoxic environment: Characterisation of archaeological artefacts, J. Nucl. Mater. 379 pp. 118–123.

[53] Odorowski, M., Jegou,C., de Windt,C.L.,Broudic,V.,Jouan,G.,Peuget,S.,Martin,.C. (2017). Effect of metallic iron on the oxidative dissolution of $UO_2$ doped with a radioactive alpha emitter in synthetic Callovo-Oxfordian water, Geochim. Cosmochim. Acta 219, pp.1-21.

[54] Ishikawa, T., Kondo,Y., Yasukawa,A., Kandori, K. (1998). Formation of magnetite in the presence of ferric oxyhydroxides, Corros. Sci. 40 pp. 1239–1251.

[55] Ritter, K., Odziemkowski, M.S.,Gillham,R.W.(2002). An in-situ study of the role of surface films on granular iron in the permeable iron wall technology, J. Contam. Hydrol. 55 87–111.

[56] Smart,N.R.,Blackwood,D.J.,Werme,L. (2001).The anaerobic corrosion of carbon steel and cast iron in artificial groundwaters, SKB Technical Report TR-01-22 .

[57] Smart,N.R.,Rance,A.P., Werme,L.O (2008). The effect of radiation on the anaerobic corrosion of steel, J. Nucl. Mater. 379.pp. 97–104,

[58] Loida,A.,Kelm,M., Kienzler,B., Geckeis,H.,Bauer,A. (2006).The Effect of Nearfield Constraints on the Corrosion Behavior of High Burnup Spent Fuel, Mat. Res. Soc. Symp. Proc. 932 (72.1).

[59] Puranen, A., Barreiro, A.F., Evins, L.Z., Spahiu, K. (2020). Spent fuel corrosion and the impact of iron corrosion – The effects of hydrogen generation and formation of iron corrosion products J. Nucl. Mater. 542, pp. 152423.

[60] Neretnieks, I. (1985).Some aspects of the use of iron canisters in deep lying repositories for nuclear waste.Nagra.

[61] Bonin.,B., Colin,M., Dutfoy,A. (2000). Pressure building during the early stages of gas production in a radioactive waste repository. Journal of Nuclear Materials, 281(1): pp. 1-14.

[62] Wu,L.,Qin,Z.,Shoesmith,D.S.(2014). An improved model for the corrosion of used nuclear fuel inside a failed waste container under permanent disposal conditions, Corros. Sci. 84 ,pp. 85–95.

[63] Amme,M., Pehrman,R., ,Deutsch,R., Roth,O., Jonsson,M. (2012).Combined effects of Fe (II) and oxidizing radiolysis products on $UO_2$ and $PuO_2$ dissolution in a system containing solid $UO_2$ and $PuO_2$. Journal of Nuclear Materials, 430(1-3): pp. 1-5.

[64] Jégou, C., Peuget, S., Lucchini, J.F., Corbel,C.,Broudic,V., Bart,J.M. (2000). Effect of Spent Fuel Burnup and Composition on Alteration of the U(Pu)$O_2$ Matrix. MRS Online Proceedings Library 663, 399.

[65]Carbol,P., Patrik Fors,P., Gouder,T., Spahiu,K.(2009).Hydrogen suppresses $UO_2$ corrosion. Geochimica and Cosmochimica Acta, 73(15): pp. 4366-4375.

[66] Jonsson, M. (2012).Radiation Effects on Materials Used in Geological Repositories for Spent Nuclear Fuel, ISRN Materials Science, Article ID 639520, 13 pages, 2012.

[67] Fors,P., Carbol, P.,Winckel,S.V., Spahiu, K.(2009).Corrosion of high burn-up structured $UO_2$ fuel in presence of dissolved $H_2$, J. Nucl. Mater. 394 pp. 1–8.

[68] Puranen,A., Roth,O., Evins,L-Z., Spahiu, K. (2018). Aqueous leaching of high burnup $UO_2$ fuel under hydrogen conditions, in: MRS Advances Scientific Basis for Nuclear Waste Management XLI, 3, Materials Research Society, pp. 1013– 1018.

[69] Ekeroth,E., Granfors,M., Schild,D., Spahiu,K.(2020). The effect of temperature and fuel surface area on spent nuclear fuel dissolution kinetics under $H_2$ atmosphere, J. Nucl. Mater. 531 , 151981.

[70]Cui,D.,Ekeroth,E.,Fors,P.,Spahiu,K.,(2008). Surface Mediated Processes in the Interaction of Spent Fuel or alpha-doped $UO_2$ with $H_2$, MRS Symp. Proc. 1104 pp.87–99.

[71] Spahiu, K.,Devoy,J.,Cui,D., Lundström,M., (2004). The reduction of U(VI) by near field hydrogen in the presence of UO2 (s). Radiochimica Acta, 92(9-11): pp 597-601.

[72] Spahiu. K. (2021). EURAD State of Knowledge (SoK) Report, Spent Nuclear Fuel Domain 3.1.1Version, 2021 - ejp-eurad.eu.

[73] Duro ,L., Riba ,O., Martínez-Esparza,A.,Bruno.J. (2013). Modelling the Activation of $H_2$ on Spent Fuel Surface and Inhibiting Effect of $UO_2$ Dissolution Mater. Res. Soc. Symp. Proc. Vol. 1518 .

[74] Broczkowski,M.E.,Zagidulin,D.,Shoesmith,D.W.(2010).The Role of Dissolved Hydrogen on the Corrosion/Dissolution of Spent Nuclear Fuel ACS Symposium Series; American Chemical Society: Washington, DC.

[75] Cui.,D., Spahiu,K. (2002).The reduction of U(VI) on corroded iron under anoxic conditions. Radiochimica Acta, 90(9-11): pp. 623-628. 41

[76] Bruno, J., Grenthe, I., Munoz, M. (1985). Studies on radionuclide coprecipitation-solid solution formation. The $UO_2$(s)-$La(OH)_3$(s) coprecipitation as an analogue for the $UO_2$(s)-Pu $(OH)_3$(s) system. MRS Symp. Proc. 50, 717-726.

[77] Bruno, J., Sandino, A. (1987). Radionuclide coprecipitation, SKB Technical Report TR-87-23, Svensk Kärnbränslehantering AB.

[78] Bruno, J., Sandino, A. (1988) The thermodynamics and kinetics of coprecipitation and its effect on radionuclide solubility, Radiochim. Acta 44/45, 17-21.

[79] Rousseau,G., Fattahi,M., Grambow,B., Boucher,F., Ouvrard,G. (2006). Coprecipitation of thorium and lanthanum with $UO_{2+X}$(s) as host phase. Radiochim.Acta 94,pp. 517-522.

[80] Rousseau, G., Fattahi, M., Grambow. B., Boucher, F., Ouvrard, G. (2002). Coprecipitation of thorium with $UO_2$ Radiochim. Acta 90,pp. 523-527.

[81] Endrizzi, F., Rao,L. (2014).Chemical speciation of uranium (VI) in marine environments: complexation of calcium and magnesium Ions with $[(UO_2)(CO_3)_3]^{4-}$ and the effect on the extraction of uranium from seawater. Chemistry–A European Journal, 2014. 20(44): pp. 14499-14506.

[82] Schenk, H. J., Astheimer, L., Witte, E. G., Schwochau, K. (1982). Development of Sorbers for the Recovery of Uranium from Seawater. 1. Assessment of Key Parameters and Screening Studies of Sorber Materials. Separation Science and Technology, 17(11), 1293–1308.

[83] Gurzhiy, V.V., Kalashnikova, S.A., Kuporev, I.V., Plášil, J.(2021). Crystal Chemistry and Structural Complexity of the Uranyl Carbonate Minerals and Synthetic Compounds. Crystals , 11, 704.

[84]Bernhard,G.,Geipel,G.,Reich,T.,Brendler,V.,Amayri,S.,Nitsche,H.(2001).Uranyl(VI) carbonate complex formation: Validation of the $Ca_2UO_2(CO_3)_3$ (aq.) species. Radiochimica Acta, . 89(8): pp. 511-518.

[85] Bernhard, G., Geipel,G.,Brendler,V., Nitsche,H.,(1996).Speciation of uranium in seepage waters of a mine tailing pile studied by time-resolved laser-induced fluorescence spectroscopy (TRLFS). Radiochimica Acta. 74(s1): pp. 87-92.

[86] Kalmykov, S.N.,Choppin,G.R.(2000). Mixed $Ca^{2+}$/ $UO_2^{2+}$/ $CO_3^{2-}$ complex formation at different ionic strengths. Radiochimica Acta, 88(9-11): pp. 603-608.

[87] Coto, B., Martos,C., Peña,J.L.,Rodríguez,R., G. Pastor,G. (2012). Effects in the solubility of $CaCO_3$: Experimental study and model description. 324: pp. 1-7.

[88] Dong, W., S.C. Brooks, S.C. (2006).Determination of the formation constants of ternary complexes of uranyl and carbonate with alkaline earth metals ($Mg^{2+}$, $Ca^{2+}$, $Sr^{2+}$, and $Ba^{2+}$) using anion exchange method. Environmental science & technology, 40(15): pp. 4689-4695.

[89] Liger,E.,Charlet,L.,Cappellen, P.V. (1999).Surface catalysis of uranium (VI) reduction by iron(II), Geochim.Cosmochim.Acta,63.pp. 2939-2955.

[90]Du,X.,Boonchayaanant,B.,Wu,W.M.,Fendorf,S.,Bargar,J.,Criddle,C.S.(2020) .Reduction of uranium (VI) by soluble iron (II) conforms with thermodynamic predictions, Environ.Sci.Technol.,54.pp. 6021-6030.

[91] Stewart, B.D.,Mayes, M.A.,Fendorf ,S.(2010). Impact of uranyl− calcium carbonato complexes on uranium (VI) adsorption to synthetic and natural sediments. Environmental science & technology, 44(3): pp. 928-934.

[92]William,J.D.(1997).Groundwater Geochemistry: Fundamentals and applications to contaminant CRC Press Taylor & Francis Group 6000 Broken Sound Parkway NW, Suite 300 Boca Raton, FL 33487-2742.

[93] Bajaj,N.S., Joshi, R.A. (2021). Chapter 3-Energy materials: synthesis and characterization techniques; , Energy Materials. Fundamentals to Applications .pp. 61-82.

[94] Carlsson, T., Aalto,H. (1997). Coprecipitation of Ni with Calcite: An Experimental Study. MRS Online Proceedings Library 506, 621–627.

[95] Enzo Curti,E. (1999). Coprecipitation of radionuclides with calcite: estimation of partition co-efficient based on a review of laboratory investigations and geochemical data. Applied GeochemistryVol.14, pp. 433-445.

[96] International Union of Pure and Applied Chemistry. (1973). Recommendations on Nomenclature for Contamination Phenomena in Precipitation from Aqueous Solutions.

[97] Bruno, J., Montoya, V. (2012).From aqueous solution to solid solutions: A process-oriented review of the work performed within the FUNMIG project.Applied Geochemistry Vol.27, Issue 2, pp. 444-452.

[98] Rane, A.V., Kanny,K., Abitha,V.K., Thomas,S. (2018). Methods for Synthesis of Nanoparticles and Fabrication of Nanocomposites Chapter 5. Synthesis of Inorganic Nanomaterials pp. 121-13.

[99] Abbaschian R., Reed, H., Robert,E. (2008). Physical Metallurgy Principles. ISBN 978-0-495-08254-5.

[100] Grandia,F., Merino,J., Bruno,J.(2008). Assessment of the radium-barium co-precipitation and its potential influence on the solubility of Ra in the near-field. Technical Report TR-08-07.

[101] Henderson, L. M., Kracek, F. C. (1927). J. Am. Chem. Soc. 49, 738.

[102]Stumm,W.,Morgan,J.J.(1981).Aquatic chemistry; An introduction Emphasizing chemical equilibria in natural waters Second Edition. Chapter 5 pp. 287-298.

[103] Doerner H. A., Hoskins W. M.(1925). J. Am. Chem. Soc. 47, 662.

[104] Rai, D., Felmy, A.R., Ryan, J. L. (1990). Uranium (IV) hydrolysis constants and solubility product of $UO_2 \cdot xH_2O$(am), Inorg. Chem. 29, 260-264.

[105] Mesmer, R.E., Baes, C.F. (1990). Review of Hydrolysis Behavior of Ions in Aqueous Solutions. MRS Online Proceedings Library 180, 85.

[106] Neck, V., Kim, J.I. (2001). Solubility and hydrolysis of tetravalent actinides, Radiochim. Acta, 89, pp.1-16.

[107] Guillaumont, R., Fanghänel, T., Fuger, J., Grenthe, I., Neck, V., Palmer, D.A., Rand, M.H. (2003). Update on the Chemical Thermodynamics of Uranium, Neptunium, Plutonium, Americium and Technetium, Vol.5 of Chemical Thermodynamics, in, Elsevier Science Publishers, Amsterdam,

[108] Lide, D. R., (2005). CRC Handbook of Chemistry and Physics ($86^{th}$ ed.).

[109] Greenwood and Earnshaw.(1997). Chemistry of the elements pp. 1244–8 $2^{nd}$ edition.

[110] Yu,P., Scott,Z.,Hayes,A.,O'Keefe, T.J.,O'Keefe,M.J.,Stoffer, J.O.(2006).The Phase Stability of Cerium Species in Aqueous Systems II. The Ce(III/IV)–$H_2O$–$H_2O_2$/$O_2$ Systems. Equilibrium considerations and Pourbaix Diagram calculations. Journal of The Electrochemical Society, 153 C74-C79.

[111] Buchenko, L.I., Kovalenko,P.N., Evstifeev Russ,M.M. (1970) 15, 1666.

[112] Kragten, J., Denkop-Weever, L.G., (1978). Hydroxide complexes of cerium (III), Talanta, 25, 147-150.

[113] Diakonov, I.I., Ragnarsdottir, K.V., Tagirov, B.R. (1998b). Standard thermodynamic properties and heat capacity equations for rare earth element hydroxides. II. Ce(III)-, Pr-, Sm-, Eu(III)-, Gd-, Tb-, Dy-, Ho-, Er-, Tm-, Yb- and Y-hydroxides. Comparison of thermochemical and solubility data. Chem. Geol., 151, 327-347.

[114] Bondareva, T.N., Stromberg, A.G. (1955). Potentiometric study of Ce(IV) and Ce(III) precipitates by effect of solution pH on the value of the redox potential of $Ce^{4+}/Ce^{3+}$. Zhur. Obshch. Khim., 25, 666-671.

[115]Chirkst,D.E.,Lobacheva,O.L., Berlinskii, I.V., Sulimova,M.I.,(2009).The thermodynamic properties of hydroxo compounds and the mechanism of ion flotation for cerium, europium and yttrium. Z. Fiz. Khim., 83, 2221-2226.

[116] Akselrud, N.V., Spivakovskii, V.B., (1959). Study of the basic chloride and hydroxide of cerium. Zhur. Neorg. Khim., 4, 56-61.

[117]Mironov,N.N.,Odnotsevtsev.(1957).Several studies of multicomponent systems containing rare earth elements. Zhur. Neorg. Khim., 11, 2202-2207

[118] Brown, P. L., Ekberg, C. (2016). Hydrolysis of metal ions. John Wiley & sons.

[119] Kungliga Tekniska Högskolan (KTH). (1959).Some laboratory methods, TRITA-OOK-T128, Royal Institute of Technology, Stockholm, Sweden

[120] Gran, G. (1952). Determination of the equivalence point in potentiometric titrations. Part II. The Analyst, 77, 661-671.

[121] Nassar,M.Y., Ahmed,I.S.,Mohamed,T.Y., Khatab,M. (2016). A controlled, template-free, and hydrothermal synthesis route to sphere-like α-$Fe_2O_3$ nanostructures for textile dye removal, Rsc Advances, 6 , 20001-20013.

[122]Laaksoharju,M.,Smellie,J.,Tullborg,E.L.,Gimeno,M.Hallbeck,L.,Molinero,J.,Waber,N.( 2008).Bedrock hydrogeochemistry Forsmark, Site Descriptive Modelling SDM-Site Forsmark.

[123]Yamada,N.(2015). Kinetic energy discrimination in collision/reaction cell ICP-MS: Theoretical review of principles and limitations, Spectrochimica Acta Part B: Atomic Spectroscopy, 110, 31-44.

[124] Klementiev, K., Norén, K., Carlson, S., Sigfridsson Clauss, K. G. V. and Persson, I. (2016). The BALDER beamline at the MAX IV Laboratory. J. Phys.Conf. Ser., 712, 012023.

[125] Thompson, A., Attwood, D., Gullikson, E., Howells, M., Kim, K.J., Kirz, K., Kortright, J., Lindau, I., Liu, Y., Pianetta, P., Robinson, A., Scofield, J., Underwood, J., Williams, G., Winick, H. (2009). X-ray Data Booklet, Lawrence Berkley National Laboratory, CA, USA.

[126] George, G. N., Pickering, I. J. (1993). EXAFSPAK - A Suite of Computer Programs for Analysis of X-ray Absorption Spectra; SSRL: Stanford, CA.

[127] Zabinsky, S. I., Rehr, J.J., Ankudinov, A., Albers, R.C., Eller, M.J. (1995). Multiple-Scattering Calculations of X-ray Absorption Spectra. Phys. Rev. B, 52, 2995-3009.

[128] Fanghänel, T., Neck, V., Kim, J.I.( 1996). The ion product of $H_2O$, dissociation constants of $H_2CO_3$ and Pitzer parameters in the system $Na^+/H^+/OH^-/HCO_3^-/CO_3^{2-}/ClO_4^-/H_2O$ at 25 °C, J. Soln. Chem. 25, 327-343.

[129] Rai D., Felmy, A., Sterner, S. M., Moore, D. A., Mason M.J. (1997). The solubility of Th (IV) and U(IV) hydrous oxides in concentrated NaCl and $MgCl_2$ solutions, Radiochim. Acta 79, 239-247.

[130] Grenthe I, Gaona X, Plyasunov A, Rao L, Runde W H, Grambow B, Konings R J M, Smith A L, Moore E E, (2020). Second update on the thermodynamics of U, Np, Pu, Am and Tc, OECD Nuclear Energy Agency Data Bank Eds., OECD publications, Paris, France.

[131] Fujiwara, K., Yamana, H., Fujii, T., Moriyama, H. (2003). Determination of uranium (IV) hydrolysis constants and solubility product of $UO_2$.xH2O, Radiochim. Acta 91, 345-350.

[132] Fujiwara, K., Yamana, H., Fujii, T., Moriyama, H. (2002). Solubility product of U(IV) hydrous oxide, J. Nucl. Sci. Technol. 39: Suppl. 3, 290-293.

[133] Cevirim-Papaioannou, N., Yalcintas, E., Gaona, X., Dardenne, K., Altmaier, M, Geckeis, H. (2018). Redox chemistry of uranium in reducing, dilute to concentrated NaCl solutions, Appl. Geochem. 98, 286-300.

[134] Jordan, N., Thoenen, T., Spahiu, K., Kelling, J., Starke, S., Brendler, V. (2024). A critical review of the solution chemistry, solubility, and thermodynamics of europium: Recent advances in Eu(III) hydrolysis, Coord. Chem. Reviews, 510, 215702.

[135] McIntire W.L. (1963). Trace element partition coefficients-a review of the theory and applications to geology, Cosmochim. Geochim. Acta, 27, 1209-1264.

[136] Rai, D., Hess, N., Yui, M., Felmy, A., Moore, D. (2004). Thermodynamics and solubility of $U_xNp_{1-x}O_2$ (am) solid solutions in the carbonate system, Radiochim. Acta 92 , 527-535.

[137] Toby, B.H. and Von Dreele, R.B.(2013). GSAS-II: the genesis of a modern open-source all-purpose crystallography software package, J. Appl. Crystallography 46, 544-549.

[138] Kleykamp, H.(1993). The solubility of selected fission products in $UO_2$ and (U, Pu) $O_2$, J. Nucl. Mater. 206, 82-86.

[139] Mclver, E.J., (1966). Unit cell size of solid solutions of uranium dioxide and fission product oxides. Technical report AERE-M-1612.

[140] Leinders, G., Cardinales T., Binnemans, K., Verwerft, M.( 2015). Accurate lattice parameter measurements of stoichiometric uranium dioxide, J. Nucl. Mater. 469, 135-142.

[141] Prieur, D., Martel, L., Vigier, J.F., Scheinost, A.C., Kvashnina, K. O., Somers, J., Martin, P.M.( 2018). Aliovalent cation substitution in $UO_2$: Electronic and local structures of $U_{1-y}La_yO_{2\pm x}$ solid solutions.; Inorganic Chemistry 57(3), 1535-1544.

[142] Hansson, N.L, Tam, P.L, Ekberg, C., Spahiu, K. (2021). XPS study of external α-radiolytic oxidation of $UO_2$ in the presence of argon or hydrogen, J. Nucl. Mater., Vol. 543, 2021, 152604.

[143] Ilton, E.S., Bagus, P.S.(2011). XPS determination of uranium oxidation states , Surf. Interface Anal. 43, 1549–1560.

[144] Paparazzo, E. (2018). Use and misuse of X-ray photoemission spectroscopy Ce3d spectra of $Ce_2O_3$ and $CeO_2$, Journal of Physics: Condensed Mater, Vol.30, 343003.

[145] Leinders, G., Bes, R., Kvashnina, K., Cleverest, M. (2020). Local Structure of U(IV) and U(V) Environments: The Case of $U_3O_7$. Inorg. Chem. 59, 4576-4587.

[146] Allen, P. G., Shuh, D. K., Bucher, J. J., Edelstein, N. M., Palmer, C. E. A., Marquez, L. N. (1996). EXAFS Spectroscopic Study of Uranium (VI) Precipitates, Report LBNL-39934, Ernest Orlando Lawrence Berkeley National Laboratory.

[147] Chaves,L.H(2005). The role of green rust in the environment: a review, Revista Brasileira de Engenharia Agrícola e Ambiental, 9, 284-288.

[148]Taylor,R.,McKenzie,R.(1980).The influence of aluminum on iron oxides. VI. The formation of Fe(II)-Al (III) hydroxy-chlorides,-sulfates, and-carbonates as new members of the pyroaurite group and their significance in soils, Clays Clay Miner., 28, 179-187.

[149] Gouder, T.,Eloirdi,R.,Caciuffo,R.(2018).Direct observation of pure pentavalent uranium in $U_2O_5$ thin films by high resolution photoemission spectroscopy, Scientific reports, 8,1-7.

[150] B. Santos, H. Nesbitt, J. Noel, D. Shoesmith, X-ray photoelectron spectroscopy study of anodically oxidized SIMFUEL surfaces, Electrochim. Acta, 49 (2004) 1863-1873.

[151] Parkhurst, D.L.,Appelo,C.(2013).Description of input and examples for PHREEQC version 3a computer program for speciation, batch-reaction, one-dimensional transport, and inverse geochemical calculations, US geological survey techniques and methods, 6 , 497.

[152]Ekberg ,C., Emrén,A. (1993).Finding and correcting calculation errors in PHREEQC, in: 4th Int. Conf. on the Chem. and Migr. Behaviour of Actinides and Fission Products in the Geosphere, Charleston, SC USA, Dec. 12-17, Oldenbourg Verlag, Munich, 1994.

[153] Sass, B. M., Rai, D. (1987). Solubility of amorphous chromium (III)-iron (III) hydroxide solid solutions, Inorg. Chem. 26, 2228-2232.

[154] Bénézeth, P., Dandurand, J.,Harrichoury,J.(2009).Solubility product of siderite ($FeCO_3$) as a function of temperature (25–250 C), Chem. Geol., 265 (2009) 3-12.

[155] Dewey,C.,Sokaras,D., Kroll,T.,Bargar,J.R.,Fendorf,S. (2020).Calcium-uranyl-carbonato specieskinetically limit U(VI) reduction by Fe(II) and lead to U(V)-bearing ferrihydrite, Environ. ‘Sci.Technol.,54, 6021-6030.

[156]Pan,Z.,Bartova,B.,Lagrange,T.,Butorin,S.M.,Hyatt,N.C.,Stennett,M.C.,Kvashnina,R., Bernier,L., BernierLLatmani, K.O (2020). Nanoscale mechanism of $UO_2$ formation through uranium reduction by magnetite, Nature communications, 11, 1-12.

[157] O'Loughlin,E.J.,Kelly,S.D.,Cook,R.E., Csencsits,R.,Kemner,K.M.(2003).Reduction of uranium (VI) by mixed iron (II)/iron (III) hydroxide (green rust): formation of $UO_2$ nanoparticles,Environ. Sci. Technol., 37, 721-727.

[158] Chaves,L.H. (2005).The role of green rust in the environment: a review, Revista Brasileira de Engenharia Agrícola e Ambiental, 9 284-288.

[159] Guillamont,R., Fanghanel,T., Grenthe,I., Neck,V., Palmer,D., Rand, M.(2003).Update on the chemical thermodynamics of uranium, neptunium, plutonium, americium and technetium, Nuclear Energy Agency Data Bank, Organization for Economic Co-operation, Development, 5.